Magnetic Coupling of Individual Atoms through Non-magnetic Spacer Layers

Dissertation
zur Erlangung des Doktorgrades
am Department Physik
der Universität Hamburg

vorgelegt von
Liudmila Vasiljewna Dzemiantsova
aus Minsk, Belarus

Hamburg
2013

Gutachter der Dissertation	Prof. Dr. R. Wiesendanger Prof. Dr. A. I. Lichtenstein
Gutachter der Disputation	Prof. Dr. R. Wiesendanger Prof. Dr. H. P. Oepen
Datum der Disputation	11.01.2013
Vorsitzender des Prüfungsausschusses	Dr. S. Mendach
Vorsitzender des Promotionsausschusses	Prof. Dr. P. Hauschildt
Dekan der MIN-Fakultät	Prof. Dr. H. Graener

Abstract

The aim of this thesis is the study of magnetic coupling of individual magnetic atoms to ferromagnetic electrodes via non-magnetic spacer layers. Two very different systems are chosen for this purpose, namely graphene/Ni(111) and Pd adlayers on Co/Ir(111).

The magnetism of the bare and graphene-covered (111) surface of a Ni single crystal is studied by employing three different magnetic imaging techniques and *ab initio* calculations, covering length scales from the nanometer regime up to several millimeters. With low temperature spin-polarized scanning tunneling microscopy (SP-STM), domain walls with widths of 60 - 90 nm are found and can be moved by small perpendicular magnetic fields. Spin contrast is also achieved on the graphene-covered surface, which means that the electron density in the vacuum above graphene is substantially spin-polarized. In accordance with density functional theory (DFT) calculations, an enhanced atomic corrugation with respect to the bare surface is observed, due to the presence of the carbon p_z orbitals and as a result of the quenching of Ni surface states. The latter also leads to an inversion of spin-polarization with respect to the pristine surface. Room temperature Kerr microscopy shows a stripe like domain pattern with stripe widths of 3 - 6 μm. Applying in-plane-fields, domain walls start to move at about 13 mT and a single domain state is achieved at 140 mT. Via scanning electron microscopy with polarization analysis (SEMPA) a second type of modulation within the stripes is found and identified as 330 nm wide V-lines. Qualitatively, the observed surface domain pattern originates from bulk domains and their quasi-domain branching is driven by stray field reduction. Individual Fe, Co and Cr atoms on graphene/Ni(111) are studied by means of scanning tunneling spectroscopy (STS). However, the systems obtained are difficult to investigate due to residual contamination of Ni(111).

Pd adlayers on Co/Ir(111) and single Co atoms adsorbed on top are studied from both experimental and theoretical side. With SP-STM, the morphology and the spin-resolved electronic properties of mono- and double-layer Pd on Co/Ir(111) are investigated. By measuring the differential tunneling conductance, pseudomorphic growth with two stackings of the Pd monolayer can easily be distinguished electronically. Spin contrast is achieved on both the Pd mono- and double-layer and on Co adatoms on top, which means that the electron density above the surfaces and adatoms is spin-polarized. Indeed, based on DFT calculations, the surface Pd atoms of mono- and double-layer are found to carry an induced magnetic moment of about 0.3 μ_B and 0.2 μ_B, respectively; Co layers adsorbed on top of a Pd mono- and double-layer possess a magnetic moment of about 2.0 μ_B/atom. The calculations also show that Co adlayers are ferromagnetically coupled to the Co/Ir(111) underneath. The size of the magnetic exchange coupling is, however, reduced by a factor of three from a mono- to a double-layer Pd spacer between the Co layers.

Inhaltsangabe

Das Ziel dieser Arbeit ist die Untersuchung der magnetischen Kopplung von individuellen magnetischen Atomen an ferromagnetische Elektroden durch nichtmagnetische Zwischenschichten. Zwei sehr unterschiedliche Systeme werden für diesen Zweck ausgewählt, nämlich Graphen/Ni(111) und Pd Adsorptionsschichten auf Co/Ir(111).

Der Magnetismus der freien und Graphen-bedeckten (111)-Oberfläche eines Nickel-Einkristalls wird sowohl mit drei magnetisch sensitiven Methoden abgebildet als auch in *ab initio* Rechnungen studiert. Dabei werden Längenskalen vom Nanometer- bis in den Millimeterbereich untersucht. Mittels Tieftemperatur-Rastertunnelmikroskopie (SP-STM) werden Domänenwände mit Breiten von 60 bis 90 nm gefunden, die durch externe senkrechte Magnetfelder bewegt werden können. Auch auf der Graphen-bedeckten Oberfläche wird Spin-Kontrast beobachtet, was bedeutet, dass die Elektronen-Zustandsdichte im Vakuum oberhalb der Graphenschicht deutlich spin-polarisiert ist. In Übereinstimmung mit Dichtefunktional-Rechnungen (DFT) wird eine im Vergleich zur freien Oberfläche erhöhte atomare Korrugation gemessen, was auf auf p_z-Orbitale des Kohlenstoffs und die Unterdrückung der Ni-Oberflächenzustände zurückzuführen ist. Letztere führt außerdem zu einer Umkehrung der Spin-Polarisation gegenüber der freien Oberfläche. Raumtemperatur-Kerr-Mikroskopie zeigt eine Streifen-Domänenstruktur mit Streifenbreiten von 3 - 6 μm. Unter dem Einfluß eines Magnetfeldes in der Ebene beginnen sich die Domänenwände ab 13 mT zu bewegen, und bei 140 mT wird ein Eindomänenzustand erreicht. Mittels Rasterelektronenmikroskopie mit Polarisationsanalyse (SEMPA) wird eine weitere, 330 nm breite V-förmige Modulation innerhalb der Streifen gefunden. Qualitativ lässt sich dieses Muster auf die eine Verzweigung der bulk-Domänen an der Oberfläche zurückführen, die das Streufeld verringert. Weiterhin werden einzelne Eisen-, Kobalt- und Chromatome auf der Graphen-bedeckten Ni(111)-Oberfläche mit Rastertunnelspektroskopie untersucht. Diese Messungen erweisen sich wegen der Restverunreinigung an der Ni(111)-Oberfläche als schwer interpretierbar.

Pd-Adsorptionsschichten auf Co/Ir(111) und einzelne, oben adsorbierte Co-Atome werden sowohl von experimenteller als auch theoretischer Seite untersucht. Mit SP-STM werden die Morphologie und die Spin-aufgelösten elektronischen Eigenschaften von Mono- und Doppellagen Pd auf Co/Ir(111) untersucht. Durch Messen der differentiellen Tunnelkonduktanz kann das pseudomorphe Wachstum mit zwei Stapelungen der Pd-Monoschicht leicht elektronisch unterschieden werden. Spin Kontrast wird sowohl auf den Pd-Mono- und Doppellagen als auch auf den Co-Atomen erreicht, was bedeutet, dass die elektronische Zustandsdichte oberhalb der Oberflächen und Atome spinpolarisiert ist. Tatsächlich zeigen DFT-Rechnungen, dass die Pd-Atome der Mono- und Doppellagen ein induziertes magnetisches Moment von ungefähr 0.3 μ_B beziehungsweise 0.2 μ_B besitzen; auf den Mono- und Doppellagen adsorbierte Co-Schichten besitzen ein magnetisches Moment von etwa 2.0 μ_B/Atom. Die

Berechnungen zeigen auch, dass Co-Adsorptionsschichten ferromagnetisch an das Co/Ir(111) darunter gekoppelt sind. Die Größe der magnetischen Austauschkopplungen ist jedoch reduziert um einen Faktor drei von einer Monozu einer Doppellage Pd als Abstandshalter zwischen den Co-Schichten.

Contents

Chapter 1

Preface

Magnetic atoms adsorbed on surfaces have become an active research topic in the last few years due to their importance in the fundamental understanding of magnetism and practical applications for spin-based computing schemes. In particular, knowledge about the electronic configuration of individual adatoms, their hybridization with the host, magnetic moments, exchange and anisotropy energies on the atomic scale is crucial for tailoring magnetic devices in reduced dimensions and tuning their properties.

A recent progress achieved in surface science is the preparation of samples with extremely small densities of magnetic atoms (typically on the order of 10^{14} atoms/cm^{-2}) on a macroscopic substrate [1]. The experimental challenge lies in probing such systems. For decades, the measurement of surface dilute magnetic impurity systems was restricted to the anomalous Hall effect (AHE) [2; 3] and impurity-induced detuning of a thin film superconducting LC oscillator [4]. More recent X-ray magnetic circular dichroism (XMCD) has been shown to probe dilute surface impurities with a concentration down to 3×10^{12} atoms cm^{-2}, corresponding to about 0.002 mono-layers (ML) [5]. While these methods are spatially averaging and therefore report on ensemble properties, *spin-polarized scanning tunneling microscopy* (SP-STM) and *spectroscopy* (SP-STS) are powerful tools to resolve the electronic and magnetic structure at a lateral resolution down to the atomic scale. Using these techniques, atomic adsorbates have been explored on different metallic surfaces either non-magnetic or magnetic [6; 7; 8; 9; 10].

A thin insulating film effectively decouples a magnetic adatom from the conductance electrons of a substrate. On this surface, the adatom exhibits a localized spin, thereby different magnetic states are localized on the adsorbate. Heinrich and co-workers reported for the first time that these states can be excited and probed by the STM [11]. They measured excitation spectra for Mn atoms on A_2O_3/NiAl and showed that energy needed to flip the adatom

spin can be evaluated as the Zeeman energy of a simple local spin, and is $\Delta E \approx 0.8$ meV at $B = 7$ T and $T = 600$ mK [11].*

When the magnetic atom is directly adsorbed on a metallic surface the spectral features are broadened, which means that it becomes harder to resolve excitations in energy. T. Balashov and co-workers succeeded to measure magnetic excitations on single Fe and Co adatoms on Pt(111), where the broadening caused by the coupling to the Pt(111) is very large and on the order of the excitation energy itself [12]. A. Khajetoorians *et al.* measured the magnetic excitations of individual Fe atoms on Cu(111), and attributed the observed spectral broadening to the decay of the magnetic excitations in the substrate via single-particle excitations or Stoner excitations where a spin-polarized electron-hole pair is produced [8]. Thus, without a decoupling layer, a magnetic adsorbate on a metallic substrate is subject to a stronger hybridization leading to a direct interaction with the continuum of electronic excitations of the metal.

If a metallic surface is magnetic, the spin direction of a magnetic atom is fixed by coupling it to the underlying substrate. The spin direction of the adatom and the type of the coupling, ferromagnetic (FM) or antiferromagnetic (AFM), can be determined by measuring the spin-polarized density of states above the adsorbate. D. Serrate *et al.* have recently imaged the spin direction of Co atoms on Mn/W(110) depending on their lateral position with respect to the underlying spin spiral [10]. Y. Yayon and co-authors reported that Fe and Cr atoms on Co islands exhibit out-of-plane magnetization and have an opposite sign of the exchange coupling between the adatom and the Co island. They found that Fe adatoms exhibit parallel spin polarization to the Co surface state while Cr adatoms show antiparallel spin polarization [9]. The authors assigned their observations to the FM and AFM alignment of the spin moment for Fe and Cr adatoms to a Co film. *Ab initio* calculations by B. W. Heinrich *et al.*, however, showed that the change of the spin polarization with respect to the pristine lead indicates a FM coupling between Co adatoms and a Co substrate [13]. M. Ziegler *et al.* reported about a change in sign of the spin polarization at the Fermi level E_{F} for Co and Cr atoms on Fe/W(110), and interpreted this phenomenon as a spin valve effect [14]. Furthermore, L. Zhou *et al.* observed an inversion of the spin polarization at the Fermi level E_{F} for Co atoms with respect to that of Co/Pt(111) [7]. They attributed their finding to the unique property of atomic protrusions due to the reduced coordination.

In my thesis, a system consisting of individual magnetic atoms adsorbed on a layer of non-magnetic material, a spacer layer, grown on a magnetic metallic substrate was designed (Fig. 1.1(a)). The focus of my study was an investigation of the properties of adatoms on different spacer layers, as well as their evolution with increasing spacer thickness (Figs. 1.1(b,c)).

*In the absence of a magnetic field, the magnetic excitations of a free Mn atom are in the range of eV, corresponding to typical values of the exchange energy in atoms [1].

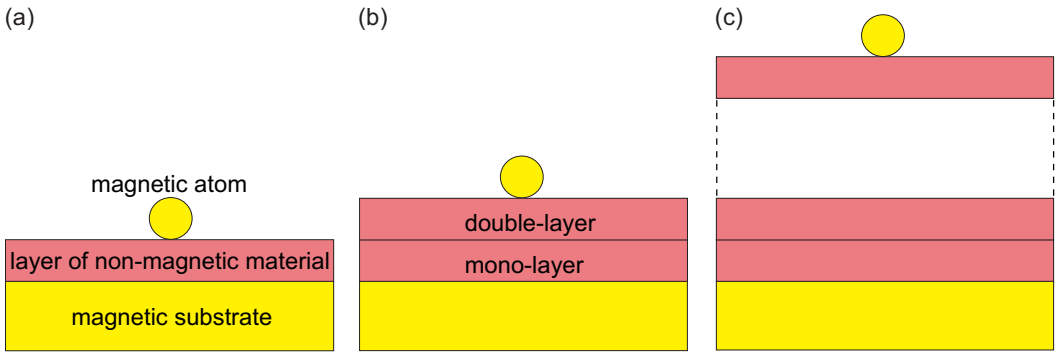

Figure 1.1: Schematic drawing of the system studied: (a) A magnetic atom is adsorbed on a layer of non-magnetic material, a spacer layer, grown on a magnetic substrate. (b) and (c) The same system but with variable spacer thickness.

In general, the spacer can be metallic or non-metallic. Magnetic domain structures of substrates have been recently observed when they were covered with a non-metallic spacer, i.e. the magnetic pattern of Co/Ir(111) was seen through one atomic layer of carbon, graphene [15], and a magnetic vortex structure of Fe/W(110) was probed through a sulfur overlayer [16]. Here, I investigated graphene on Ni(111) and single magnetic atoms such as Fe, Co and Cr adsorbed on top. The Ni(111) substrate was chosen since its domain structure was not yet well investigated, even though Ni(111) is a conventional ferromagnet. Furthermore, Ni(111) was reported to be a perfect substrate for the growth of graphene [17]. In case of metallic overlayers on magnetic systems, it has been shown that spin contrast of Fe/W(110) and Fe/Mo(110) can penetrate through thin Pb films [18] and small Au clusters [19], respectively. However, due to a quantum size effect of Pb structures [18; 20] and AuFe alloy formation [19], these systems are complicated for the current research focus on the magnetic coupling of single atoms through spacer layers of different thickness. Therefore, I used Pd as a metallic spacer material. Indeed, Pd possesses very intriguing properties: As bulk it is paramagnetic but its density of states which is strongly enhanced at E_{F}, only barely fails to satisfy the Stoner criterion [21]; Pd films get easily polarized in the vicinity of Fe or Co [22]. Individual Co atoms and a Co ML on Ir(111) were chosen as magnetic units. For a deeper understanding of the observations made in the SP-STM experiments spin-resolved density functional theory (DFT) calculations were performed.

This thesis is organized as follows: After a short introduction into the magnetic exchange interactions which play an important role in the magnetism of the studied systems (Chap. 2), the working principles of STM and SP-STM are covered (Chap. 3). The experimental setup and the magnetic tip preparation are described in Chap. 4. Chapter 5 is devoted to the sample systems Ni(111) and graphene/Ni(111). Chapter 6 deals with Pd adlayers on Co/Ir(111), and individual Co atoms adsorbed on top. Finally, summary and

perspectives are given in Chap. 7.

Chapter 2

Origin of magnetism

> Exchange interactions are nothing more than electrostatic interactions, arising because charges of the same sign cost energy when they are close together and save energy when they are apart.
>
> S. Blundell (Oxford University Press, 2010)

The force responsible for magnetism is called the exchange interaction. This chapter gives an overview of different types of exchange: (i) the intra-atomic exchange between electrons in one atom, which creates an atomic moment; (ii) the itinerant exchange in metals such as Ni; and (iii) the inter-atomic exchange, in particular interlayer exchange, which is responsible for long-range magnetic order. All interactions play an important role in the fundamental understanding of magnetism of the sample systems investigated in Chap. 5 and Chap. 6.

2.1 Intra-atomic exchange

Consider a simple model with just two electrons. The starting point is the Pauli principle which forbids the occupancy of a given orbital with two electrons of parallel ($\uparrow\uparrow$) spins but allows with those of antiparallel ($\uparrow\downarrow$) spins. The Pauli principle explains, for example, the periodic table of the elements: the 1s orbital of helium is occupied by a $\uparrow\downarrow$ electron pair, and an additional electron is not allowed to jump into the 1s shell. To realize a $\uparrow\uparrow$ orientation, which would show a net magnetic moment, one electron must occupy an excited one-electron orbital. The interaction between electrons is described by the

electrostatic or Coulomb interaction

$$V_{\mathrm{C}}(\mathbf{r}_1, \mathbf{r}_2) = \frac{e^2}{4\pi\epsilon_0 \mid \mathbf{r}_1 - \mathbf{r}_2 \mid}, \tag{2.1}$$

where $\mathbf{r}_1$ and $\mathbf{r}_2$ are spatial locations of electrons. Though there is no explicit spin-dependence in Eq. (2.1), the Coulomb interaction is larger for electrons in a common $\uparrow\downarrow$ orbital than for electrons in different $\uparrow\uparrow$ orbitals. In order to obtain a spin-dependent term, a quantum mechanical description of the electron is required.* The state of an electron is given by its wave function ψ: if the first electron is in state $\psi_a(\mathbf{r}_1)$ and the second electron is in state $\psi_b(\mathbf{r}_2)$, then the wave function for the joint state can be written as $\psi_a(\mathbf{r}_1)\psi_b(\mathbf{r}_2)$. Since electrons are indistinguishable, the square of the joint wave function must be invariant for the exchange of both electrons. To fulfill the Pauli principle, the wave function must be antisymmetric. Taking into consideration the spin $\mathbf{S}$ of the electrons, there are two possibilities: a symmetric spatial part ψ in combination with an antisymmetric spin part χ or an antisymmetric spatial part in combination with a symmetric spin part. The first situation represents a singlet state with $S_{\mathrm{total}} = 0$ whereas the second one is a triplet state with $S_{\mathrm{total}} = 1$. The corresponding total wave functions are given by

$$\Psi_{\mathrm{S}}(\mathbf{r}_1, \mathbf{r}_2) = \sqrt{1/2}[\psi_a(\mathbf{r}_1)\psi_b(\mathbf{r}_2) - \psi_a(\mathbf{r}_2)\psi_b(\mathbf{r}_1)] \cdot \chi_{\mathrm{S}}, \tag{2.2}$$

$$\Psi_{\mathrm{T}}(\mathbf{r}_1, \mathbf{r}_2) = \sqrt{1/2}[\psi_a(\mathbf{r}_1)\psi_b(\mathbf{r}_2) + \psi_a(\mathbf{r}_2)\psi_b(\mathbf{r}_1)] \cdot \chi_{\mathrm{T}}. \tag{2.3}$$

The total energy between electrons can be found by solving the Schrödinger equation

$$E\Psi = \mathbf{H}\Psi, \tag{2.4}$$

where $\mathbf{H}$ is a two-electron Hamiltonian. The energies of the singlet and triplet states therefore amount to

$$E_{\mathrm{S}} = \int \Psi^*_{\mathrm{S}}(\mathbf{r}_1, \mathbf{r}_2) H(\mathbf{r}_1, \mathbf{r}_2) \Psi_{\mathrm{S}}(\mathbf{r}_1, \mathbf{r}_2) \mathrm{d}\mathbf{r}_1 \mathrm{d}\mathbf{r}_2 \tag{2.5}$$

$$E_{\mathrm{T}} = \int \Psi^*_{\mathrm{T}}(\mathbf{r}_1, \mathbf{r}_2) H(\mathbf{r}_1, \mathbf{r}_2) \Psi_{\mathrm{T}}(\mathbf{r}_1, \mathbf{r}_2) \mathrm{d}\mathbf{r}_1 \mathrm{d}\mathbf{r}_2. \tag{2.6}$$

Taking into account the normalized spin parts of the singlet and triplet wave functions, i.e.

$$\mathbf{S}^2 = (\mathbf{S}_1 + \mathbf{S}_2)^2 = S_1^2 + S_2^2 + 2\mathbf{S}_1\mathbf{S}_2, \tag{2.7}$$

where $\mathbf{S}_1\mathbf{S}_2 = -\frac{3}{4}$ for the singlet state and $\mathbf{S}_1\mathbf{S}_2 = +\frac{1}{4}$ for the triplet state, the effective Hamiltonian can be written as

$$H = \frac{1}{4}(E_{\mathrm{S}} + 3E_{\mathrm{T}}) - (E_{\mathrm{S}} - E_{\mathrm{T}})\mathbf{S}_1\mathbf{S}_2. \tag{2.8}$$

*A detailed description of the Heisenberg exchange can be found in [23; 24].

The first term is constant and often included in other energy contributions. The second term depends on the spin. The *exchange constant* is defined by

$$J = (E_{\mathrm{S}} - E_{\mathrm{T}})/2 = \int \psi_a^*(\mathbf{r}_1)\psi_b^*(\mathbf{r}_2)H(\mathbf{r}_1,\mathbf{r}_2)\psi_a(\mathbf{r}_2)\psi_a(\mathbf{r}_1)\mathrm{d}\mathbf{r}_1\mathrm{d}\mathbf{r}_2. \quad (2.9)$$

Hence, the spin-dependent term in the effective Hamiltonian can be written as

$$H_{spin} = -2J\mathbf{S}_1\mathbf{S}_2. \quad (2.10)$$

If $J > 0$ then $E_{\mathrm{S}} > E_{\mathrm{T}}$, i.e. the triplet state with $S_{\mathrm{total}} = 1$ is energetically favored and the spin wave function is symmetric, hence the spins are aligned $\uparrow\uparrow$. If $J < 0$ then $E_{\mathrm{S}} < E_{\mathrm{T}}$, i.e. the singlet state with $S_{\mathrm{total}} = 0$ is energetically favored and the spin wave function is antisymmetric, hence the spins are aligned $\uparrow\downarrow$. Thus, J is defined as a half the energy difference between the $\uparrow\uparrow$ and $\uparrow\downarrow$ states, and is governed by the Coulomb repulsion which punishes $\uparrow\downarrow$ occupancies.

Since the spin of the electron is linked to its intrinsic magnetic moment $\mathbf{m}$ via

$$\mathbf{m} = -g\mu_{\mathrm{B}}\mathbf{S}/\hbar, \quad (2.11)$$

where g is the electron g-factor, μ_{B} is the Bohr magneton and $\hbar$ is the reduced Planck constant. The atomic magnetic moment is thus created by the intra-atomic exchange acting between inner-shell electrons.

2.2 Itinerant exchange

The magnetism of the transition metals such as Ni is caused by extended, delocalized, or *itinerant* electrons. The itinerant character manifests itself as the non-integer spin moments per atom, for example, 0.6 μ_{B} for Ni [24]. Since each spin carries a moment of 1 μ_{B}, these non-integer values cannot be of atomic origin but reflect the inter-atomic hopping of the moment-carrying electrons. Each delocalized electron is owned by all atoms, so that the moment per atom is not necessarily integer.

In non-magnetic metals, there are two equally populated $\uparrow$ and $\downarrow$ sub-bands; an applied magnetic field moves some electrons from the $\downarrow$ band to the $\uparrow$ band, leading to the corresponding spin polarization which is however small [24]. This is known as Pauli paramagnetism. In itinerant ferromagnets, due to the strong Coulomb interaction, the formation of narrow bands with hybridization energies smaller than about 1 eV and densities of states with sharp peaks of widths less than 1 eV is favorable. A refined version of these arguments is the *Stoner criterion*

$$ID(E_{\mathrm{F}}) \geq 1, \quad (2.12)$$

where I is the Coulomb integral or the Stoner parameter, and $D(E_{\mathrm{F}})$ is the density of states (DOS) at E_{F}. The DOS scales as $1/W$, where W is a bandwidth. Typical 3d metals have $I \approx 1\ eV$ and $W \approx 5\ eV$ [22]. The DOS is also

roughly proportional to $1/\sqrt{z}$, where z is the number of nearest neighbors. Physically, a reduced z leads to reduced hybridization, thus tends to the magnetic moment formation at surfaces and in small-scale nanostructures. The Stoner criterion defines a spontaneous splitting of the spin up and spin down bands without applying an external magnetic field. If the Stoner criterion is fulfilled, i.e. $ID(E_{\mathrm{F}}) \geq 1$, an element is ferromagnetic. If $ID(E_{\mathrm{F}}) < 1$, no spontaneous magnetization occurs, thus an element is paramagnetic. Some elements such as Pd and Pt do not satisfy the Stoner criterion but are close to ferromagnetism. The Stoner criterion, however, does not distinguish between paramagnetism and antiferromagnetism. Some values of $ID(E_{\mathrm{F}})$ are shown in Fig. 2.1 for the first 50 elements.

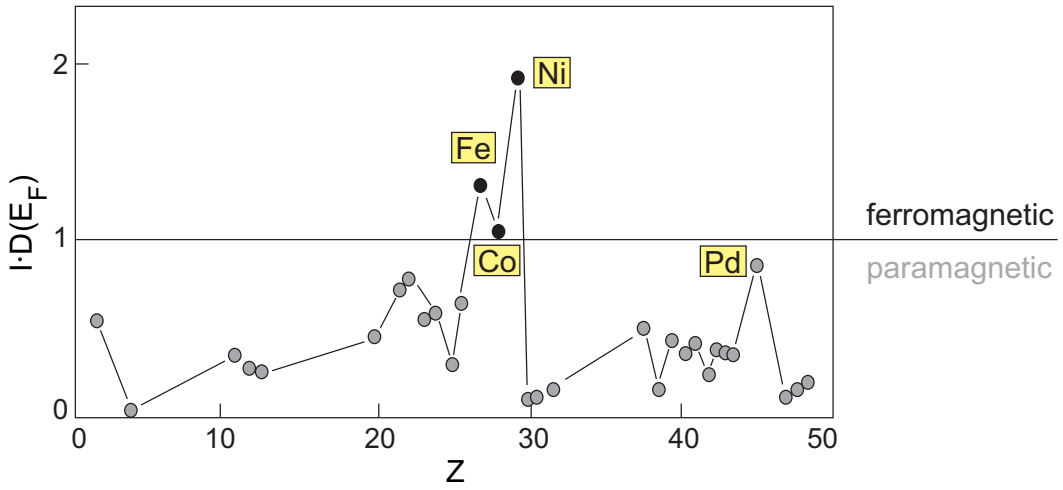

Figure 2.1: Values of $ID(E_{\mathrm{F}})$, where I is the Stoner parameter and $D(E_{\mathrm{F}})$ is the density of states at the Fermi level, as a function of the atomic number Z. Elements Fe, Co and Ni fulfill the Stoner criterion, thus are ferromagnetic (Source: [21]).

The Stoner criterion originates from an independent-electron approach where electrons in narrow bands exhibit a spin orientation to be parallel to the average spin. This mechanism is also referred to as Stoner exchange [22].

2.3 Inter-atomic exchange

In Section 2.1, Eq. (2.10) describes the interaction between two spins. However, it can be generalized for interactions between more than two spins, leading to the *Heisenberg model*

$$H_{spin} = -\sum_{ij} J_{ij}\mathbf{S}_i\mathbf{S}_j, \tag{2.13}$$

where J_{ij} is the exchange constant between i and j spins. The factor of 2 is omitted because the summation includes each pair of spin twice. The Heisenberg Hamiltonian in Eq. (2.13) describes, in general, the interaction between

two nearest-neighboring localized spins. If the spins are on different atoms, the exchange is referred to as inter-atomic. In this case, $J > 0$ indicates a ferromagnetic (FM) alignment of spins, whereas $J < 0$ means an antiferromagnetic (AFM) spin configuration. Both intra- and inter-atomic exchange have the same origin, but intra-atomic exchange tends to be stronger, on the order of 1 eV or 10000 K, compared to typical inter-atomic exchange of about 0.1 eV or 1000 K.

Depending on the distance between the spins, *direct* and *indirect* exchange can be distinguished. If electrons of neighboring magnetic atoms interact directly without the need for an intermediate atom, exchange is direct. If the overlap between neighboring magnetic orbitals is insufficient, direct exchange is not the dominating mechanism for magnetic properties. For this class of systems indirect exchange is responsible for magnetism. Indirect exchange significantly depends on the kind of magnetic material.

Superexchange originates between non-neighboring magnetic ions and is mediated by a non-magnetic ion located in between the magnetic ions. An example is the antiferromagnetic ionic solid MnO [21].

Double exchange arises in oxides where the magnetic ions exhibit mixed valencies. One example is given by magnetite Fe_3O_4 which includes Fe^{2+} as well as Fe^{3+} ions [21].

Rudermann-Kittel-Kasuya-Yosida (RKKY) exchange occurs, in general, between magnetic moments coupled via conductance electrons [25; 26]. There are two types of systems where it takes place: (i) magnetic moments are separated with a non-magnetic metallic spacer, and (ii) magnetic moments are diluted in a non-magnetic metallic host. RKKY exchange is long range and anisotropic which can result in a complicated spin arrangement. Additionally, it possesses an oscillating behavior. The characteristic feature of the interaction is the distance dependent exchange integral $J_{\mathrm{RKKY}}(r)$:

$$J_{\mathrm{RKKY}}(r) = J_0 \frac{\sin(2k_{\mathrm{F}}r) - r\cos(2k_{\mathrm{F}}r)}{(2k_{\mathrm{F}}r)^4}, \tag{2.14}$$

where k_{F} is the Fermi wavelength. $J_{\mathrm{RKKY}}(r) > 0$ means a FM coupling between magnetic moments whereas $J_{\mathrm{RKKY}}(r) < 0$ results in an AFM configuration.

In case of layered magnetic materials separated by a non-magnetic metallic spacer of thickness n, RKKY exchange is referred to as *interlayer exchange*. The dependence of interlayer exchange is different and described as follows:

$$J_{\mathrm{RKKY}}(n) \propto \frac{\sin(2k_{\mathrm{F}}n)}{n^2}, \tag{2.15}$$

Figure 2.2(a) schematically illustrates the RKKY behavior of the interlayer exchange coupling between two FM thin films.

In my thesis, I worked with a system similar to the type (i), therefore I will focus on the interaction for this system in more detail. If a spacer is non-metallic, the coupling is non-oscillatory and decays exponentially with spacer

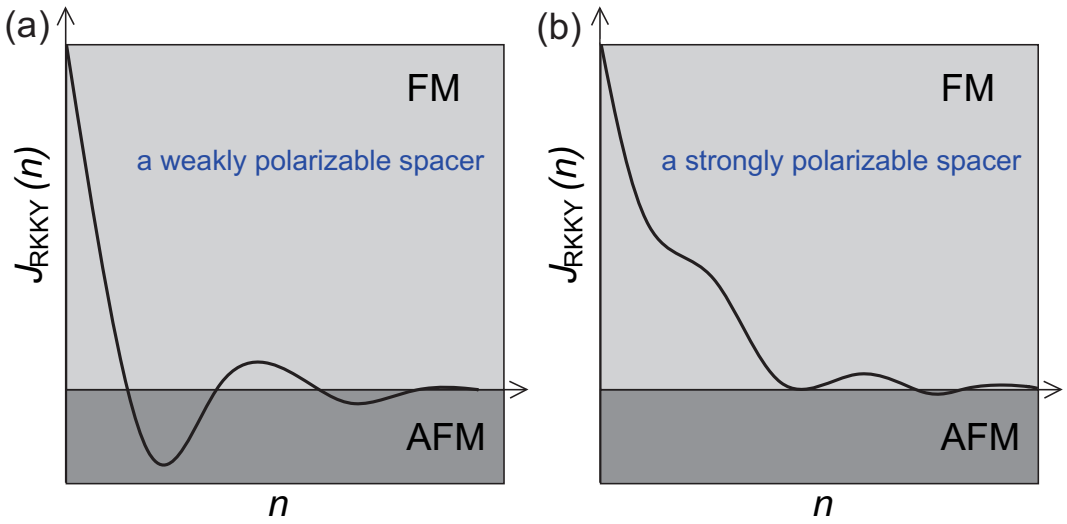

Figure 2.2: Schematic drawing of interlayer exchange coupling between two ferromagnetic thin films exhibiting a RKKY behavior for: (a) a weakly polarizable (for example, Cu) spacer, and (b) a strongly polarizable (for example, Pd) spacer. Depending on the thickness of a spacer n a ferromagnetic ($J_{\mathrm{RKKY}}(n) > 0$) or antiferromagnetic ($J_{\mathrm{RKKY}}(n) < 0$) alignment occurs.

thickness [25]. In Chap. 5, I exploit a graphene sheet to magnetically decouple adsorbed Fe, Co and Cr atoms from an underlying Ni substrate. However, due to a self-terminated monolayer growth of graphene, the dependence of the magnetic coupling on the thickness of the spacer fails. If a spacer is metallic, a multi-layer growth of material is possible. Depending on polarization properties of the metallic spacer, the oscillatory behavior of the RKKY coupling differs. In case of a *weakly polarizable* spacer such as Cu, Al, Au and Ag, the conductance electrons scattered from a magnetic surface form spin-polarized interference patterns inside the spacer due to the quantum confinement [25; 26]. If the spacer is *strongly polarizable* like Pd and Pt, the conductance electrons form extended polarization clouds consisting of very small induced moments on atomic sites of the spacer, in the vicinity of the magnetic surface [27; 28]. The main difference between the weakly and strongly polarizable spacer is that the intra-atomic exchange interaction among d electrons is very strong in the latter case. This has a dramatic effect on the spacer thickness dependence of the interlayer exchange coupling, as shown in the previous study of a Fe/Pd$_n$/Fe layer system [29]: by varying Pd spacer thickness they found that the oscillatory behavior of the coupling between the magnetic layers is superimposed on the exponentially decreasing FM contribution (Fig. 2.2(b)). In Chap. 6 I show that the polarization effect of a Pd spacer plays a crucial role in the magnetic coupling between single Co adatoms and a Co layer underneath.

Chapter 3

Scanning tunneling microscopy

This chapter introduces fundamental aspects of scanning tunneling microscopy (STM) which allow to investigate electrically conducting surfaces down to the atomic scale, and spin-polarized scanning tunneling microscopy (SP-STM) which opens a new perspective to a new class of experiments with focus on atomic scale structures.

3.1 Tunneling effect

A convenient starting point for the theory of STM is the *tunneling effect* in one dimension. The tunneling effect is a purely quantum mechanical phenomenon due to the wave-particle dualism which is unknown to classical physics. In classical theory, an electron with energy E moving in a potential barrier of finite height U_0 and finite width d can overcame a barrier only if $E > U_0$, otherwise the electron is reflected (see Fig. 3.1(a)). In quantum mechanics, the electron has, however, a non-zero probability of tunneling through the barrier of finite height (Fig. 3.1(b)). The electron can be described by a wave function $\psi(z)$ that has to fulfill continuity conditions within the three different regions:

region I: $z < 0$, $U(z) = 0$
region II: $0 \leq z \leq d$, $U(z) = U_0$
region III: $z > d$, $U(z) = 0$

to solve the time-independent Schrödinger equation

$$(-\frac{\hbar^2}{2m_\mathrm{e}}\frac{\mathrm{d}^2}{\mathrm{d}z^2} + U(z))\psi(z) = E\psi(z), \tag{3.1}$$

where m_e is the electron mass and $\hbar$ is the reduced Planck constant. The respective solutions for the different regions are

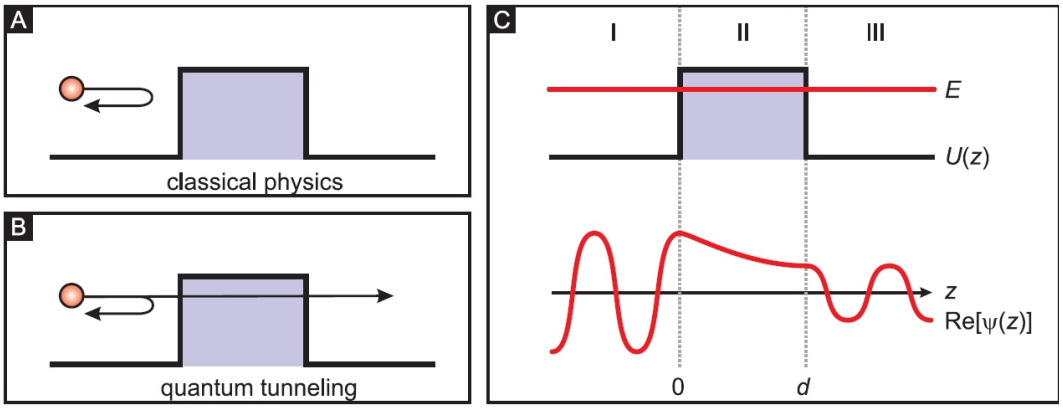

Figure 3.1: Tunneling effect in one dimension: (a) In classical theory, an electron moving in a potential will be reflected at a potential barrier if the electron energy is smaller than the height of the barrier. (b) In quantum mechanics, however, the electron has a non-zero probability of tunneling through the barrier of finite height. (c) In quantum mechanics, the electron can be also described by a wave function $\psi(z)$ that has to fulfill continuity conditions within the three different regions to solve the time-independent Schrödinger equation. (Source: [30])

region I: $\psi_1 = \exp(\mathrm{i}kz) + A\exp(-\mathrm{i}kz)$
region II: $\psi_2 = B\exp(-\kappa z) + C\exp(\kappa z)$
region III: $\psi_3 = D\exp(\mathrm{i}kz)$

with the two constants $k = \sqrt{\frac{2m_\mathrm{e}E}{\hbar^2}}$ and $\kappa = \sqrt{\frac{2m_\mathrm{e}(U_0-E)}{\hbar^2}}$, where k is the wave number and κ is the decay constant. As it is shown in Fig. 3.1(c), for the region I, the wave function of the electron has a plane wave character. Inside the region II, the electron wave function penetrates into the classically forbidden barrier, where it decays exponentially. This means that there is *always* a finite probability for the electron to cross a potential barrier as long as $U_0 < \infty$.

To derive values for remaining constants A, B, C and D, $\psi(z)$ and its first derivative $\frac{\mathrm{d}}{\mathrm{d}z}\psi(z)$ are required to be continuous for all z, that can be obtained by matching the partial solutions found for the respective regions at the points $z = 0$ and $z = d$ (*wave matching method*). As a result, one can gain an exact expression for the transmission coefficient which is the ratio of the transmitted and the incident flux j_t and j_i

$$T \equiv \frac{j_\mathrm{t}}{j_\mathrm{i}} = |D^2| = \frac{1}{1 + \frac{(k^2+\kappa^2)^2}{(4k^2\kappa^2)} \cdot \sinh^2(\kappa d)}. \tag{3.2}$$

In the limit of $\kappa d \gg 1$ the transmission coefficient T can be simplified to

$$T \approx \frac{16k^2\kappa^2}{(k^2+\kappa^2)^2} \cdot \exp(-2\kappa d). \tag{3.3}$$

The key point of the obtained approximation is the exponential dependence

of T on the width d of the potential barrier. In STM, a tunnel current is measured between two metallic electrodes, namely a tip and a sample, through a vacuum barrier. Inside metallic electrodes, electrons can be described within the free-electron-gas model, where all electronic states are occupied up to E_F (for simplicity, $T = 0$ K). The height U_0 of the vacuum barrier is given by the work function Φ of the metallic electrode, i.e. the energy required to extract an electron out of the surface into the vacuum. The width of the barrier is given by the tip-sample distance. For a typical metal the work function is $\Phi \approx 4$ eV, resulting in $\kappa \approx 1$ $\mathring{A}^{-1}$. As a consequence, the tunneling current decreases by about a factor of 10, if the tip-sample distance is increased by about 1 $\mathring{A}$. Thus, STM is a very sensitive technique. This explains high resolution of STM images where structures on the nanometer scale and individual atoms adsorbed on surfaces can be observed.

3.2 Working principle

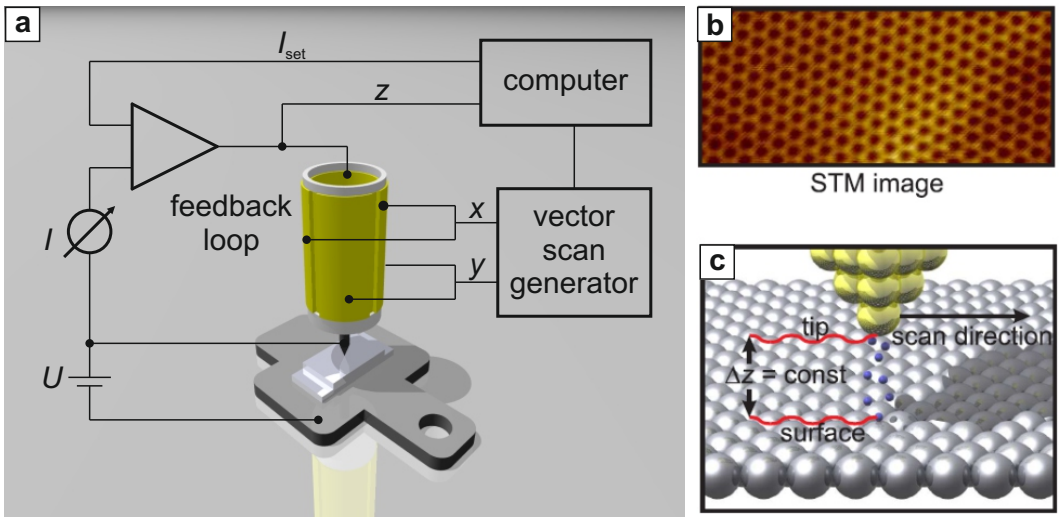

Figure 3.2: Working principle of STM: (a) The tunnel current is kept constant at a set point I_{set} using a feedback loop while the tip scans laterally across the surface by applying voltages to the $x-$ and $y-$electrodes of the tube scanner. The feedback loop adjusts the tip height until the measured current is identical to the set point. (b,c) A computer records the $\Delta z(x, y)$ points and constructs a topographic map out of those height changes in a color code. (Sources: (a) from [31], (b,c) from [30])

As it is shown in the previous section, the tunnel current is extremely sensitive to the tip-sample separation. This means that the tip positioning has to be very accurate. This can be accomplished by using piezoelectric actuators to control the tip-sample distance as well as the lateral position of the tip above the sample surface. A schematic illustration of the STM set-up used in this study is shown in Fig. 3.2. The working principle of the piezoelectric effect

is the following: the outer side of a piezoelectric tube scanner is covered by four electrodes (x_+, x_-, y_+, y_-), whereas the inner side is connected by one single electrode (z). When a d.c. voltage is applied, for example, to opposite x electrodes, and the z electrode is grounded or has a constant value, the piezoelectric material elongates at one electrode and contracts at the other, which leads to the bending of the tube scanner. As a result, the tip is moved along the x direction. The same principle can be used to control the tip motion along the y direction. However, if a voltage is applied between the inner and all outer electrodes, the whole tube scanner elongates or contracts depending on the polarity. This effect moves the tip along the z direction, thus, can be used to adjust the distance between the tip and the sample.

To record an STM image, the tunneling current is usually kept constant at a chosen set point I_{set} (*constant-current mode*) by using a feedback loop to control the tip-sample distance. While the tip is scanning above the sample surface, the z component of the tip position is collected as a function of the lateral position (x, y), providing a measure of a sample surface contour. Color coding of the $\Delta z(x, y)$ gives an impression about the sample surface topography.

3.3 Topography and spectroscopy

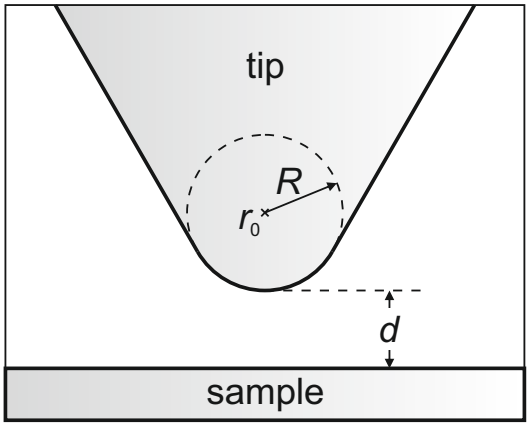

Figure 3.3: Tip and sample geometry in the Tersoff-Hamann model, where d denotes the tip-sample distance, R and r_0 indicate the effective tip radius and the center of the tip curvature, respectively. (Source: [31])

The simple model introduced in Section 3.1 shows the exponential dependence of the tunnel current on the tip-sample separation. However, this model is only one dimensional whereas STM experiments are mostly carried out in three dimensions. Also, it fails to explain a dependence of the tunneling current on the electronic structure of the two electrodes.

To describe appropriately the tunneling process in STM, Tersoff and Hamann developed a more precise model [32; 33], which is based on Bardeen's

formalism derived from the first-order time-dependent perturbation theory [34]. In the tunneling geometry of the Tersoff-Hamann model, the tip is approximated by a sphere (see Fig. 3.3), and only s-type wave functions contribute to the tunneling process. Under assumption of low temperatures and small bias voltages U such that only states at E_F need to be considered, one arrives at

$$I \approx U \cdot n_\mathrm{t}(E_\mathrm{F}) \cdot \exp(2\kappa R) \cdot \sum_{\upsilon} \mid \psi_\upsilon(\vec{r}_0) \mid^2 \cdot \delta(E_\upsilon - E_\mathrm{F}), \tag{3.4}$$

where n_t is the constant density of states of the tip. The quantity

$$n_\mathrm{s} = \sum_{\upsilon} \mid \psi_\upsilon(\vec{r}_0) \mid^2 \cdot \delta(E_\upsilon - E_\mathrm{F}), \tag{3.5}$$

is the local density of states (LDOS) of the surface at E_F, evaluated at the center of curvature r_0 of the effective tip. The sample wave functions decay exponentially into the vacuum

$$\mid \psi_\upsilon(\vec{r}_0) \mid^2 \approx \exp(-2\kappa s), \tag{3.6}$$

where the tip-sample distance is defined by $s = d + R$. The most important result of the Tersoff-Hamann model is that the tunneling current is determined by sample properties alone while the role of the tip is reduced simply to that of a probe. Thus, STM images measured in the constant-current mode can be interpreted as contour maps of constant sample LDOS, which follow the topography of the sample surface. In this way, the details of the surface geometry like step edges, defects, surface reconstructions etc. can be imaged.

The tunneling process is, however, described in the limit of low bias voltages U. When U is increased, the Tersoff-Hamann model can be extended to the case of a tunneling current integrated over an energy range

$$I \approx \int_0^{eU} U n_\mathrm{t}(E_\mathrm{F} - eU + E) n_\mathrm{s}(E_\mathrm{F} + E) T(E_\mathrm{F} + E, E_\mathrm{F} - eU + E) \mathrm{d}E, \tag{3.7}$$

with a transmission factor

$$T(E_\mathrm{F} + E, E_\mathrm{F} - eU + E) = \exp\left[-s\sqrt{\frac{4m_\mathrm{e}(\Phi_\mathrm{t} + \Phi_\mathrm{s} - 2E_\mathrm{F} + eU - 2E)}{\hbar^2}}\right], \tag{3.8}$$

where Φ_t and Φ_s are the work functions of a tip and a sample, respectively.

Figure 3.4 schematically illustrates the tunneling process described by Eq. (3.7), where the tip-sample system is shown for three different situations. In these diagrams, E_F and E_V are the Fermi energy and the vacuum energy, respectively. If no voltage U is applied (Fig. 3.4(a)), sample and tip have the same E_F, and the same number of electrons tunnel from the tip to the sample or vice versa. This leads to a vanishing net tunnel current. In case of $U < 0$, i.e. a negative bias voltage is applied to the sample (Fig. 3.4(b)), E_F of the

sample is shifted to a higher value with respect to that of the tip. This results in a non-zero tunnel current where electrons of occupied states of the sample can tunnel into unoccupied states of the tip. The situation is reversed for $U > 0$ (Fig. 3.4(c)), where E_F of the sample is shifted to a lower value with respect to that of the tip, and electrons tunnel from occupied states of the tip to unoccupied states of the sample. If the sample and the tip have a constant (or flat) LDOS, the tunnel current is directly proportional to the applied bias voltage ($eU << \Phi$) giving rise to an ohmic behavior of the tunnel junction.

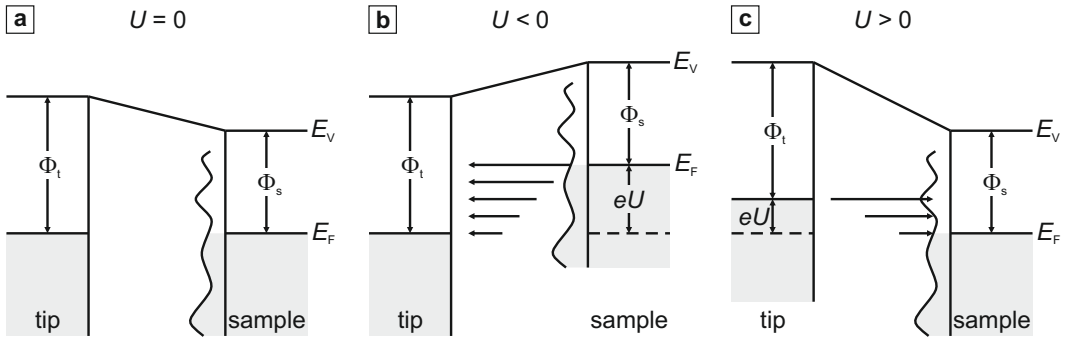

Figure 3.4: Diagrams of tip-sample systems in a tunnel contact: (a) For $U = 0$, no tunnel current is flowing since the same number of electrons tunnels from the tip to the sample as vice versa. (b) and (c) With $U \neq 0$, a tunnel current is non-zero and flows from the sample to the tip or vice versa, depending on polarity.(Source: [31])

Under the approximation of Tersoff and Hamann, differentiation of Eq. (3.7) with respect to the applied voltage U yields the *differential conductance*

$$\frac{\mathrm{d}I}{\mathrm{d}U}(U) \approx n_\mathrm{t}(E_\mathrm{F}) n_\mathrm{s}(E_\mathrm{F} + eU) T(E_\mathrm{F} + eU, E_\mathrm{F}) \tag{3.9}$$

Assuming T varies monotonically with U, $\mathrm{d}I/\mathrm{d}U$ is a good measure of n_s at an energy equal to eU.

The differential conductance $\mathrm{d}I/\mathrm{d}U$ is the central quantity we are interested in since it carries important information about electronic properties of the sample. Experimentally, $\mathrm{d}I/\mathrm{d}U$ is measured by stabilizing the tip at I_stab and U_stab above the surface area with spatial coordinates (x_0, y_0), switching off the feedback loop, and sweeping the bias voltage. This method is referred to as *single point spectroscopy*. During the voltage sweep an $I(U)$-curve is recorded while the tip position z remains constant. By numerical differentiation of the $I(U)$-curve, the respective $\mathrm{d}I/\mathrm{d}U(U)$ quantity can be obtained. In this work, $\mathrm{d}I/\mathrm{d}U$ was detected by using a lock-in technique: while ramping the d.c. voltage, a small a.c. signal (U_mod=5...30 mV, f_mod=2...5 kHz) is added, and the respective in-phase current modulation, i.e. $\mathrm{d}I/\mathrm{d}U$ signal, is measured by a lock-in amplifier. Signal variations due to noise are effectively filtered since they do not follow the constant modulation frequency and phase. As a result, a measured $\mathrm{d}I/\mathrm{d}U(U)$ curve provides a spectrum of LDOS of the sample.

To investigate electronic properties of a sample with lateral resolution, a $\mathrm{d}I/\mathrm{d}U$ *spectroscopy map* is measured. In this case, the LDOS is recorded at every position (x, y) of the surface for a chosen bias voltage. This map can be compared to the simultaneously acquired topography, thus, structural and electronic properties can be correlated directly.

If a spectroscopic $\mathrm{d}I/\mathrm{d}U(U)$ curve with a number of points l is taken at each point of a rectangular grid with a size $(m \times n)$, a measurement is called *spectroscopic field*, and the result has a shape $(m \times n \times l)$. Such a spectroscopic field allows investigating the spatial extent and energetic development of spectroscopic features of the surface studied. A common way to display obtained data is a form of slices where $\mathrm{d}I/\mathrm{d}U$ values of the grid are shown at one voltage U. A drawback of these measurements is that they can take significant amounts of time, on the order of hours.

It is important to note that the expression (3.9) was obtained under the assumption of the constant LDOS of the tip. In a real experiment, the electronic structure of the tip may, however, vary. This has to be taken into account when spectroscopic data is analyzed.

3.4 Spin-polarized scanning tunneling microscopy

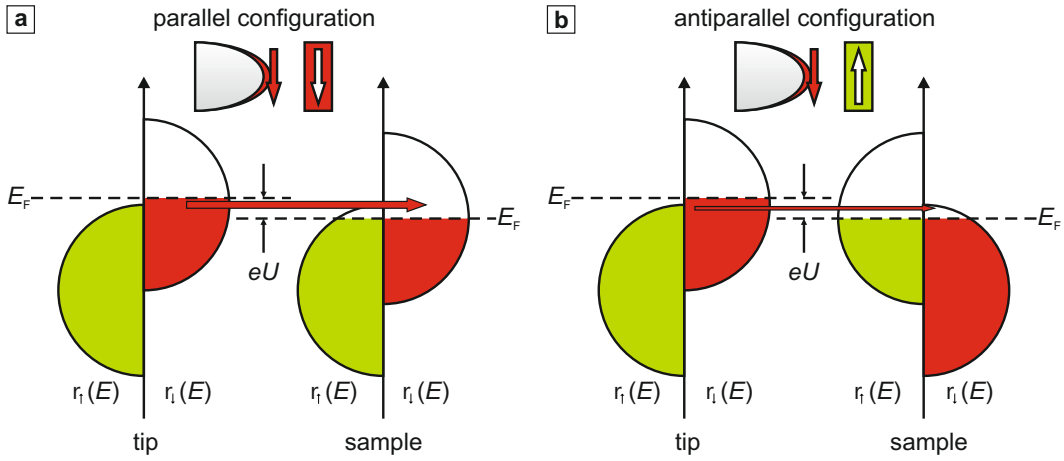

Figure 3.5: Scheme of SP-STM: (a) Parallel configuration of tip and sample magnetizations, where only spin ↑ electrons of occupied states of the tip can tunnel into unoccupied spin ↑ states of the sample. (b) In case of antiparallel configuration, the number of unoccupied spin ↑ states of the sample is reduced, which leads to a reduced tunneling current. (Source: [31])

The concept of SP-STM is based on measuring of the tunnel current flowing between two *magnetic* electrodes (*the tunneling magneto-resistance*). In this case, in addition to the electronic properties of the electrodes, the tunnel

current depends on their magnetic properties. Figure 3.5 schematically shows the principle of SP-STM for parallel and antiparallel configuration between tip and sample magnetizations. Each magnetic electrode is characterized by its spin-split density of states of majority ($r_\uparrow(E)$) and minority ($r_\downarrow(E)$) electrons, which leads to a spin polarization at E_F

$$P(E_\mathrm{F}) = (\rho_\uparrow(E_\mathrm{F}) - \rho_\downarrow(E_\mathrm{F}))/(\rho_\uparrow(E_\mathrm{F}) + \rho_\downarrow(E_\mathrm{F})). \tag{3.10}$$

In case of parallel configuration, spin $\uparrow$ electrons from occupied states of the tip tunnel into unoccupied spin $\uparrow$ states of the sample. For antiparallel configuration, the number of unoccupied states of the sample is decreased which leads to a reduced tunnel current. Thus, the tunnel current is larger for parallel configuration than for the antiparallel one in this case.

J. C. Slonczewski treated the tunneling between two magnetic electrodes theoretically [35]. In the limit of vanishing bias voltage U and under the assumption of a free-electron behavior of the conduction electrons, the spin-polarized tunnel current I_sp between two magnetic electrodes can be described as follows

$$I_\mathrm{sp} = I_0[1 + P_\mathrm{t}P_\mathrm{s} \cdot \cos(\vec{M}_\mathrm{t}, \vec{M}_\mathrm{s})], \tag{3.11}$$

where I_0 is the non-polarized current, P is the polarization and $\vec{M}$ is the magnetization direction of the tip (t) and the sample (s), respectively. The cosine dependence of I_sp on an angle θ between magnetic moments of two planar electrodes was for the first time verified experimentally by M. Julliere in 1975 [36]. R. Wiesendanger showed that the tunneling magneto-resistance can also be measured in STM geometry [37]. Since more than 10 years, SP-STM is a well-established technique to investigate magnetic systems down to the atomic scale. Recently, it has been shown that new classes of experiments such as atom manipulation [10; 38], atom magnetometry [6], spin-flip processes of a localized spin [39; 8] and spin relaxation [40] can be achieved with SP-STM.

Chapter 4

Instrumental setup and tip preparation

This chapter introduces an ultra-high vacuum (UHV) system which was used to prepare our systems studied, and room- and low-temperature STMs used for measurements. The preparation of magnetic tips crucial for SP-STM experiments is described in the last section.

4.1 Ultra-high vacuum system

Within my PhD thesis, I investigated graphene/Ni(111), Pd adlayers on Co/Ir(111), and single magnetic atoms adsorbed on top, by means of SP-STM. Since STM is a very sensitive technique, it is required to keep samples clean and uncontaminated during measurement time, that can last several hours or even days. Under ambient conditions, metallic surfaces tend to immediately form an oxide layer. In vacuum with a base pressure of $p \approx 10^{-6}$ mbar, a clean surface is completely covered by adsorbates from the residual gas within 1 s [41]. All experiments in this work were, therefore, performed under ultra-high vacuum (UHV) conditions, i.e at $p < 10^{-10}$ mbar.

UHV is maintained by means of a variety of vacuum pumps with different working principles. Turbo-molecular pumps with auxiliary roughing pumps are able to remove most of the air from the system and achieve pressures of $p < 10^{-6}$ mbar within a short time. Ion-getter pumps and titanium sublimation pumps are very effective at low pressures and able to reach UHV down to 10^{-10} mbar or better.

The measurements presented in Chap. 5 and Chap. 6 were conducted in the UHV system shown in Fig. 4.1. The central part of the system is a distribution (Dist) chamber which connects all other chambers: parking spot (P),

load-lock (LL), analysis (Ana) chamber, preparation (Prep) chamber, satellite (Sat) and molecular-beam epitaxy (MBE) chambers; also it has an access to low-temperature STMs (^{4}He and ^{3}He cryostats). Tip and samples are transferred between the chambers by linear manipulations. A parking spot serves as a place to store different samples and tips. The load-lock allows to introduce new samples and tips. The analysis chamber is equipped with the standard surface characterization units such as Auger electron spectroscopy (AES) to investigate chemical composition of samples, and low energy electron diffraction (LEED) to gain insight into the symmetry of crystal surfaces used. This chamber is also accommodated with a high energy ($E \approx 0.8 - 4$ keV) Ar^+ sputter gun to clean sample surfaces. In the preparation chamber, samples and tips can be flashed up to $T \approx 2000$ K by using an electron beam heater. With a mounted dosing valve, samples can be annealed in oxygen atmosphere to get rid of carbon contamination. The MBE chamber is used for deposition of magnetic (Fe, Co, Cr, Mn, Ni) and non-magnetic (Pd, Ag, Pt) materials onto the clean surfaces or tips. It is additionally equipped with a room-temperature STM for growth studies (see Section 4.3). The UHV system has been recently extended with the satellite chamber which is described in Section 4.2 in details, and a new ^{3}He cryostat for SP-STM measurements at $T < 1$ K and magnetic fields up to $B = 9$ T.

To prevent vibrations, the whole system is installed in an acoustically shielded laboratory with a foundation which is completely separated from the rest of the building. In addition, the UHV system is supported by a table with pneumatic damping.

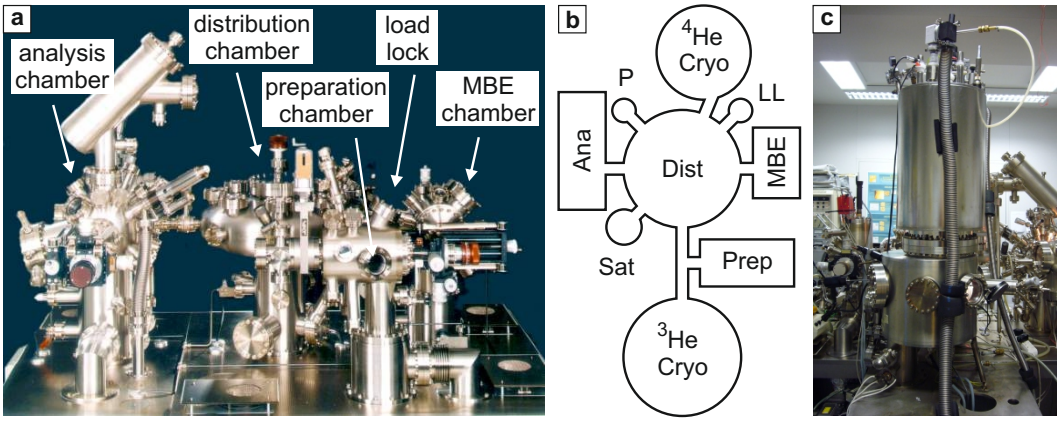

Figure 4.1: The UHV system used in this thesis: (a) Side view of the multi-chamber system consisting of distribution, analysis, preparation and MBE chambers for *in vacuo* preparation, and load-lock to introduce new tips and samples. (b) Schematic drawing of the top view of the system with all extensions. A parking place for tips and samples (P), a satellite chamber (Sat) described in Section 4.2 and two chambers for low-temperature STMs (^{4}He and ^{3}He cryostats) have been attached to the main system displayed in (a). ^{4}He cryostat which contains the low-temperature STM is presented in Section 4.3. (Source: [31])

4.2 Satellite chamber

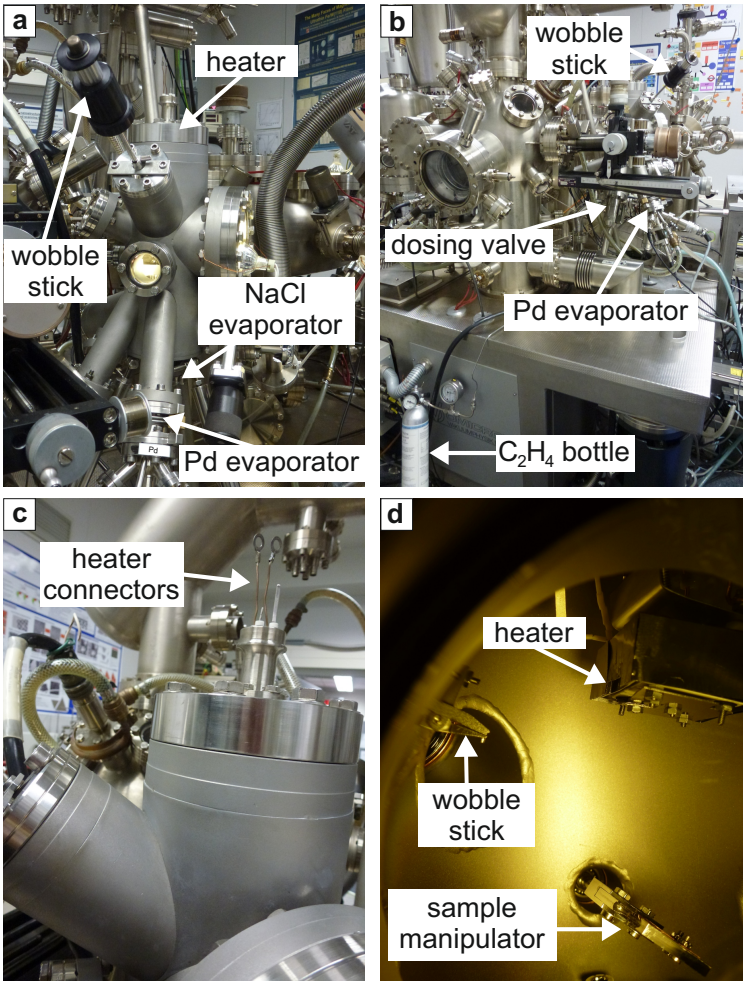

Figure 4.2: Satellite chamber used to prepare sample systems studied in this thesis: (a-c) Side views of the chamber equipped with a boralectric heater, an electron beam evaporator with a Pd rod, an evaporator filled with NaCl grains and a C_2H_4 dosing valve. A wobble-stick is used to insert samples into the heater. As shown in (c), all connectors of the heater are mounted on the outside of the chamber. (d) UHV parts of the chamber.

The satellite or a small preparation chamber shown in Fig. 4.2 was designed by M. Menzel, built by me and Y. Yoshida, and used to fabricate sample systems studied in this thesis. The main facilities equipped in this chamber are a boralectric heater, an electron beam evaporator with a Pd rod, an evaporator filled with sodium chloride (NaCl) grains and a dosing valve to introduce ethylene (ethene or C_2H_4). Advantages of the chamber are as follows: a preparation of carbon-contained samples such as graphene/Ni(111) separately from the UHV system, a deposition of materials directly on hot substrates, and a precise temperature control to heat samples. However, due to the design of

the chamber, the heating of samples at high temperatures ($T > 1000°C$) for a long time ($t > 3$ min) is not possible.

To clean a single Ni(111) crystal and prepare graphene/Ni(111), the boralectric heater was used. It is UHV compatible, almost chemically inert, exhibits good mechanical stability, high power density (about 45 W/cm^2), high heating rates ($> 100°C/s$) and temperatures up to $T = 1800°C$. The heater was supplied as a complete flange mounted unit from TecTra [42].

The main part of the heater is a heating element which consists of a pyrolytic boron nitride plate (PBN) covered with a thin conducting film of pyrolytic graphite (PG) and a dielectric layer of PBN added on top. The outer shape of the element is rectangular with two contacts exposed to the PG film on one diagonal and insulated through holes for sample mounting on the other diagonal (see Fig. 4.3). The center part is the heated zone. At a side there is a small (about 500 μm in diameter) hole for a thermocouple. One side of the PBN/PG element is shielded with two Mo foils and contacted by a current-thermocouple feedthrough. All connectors are mounted on the outside of the chamber, as shown in Fig. 4.2(c). Power is supplied by a standard Proportional-Integral-Derivative (PID) controller. The heater is installed such that the contacts are looking towards the heat shields. With the design of the heater, a sample is transfered up-side down and placed in between a metallic Mo plate and the PBN/PG heating element.

To deposit Pd material, Co/Ir(111) samples were inserted in the boralitic heater due to the geometry of the satellite chamber. Since the deposition was performed at room temperature, the heating power was switched off.

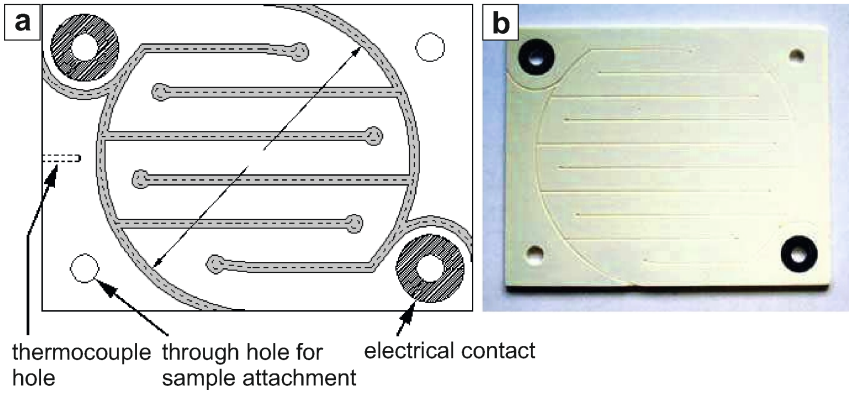

Figure 4.3: (a) Schematic drawing and (b) a picture of a boralitic heating element. (Source: [42])

4.3 Scanning tunneling microscopes

As it was mentioned in the previous section, the MBE chamber is accommodated with the room-temperature STM (RT-STM) which is shown in

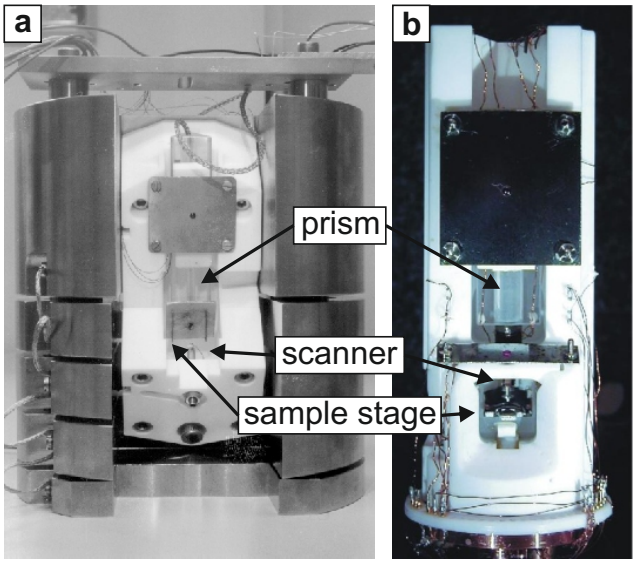

Figure 4.4: The STMs exploited for studies in this thesis: (a) Room-temperature STM used for sample characterization and morphology investigations. (b) Low-temperature STM where SP-STM and SP-STS measurements were conducted. (Source: [43; 31])

Fig. 4.4(a). It is a home-built microscope designed by C. Witt [44], and usually used for the sample characterization and the growth studies of deposited materials on surfaces. A STM tip is made from a 1 mm PtIr wire. The tip is, however, not exchangeable, which means that care has to be taken to prevent any mechanical contact with the tip. A big advantage of the STM is that there is a 60° angle of the sample and the tip axes, that allows a vertical as well as lateral motion of the sample with respect to the tip. With such a geometry, it is possible to deposit material onto the sample directly sitting in the STM, without affecting the tip. Furthermore, the same area of the surface can be imaged after the deposition, thus, samples can be investigated at different coverage regimes. Since the MBE is equipped with four electron beam evaporators, three of them are pointing at the sample position, growth studies of various systems are possible.

The other system used in this study is the low-temperature STM (LT-STM) shown in Fig. 4.4(b). It is a home-built machine designed and built by O. Pietzsch [45]. The STM is located in the liquid helium or ^{4}He ($T \approx 4.2$ K) bath cryostat enclosed with liquid helium and liquid nitrogen ($T \approx 77$ K) radiation shields. In thermal equilibrium, the microscope temperature is $T \approx 8$ K. The temperature is detected directly on the sample stage, and kept for about 40 h after filling. The STM is also surrounded by a superconducting split magnetic coil which produces a homogeneous magnetic field perpendicular to the sample surface, up to $B = \pm 2.5$ T. A particular feature of this design of the STM is a tip exchange mechanism which was built by A. Kubetzka to perform SP-STM measurements [46]. The capability to rotate a sample such that it is in line

with a triple evaporator installed in the ^{4}He ($T \approx 4.2$ K) cryo-chamber allows depositing single Fe, Co or Cr atoms on cold surfaces ($T_{\max} =$ K) to prevent diffusion. Compared to the RT-STM, the LT-STM has the advantage of a much higher energy resolution ($k_B \cdot (300\,K) \approx 25\,\text{meV}$ vs. $k_B \cdot (8\,K) < 1\,\text{meV}$) as well as reduced thermal drift between tip and sample [31].

4.4 Magnetic tip preparation

Successful SP-STM and SP-STS measurements strongly depend on electronic and magnetic stability of the tips offering simultaneously a high spatial resolution and a high spin polarization. All experiments shown in this work were performed with W-tips coated with magnetic material of either Cr or Fe. A typical magnetic tip preparation is as follows. The tip is sharpened from a 0.75 mm diameter polycrystalline W wire by electrochemical a.c.-etching in sodium hydroxide (NaOH) solution. After etching, the tip is mounted in a tip holder, fixed in a tip shuttle and introduced in the UHV system. Under UHV conditions, it is then cleaned by heating at $T \approx$2000 K by means of electron bombardment in the preparation chamber in order to remove oxide. To make the tip magnetically sensitive, it is coated with Fe or Cr material followed by annealing at $T \approx 500$ K for about $t = 5$ min. The annealing results in a smooth thin film at the tip apex.

For determining whether the in-plane or out-of-plane component of surface spins is imaged, it is important to control the spin orientation at the tip apex. It was reported that a film thickness between 25 and 45 ML Cr predominantly leads to an out-of-plane sensitivity, whereas thicker films of Cr are sensitive to the in-plane component [47]; Fe films exhibit a strong in-plane anisotropy [48]. The spin direction of Fe-coated W tips can be changed in external magnetic fields applied normal to the sample surface, that force the tip magnetization out of the easy (in-plane) into the hard (out-of-plane) direction (see Fig. 4.5) [48; 47]. This makes Fe-coated W tips useful to investigate magnetic samples with a large anisotropy, which remain unaffected by the magnetic field. Another advantage of tips covered with Fe films is that their spin polarization is larger than the spin polarization of Cr-coated tips: the measured spin polarization of tunneling electrons from Fe-coated tips amounts to 40-45 %, whereas only half of that value is typically measured for Cr-coated tips [47]. However, the magnetic stray field from a Fe film can lead to modifications of the sample's magnetization, especially for magnetically soft materials such as Ni. In contrast, the stray field of Cr-coated tips is found to be negligible due to the antiferromagnetic ordering [49; 47].

In my thesis, bare and graphene-covered Ni(111) were investigated by using W tips coated with about 50 ML of Cr, to minimize the magnetostatic interaction between the probe and the sample. It will be, however, shown in Chap. 5 that the tip can exhibit a non-negligible stray field due to picking up magnetic material from the surface, resulting in measurement artifacts. In-

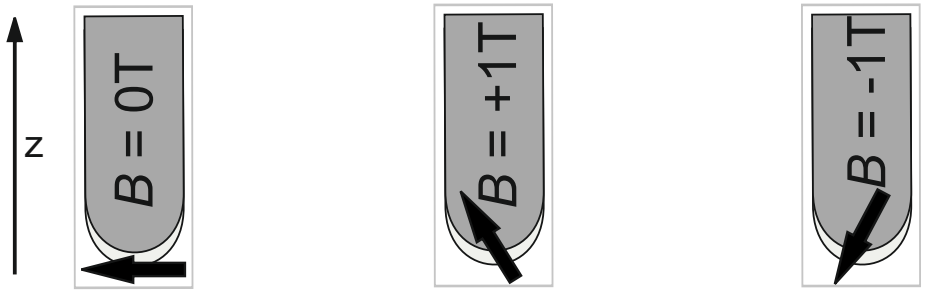

Figure 4.5: Schematic illustration of Fe-coated W tips used to study Pd adlayers on Co/Ir(111) and single Co atoms adsorbed on top. The tip magnetization direction is in-plane at $B = 0$ T, while it possesses a significant out-of-plane component at magnetic fields of $B = \pm 1$ T applied normal to a sample surface (along z-direction).

dividual magnetic atoms deposited on graphene/Ni(111) were explored with bare W tips only. Pd adlayers on Co/Ir(111) and single Co atoms adsorbed on top were studied with W tips coated with ≈ 45 ML of Fe, to achieve larger spin contrast and align the tip's magnetization in an external magnetic field, such that it possesses a significant out-of-plane component. It will be shown in Chap. 6 that magnetic fields of $1\text{T} \leq |B| \leq 2\text{T}$ does not affect Pd-covered Co/Ir(111), therefore I made use of the possibility to align the tip magnetization in a magnetic field of this size throughout that study (see Fig. 4.5).

Chapter 5

Ni(111) and graphene/Ni(111)

This chapter presents an investigation of Ni(111) and graphene on Ni(111) with three different magnetic imaging techniques, covering length scales from the nanometer regime up to several millimeters. With STM the atomic lattice is resolved and bare Ni(111) is characterized by STS. SP-STM can access single domain walls and their response to an applied magnetic field. To investigate the entire surface domain structure, however, techniques with a larger field of view are necessary. *Scanning electron microscopy with polarization analysis* (spin-SEM or SEMPA) [50] is used for vectorial mapping of the surface magnetization and *Kerr microscopy* is applied for field dependent imaging [51]. Interestingly, SP-STM and SEMPA can access the Ni magnetism through the graphene layer, which is unchanged compared to bare Ni(111). For a deeper understanding of the two surfaces spin-resolved *density functional theory* (DFT) calculations are performed. Evaluating the calculated LDOS in the vacuum above the surfaces allows the interpretation of the STM and STS data. After having investigated graphene/Ni(111), individual magnetic atoms such as Fe, Co and Cr are deposited on top and studied by means of STM.

5.1 Ni(111) properties

Bulk Ni has a fcc crystallographic structure with three magnetization axes along [111], [110] and [100]- directions. The corresponding magneto-crystalline anisotropy constants are $K_1 = -12.63 \cdot 10^4\ J/m^3$, $K_2 = 5.78 \cdot 10^4\ J/m^3$ and $K_3 = 3.48 \cdot 10^3\ J/m^3$, respectively. Due to the relationship $E_1 < E_2 < E_3$, where E_i is the energy related to the magneto-crystalline anisotropy, [111], [110] and [100]-directions are the easy, medium and hard magnetization axes, respectively (see Fig. 5.1(a)). The ratio of K_1/K_2 is, however, about 2, which means that both constants are of the same order of magnitude. In this case,

the temperature dependence of the anisotropy constants has to be taken into account (Fig. 5.1(b)). For example, K_1 is negative for temperatures below about 400 K and changes sign above this value. Thus, the magnetic properties are different in both temperature regimes [21].

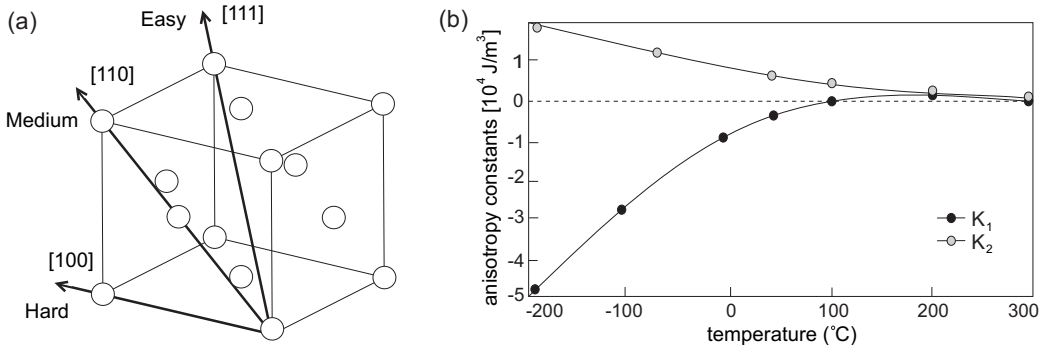

Figure 5.1: Fcc-Ni: (a) Schematic drawing of a crystallographic structure with magnetization axes. (b) Temperature dependence of the magneto-crystalline anisotropy constants K_1 and K_1 (Source: [21]).

Ferromagnetic Ni possesses uniformly magnetized regions which exhibit a parallel orientation of all magnetic moments within so-called magnetic *domains* but different directions of the magnetization in different domains. The boundary between neighbored domains is a *domain wall*. Due to energy minimization, the formation of domains is a balance between the cost of *dipolar energy* (in literature, it is also called demagnetization energy or magnetostatic energy) and the energetic cost of a domain wall. A classification of domain walls is given by the angle of the magnetization between two neighbored domains with the wall as boundary. The occurrence of different types of domain walls depends on the crystallographic arrangement of the ferromagnet. Since fcc-Ni has four axes along [111]-like directions, the domain walls exhibit angles of 180°, 109° and 71°. 180° domain walls can be divided into two classes: *Bloch walls* with the rotation of the magnetization in a plane parallel to the domain wall, and *Néel walls* with the rotation of the magnetization perpendicular to the domain wall.* The Bloch wall is favoured in the bulk because it leads to a smaller dipolar energy. The Néel wall tends to be favoured in thin films since there is a dipolar energy cost to rotate the spins out of the plane of the film.

Due to the reduction of the symmetry, the domain pattern becomes different at the surface compared to the bulk. The difference is a formation of additional domains called *closure domains*. Closure domains lead to a *branching* of domains nearby the surface. The branching process depends on a crystal symmetry, in particular on the number of available easy directions. Since there are no easy magnetization axes in the plane, a complex magnetic pattern is expected for Ni(111) [21]. A model of multiple *quasi-domain branching* was

*A good introduction into a domain wall formation can be found in [21; 51]

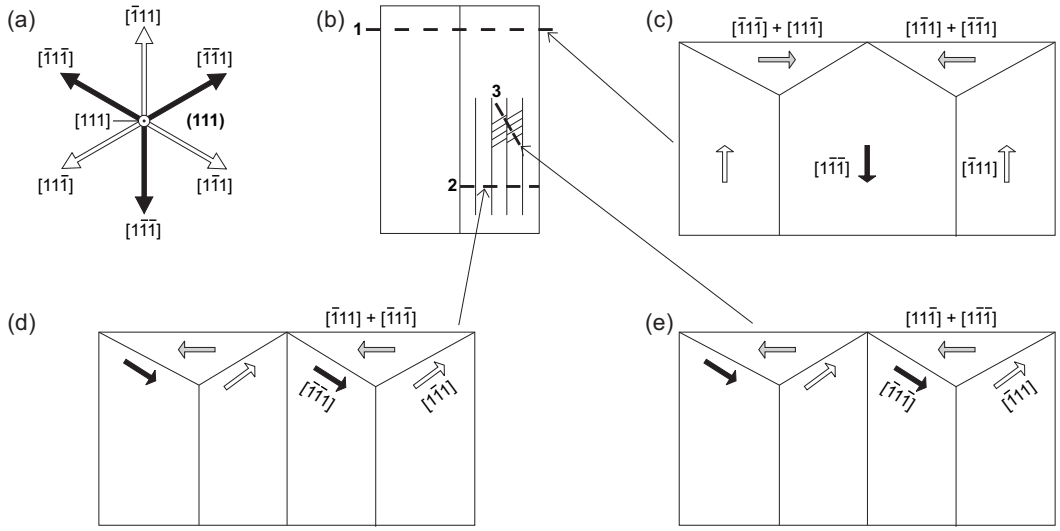

Figure 5.2: An example of allowed sequence of quasi-domain branching for Ni(111) (Source: [51]).

therefore proposed by Hubert and Schäfer [51]. In this model, the branching phenomenon can be explained by the progressive domain refinement towards the surface by integrated generations of domains. Figs. 5.2(a,b) shows different {111}-easy directions seen from the top of the (111)-plane, and different domain generations. Hubert and Schäfer suggested to start with the cross-section as shown in Fig. 5.2(c), which indicates the basic domains consisting of 180° domains and the closure domains in the first generation. The closure domains are chosen from combinations of the easy directions which results in surface-parallel net magnetization directions - the quasi-domains. In the next branching generation shown in Fig. 5.2(d), the components of a quasi-closure domain are used from Fig. 5.2(c) as the new basic domains; consequently, the components of the third generation in Fig. 5.2(e) are combined from those of the surface-net magnetization of Fig. 5.2(d). The subdivision process ends when the additional domain wall energy exceeds the dipolar energy in the closure domains.

For a long time, only bitter technique data has been available, which gives only a rough idea of the surface domain structure of Ni(111) [52]. More recent Magnetic Force Microscopy (MFM) studies showed that domains of the order of 500 nm can be observed at $T = 8$ K and domain walls shifted in perpendicular fields of $B = +25$ mT [53]. However, a complete picture of the microscopic domain pattern was still missing. A close inspection of the magnetic structure of Ni(111) in different temperature regimes and covering length scales from the nanometer regime up to several millimeters has been studied in my PhD thesis, where results are shown in Sections 5.4, 5.6 and 5.7.

The band structure of Ni(111) exhibits the free-electron-like surface state called *Shockley surface state*. The nature of the state was long studied and

discussed [54; 55; 56; 57; 58]. Recently, the spin-splitting of the Shockley surface state has been found to play an important role for the magnetic properties of the surface. In my PhD work, by observing of the standing waves caused by the step edges, the spatial resolution of the electronic state is examined in Section 5.4, and a detailed theoretical investigation of the band structure of Ni(111) is shown in Section 5.5.

5.2 Graphene properties

Graphene is a single atomic layer of carbon which is tightly packed into a two-dimensional (2D) honeycomb lattice (Fig. 5.3(a)). Alternatively, it can be viewed as an individual atomic plane pulled out of bulk graphite. Theoretically, graphene (or "2D graphite") has been studied for sixty years and widely used to describe properties of carbon-based materials [59; 60; 61]. Forty years later, it was realized that graphene also provides an excellent condensed-matter model of 2D quantum electrodynamics [62; 63; 64]. However, graphene was presumed not to exist in the free state, since it is thermodynamically unstable, thus graphene was described as an "academic" material [63] and believed to form only curved structures such as fullerenes and nanotubes. A breakthrough was made few years ago when *free-standing* graphene was unexpectedly found by A. K. Geim and K. S. Novoselov [65; 66; 67]. They showed that carbon in such a flat form has exceptional properties revealing a lot of new physics and potential applications, and were awarded with the Nobel Prize in Physics in 2010.

From the point of view of its electronic properties, graphene is a zero-gap semiconductor where electrons propagating through the honeycomb lattice behave as massless, which results in quasi-particles that are described by a Dirac-like equation rather than the Schrödinger equation. The Dirac equation is a direct consequence of a graphene's crystal symmetry: its lattice is made up of two equivalent carbon sub-lattices A and B, and energy bands associated with sub-lattices intersect at zero energy at K points of the Brillouin zone, giving rise to a *linear spectrum* shown in Fig. 5.3(a). The linear gapless spectrum means that graphene exhibits ballistic electronic transport on the micrometer scale at room temperature (RT) [65]. This manifests itself in a variety of spectacular transport phenomena such as a minimum conductivity, anomalous quantum Hall effect (QHE) [67; 68], bipolar supercurrent [69] and room-temperature QHE [70].

The transport experiments were performed on graphene sheets obtained by mechanical exfoliation of graphite and placed on an amorphous SiO_2 substrate. In this case, the interaction between graphene and substrate is mainly through weak van der Waals forces, which do not induce any structural changes in the graphene crystal. However, if graphene is obtained by thermal treatment, for example, of a SiC wafer, or via a chemical vapour deposition (CVD) [71] of hydrocarbon molecules on a metallic substrate, a stronger interaction is

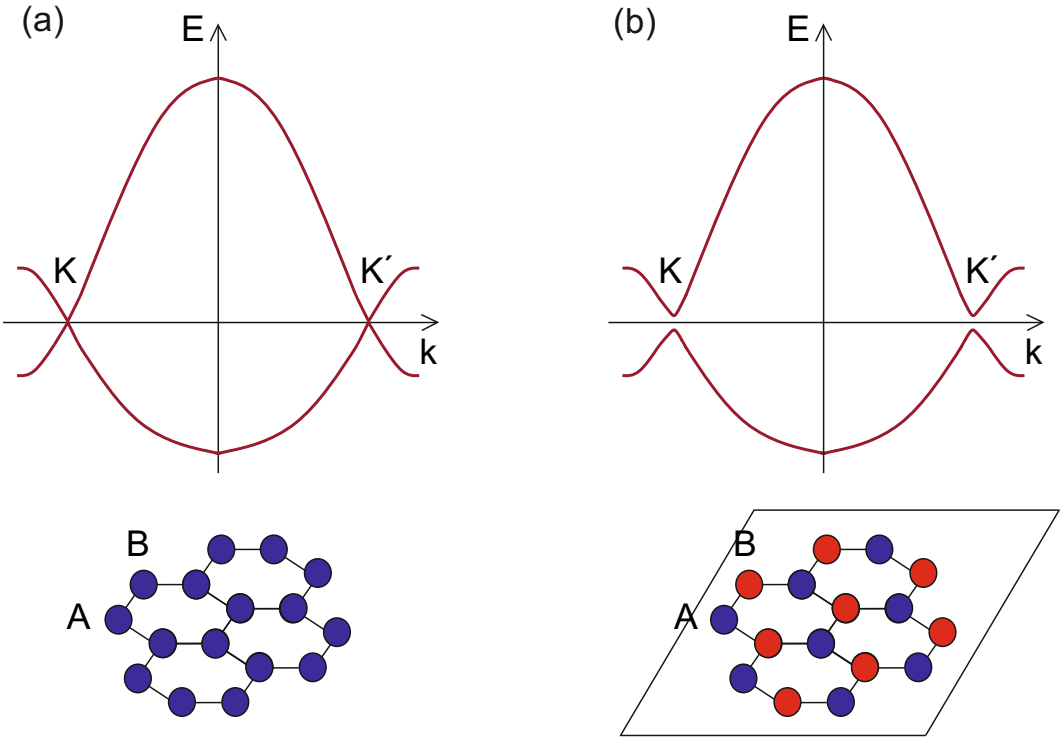

Figure 5.3: Schematic representation of crystal and electronic band structure of (a) free-standing graphene and (b) epitaxial graphene.

expected [72]. In this case, graphene is known as *epitaxial*, and it can be commensurate with an underlaying crystal structure. The interaction of graphene with the substrate can, in principle, open a gap around the K points: since only every second carbon atom has a neighbour in the bottom layer, the graphene's lattice symmetry is broken (see Fig. 5.3(b)). For example, due to the strong hybridization between carbon p_z and transition metal $3d$ band states, a gap $\leq 0.3\ eV$ was predicted theoretically [73] and observed experimentally [74] in graphene/Ni(111). Since most electronic applications rely on the presence of a gap between the valence and conduction bands, the opening of the mini-gap in epitaxial graphene makes it technologically promising.

In my PhD work, I used a Ni(111) crystal due to its role of a perfect substrate for the growth of graphene [17]. Owing to the very small lattice mismatch, graphene grows pseudomorphically, and, due to the hybridization with the Ni atoms, graphene-covered Ni can be an efficient source of spin-polarized electrons [74; 75]. In addition, it was also reported that graphene passivates Ni(111) against oxygen exposure [75], which makes the graphene/Ni(111) system a promising candidate for applications in carbon-based magnetic media and spintronic devices.

5.3 Sample preparation

The same Ni(111) single crystal (3 mm × 7 mm width, 1 mm thickness) was used in SP-STM, SEMPA and Kerr experiments. It was cleaned by repeated cycles of 800 eV Ar^+ ion etching at RT and annealing at $T = 1100$ K. The sample was considered clean when no impurities such as carbon or sulfur were detected by AES and a hexagonal (1×1) pattern was observed by LEED. The graphene layer was grown on Ni(111) by CVD consisting of the following steps [76; 77]:
(i) When Ni(111) was heated to $T = 950$ K in an ethylene (C_2H_4) atmosphere of $p = 5 \times 10^{-7}$ mbar for 200 s (100 L), carbon atoms were generated at the Ni surface and diffused into the metal (see Figs. 5.4(a,b)).
(ii) As Ni(111) was subsequently cooled down in ultra-high vacuum (UHV), the carbon atoms segregated out of the Ni layers and formed graphene on the surface (Fig. 5.4(c)). The sample quality was verified by STM measurements.

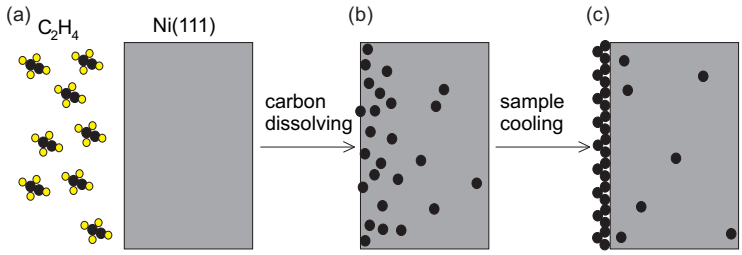

Figure 5.4: Illustration of a graphene preparation on Ni(111) via CVD.

5.4 STM results

5.4.1 Ni(111)

Figure 5.5(a) shows a typical surface area of bare Ni(111) including two monatomic steps. The observed terrace widths vary from 20 - 200 nm. As seen in Fig. 5.5(b), the atomic lattice can be resolved on the terraces. Fig. 5.5(c) displays a line profile along a closed packed row (white line in (b)) and the interatomic spacing is in agreement with the nearest-neighbor atomic distance of Ni (2.49 Å). As expected for closed packed surfaces like fcc(111), the corrugation is comparatively small and lies in the range of 3 - 5 pm [78].

Despite the nice ordering of surface Ni atoms, residual contamination is present in the sample, in particular sub-surface defects. These defects have very low corrugation in constant current images, but are clearly seen in $\mathrm{d}I/\mathrm{d}U$ maps, e.g. at $U = +1$ V (see the inset in Fig. 5.5(d)). Therefore, care was taken to measure $\mathrm{d}I/\mathrm{d}U$ spectra on defect free areas: Fig. 5.5(d) shows an average of three spectra measured at positions as indicated in the inset. Two

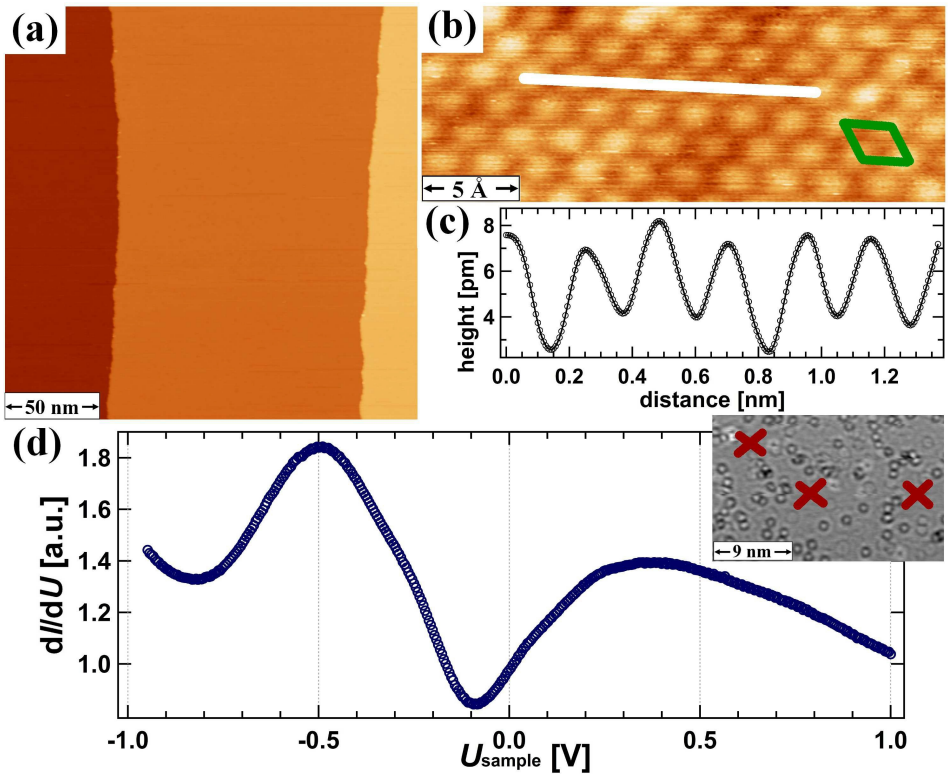

Figure 5.5: Ni(111), spin-averaged data: (a) Constant-current image ($U = -1$ V, $I = 0.5$ nA) taken at $T = 8$ K. (b) Atomically resolved image ($U = -4$ mV, $I = 5$ nA) taken at RT. The diamond highlights the unit cell. (c) Height profile along the line displayed in (b). (d) The dI/dU spectrum ($U_{\mathrm{stab}} = +1$ V, $I_{\mathrm{stab}} = 2$ nA, $U_{\mathrm{mod}} = 80$ mV) is averaged over data taken at three different locations marked as red crosses in the dI/dU map (inset).

broad maxima can be observed: 500 meV below and about 400 meV above E_{F}, respectively. The spectrum agrees well with the experimental results in [56; 57]. First-principle calculations shown in Section 5.5 attribute these features to a minority spin surface resonance below E_{F} and the Shockley state of both spin characters above E_{F}.

To explore the Ni(111) electronic structure spatially resolved, I performed measurements on standing-waves patterns associated with surface states. Figures 5.6(a-e) display dI/dU maps where standing waves caused by the step edges can be clearly observed. To get more detailed information about the standing waves, fast Fourier transformation (FFT) was applied to the dI/dU maps. As a result, FFT reciprocal images show circular-shaped patterns where bright regions indicate more intense Fourier components (Figs. 5.6(f-j)). The circles become smaller as U decreases. The extracted radii from FFT images are therefore plotted as a function of energy, as it is shown in Fig. 5.6(k). The obtained result determines the electronic dispersion of the surface state of Ni(111), which is in good qualitative agreement with previous experimental

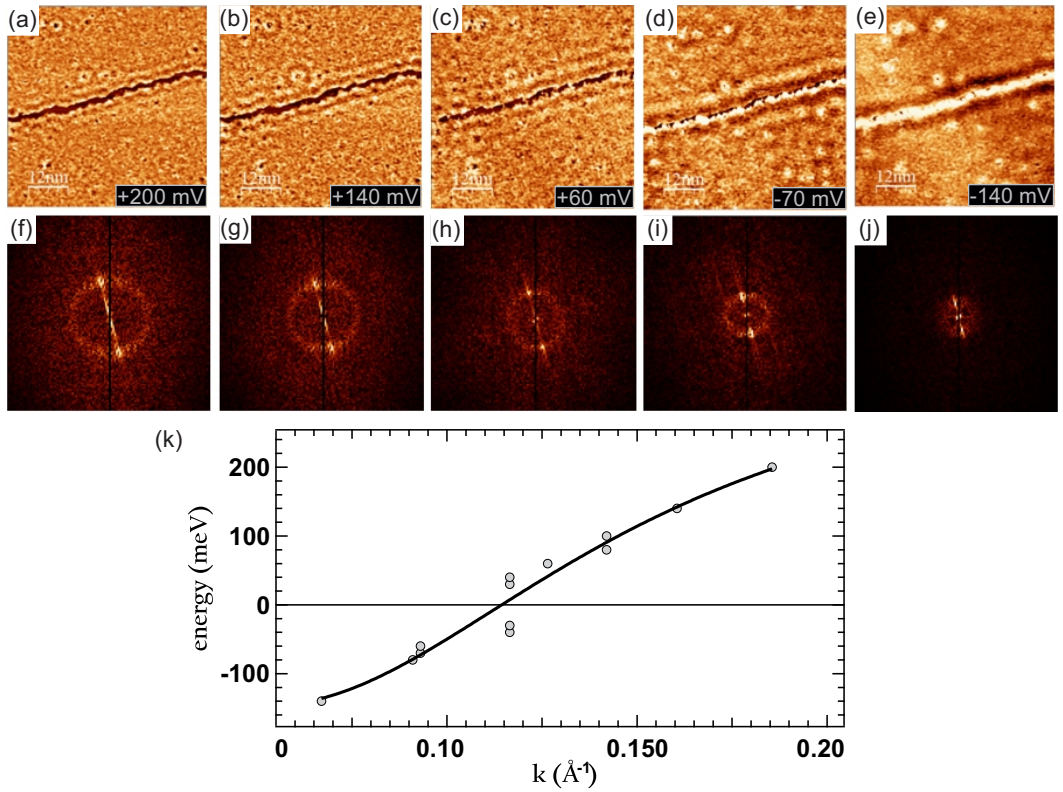

Figure 5.6: (a-e) dI/dU maps showing standing waves at a step edge of Ni(111). (f-j) Circular patters obtained by the fast Fourier transformation of dI/dU images, respectively. All data were measured at $T = 8$ K and $I = 2.5$ nA. (k) Electronic dispersion of the Ni(111) surface state.

studies in [57; 79], and arises from an upward dispersing band of the minority-spin component with an energy minimum of $E = -140$ meV at the Γ point, as found in our DFT calculations (see Section 5.5).

To investigate the magnetic properties of the Ni(111) surface I used SP-STM with W tips which were coated with about 50 ML of Cr and exhibiting an in-plane spin sensitivity: Fig. 5.7(a) shows a dI/dU map of a sample area exhibiting nearly horizontal steps. The darker and brighter regions indicate magnetic domains of Ni(111) and the dashed lines indicate domain walls. To prove the magnetic origin of the observed contrast I apply an out-of-plane magnetic field of $B = +50$ mT and as a result both domain walls have moved to the left as seen in Fig. 5.7(b), the right one by about 150 nm. Line sections across the walls, as indicated by a white box in Fig. 5.7(a) are shown in Fig. 5.7(c). Fitting a standard wall profile[†] (solid line),

$$\tanh((x)/(w/2)), \tag{5.1}$$

where x is a lateral distance, to the experimental data (dots) yields wall widths

[†]I used a fit for a 180° Bloch wall for the only purpose of estimating the domain wall width.

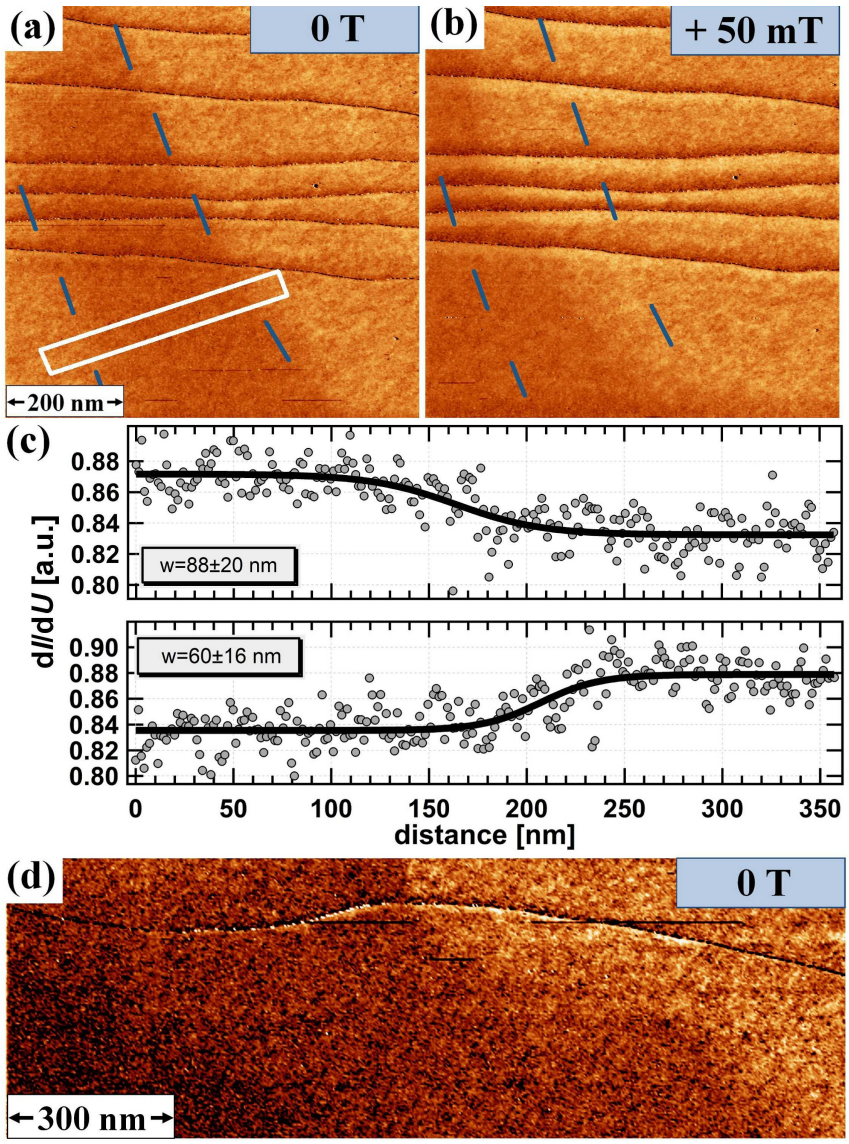

Figure 5.7: Ni(111), spin-polarized data: Magnetic dI/dU maps taken at (a) B = 0 T and (b) B = +50 mT. Dashed lines show the shift of domain walls in the external magnetic field. (c) Line sections across domain walls marked by the white box in (a). Gray circles and black lines represent experimental data and fitted profiles, respectively. (d) Magnetic dI/dU map of 1.5 μm width taken at B = 0 T. All data measured at U = −200 mV and I = 2.5 nA.

of w = 88±20 nm and w = 60±16 nm, respectively. The wall width determined for the wall in (b) at +50 mT is $w = 62 \pm 17$ nm. This shows that while one can move domain walls in the out-of-plane field of +50 mT the width of the wall in Fig. 5.7 is not altered within the error of the measured width. The reason why these walls can be moved by the out-of-plane field becomes clear from the volume domain structure as deduced from SEMPA measurements (Section 5.7). The magnetic contrast, which can be defined as the asymmetry

of the $\mathrm{d}I/\mathrm{d}U$ signals of bright (b) and dark (d) areas [47],

$$A(U) = \frac{\mathrm{d}I/\mathrm{d}U(U)_\mathrm{b} - \mathrm{d}I/\mathrm{d}U(U)_\mathrm{d}}{\mathrm{d}I/\mathrm{d}U(U)_\mathrm{b} + \mathrm{d}I/\mathrm{d}U(U)_\mathrm{d}}, \tag{5.2}$$

is only of $A(-200\ \mathrm{mV}) = 2\ \%$, evaluated for the data in Figs. 5.7(a,b). Such a low value of $A(-200\ \mathrm{mV})$ was also obtained for different samples measured with different Cr-coated W tips.

The observed domains in Ni(111) are larger than the image size of Figs. 5.7(a,b). To get a better view of the magnetic structure, I performed SP-STM measurements on a larger area of the surface. The spin-resolved $\mathrm{d}I/\mathrm{d}U$ map in Fig. 5.7(d) has a width of 1.5 μm and shows three regions of different intensity, i.e. magnetic domains, and an atomic step. The asymmetry between the highest and lowest signal is the same as determined for Figs. 5.7(a,b). The occurrence of several domains with different magnetization directions on this length scale indicates already an interesting overall magnetic structure. However, the observation of the whole pattern is difficult to achieve with SP-STM, thereby an imaging technique with a larger field of view is required (see Sections 5.6 and 5.7).

5.4.2 Graphene/Ni(111)

The graphene layer is commensurate with Ni(111) due to the small lattice mismatch [73]. A typical sample of graphene on Ni is shown in Fig. 5.8(a). The flat terraces indicate perfect single domain graphene formation without any visible defects. At higher magnification in Fig. 5.8(b) a triangular lattice is seen rather than the honeycomb structure of the carbon atoms (the unit cell is highlighted by the diamond as shown in the inset). This is not surprising since neighboring carbon atoms occupy non-equivalent sites on the Ni substrate: in the ball model in Fig. 5.8(d) the carbon atoms labeled A reside on top of the Ni atoms of the first layer, while the carbon atoms labeled B are at positions of the Ni atoms of the third layer (fcc hollow site) [73; 80; 81].

The white line in Fig. 5.8(b) indicates the position of the line profile in Fig. 5.8(c) and the distance between maxima is the same as for the bare Ni(111) surface shown in Fig. 5.5(b,c), reflecting the nearest-neighbor distance of Ni (2.49 Å). However, in contrast to Figs. 5.5(b,c), fcc and hcp hollow sites are now distinguishable, due to the B type atoms on fcc positions. In addition, the atomic corrugation of 10 - 15 pm for graphene on Ni(111) observed here is roughly a factor of 3 larger than that measured on bare Ni(111). Both a triangular lattice structure and an enhanced corrugation seen in STM images are a purely electronic effect originating from graphene p_z states around E_F and the quenching of Ni surface states as will be discussed in Section 5.5.

To investigate whether it is still possible to measure a magnetic signal on graphene-coated Ni(111) SP-STM measurements were performed using W tips coated with about 50 ML of Cr and exhibiting an in-plane spin sensitivity. Figures 5.9(a,b) show $\mathrm{d}I/\mathrm{d}U$ maps measured in (a) forward and (b) backward

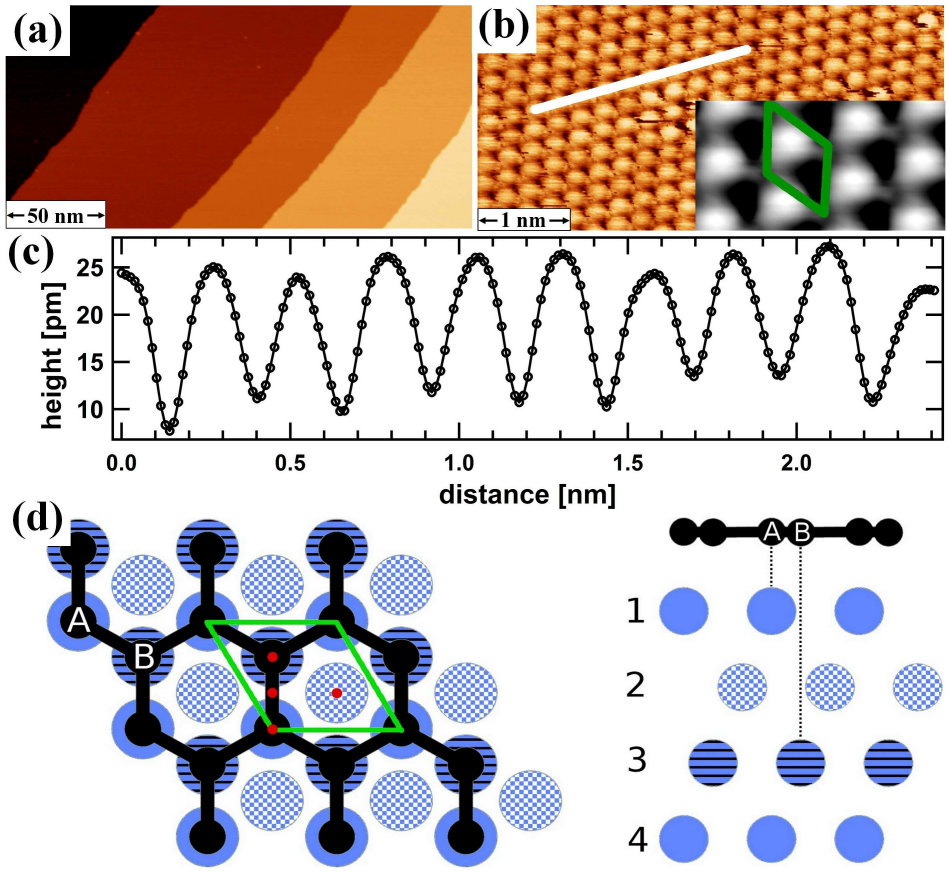

Figure 5.8: Graphene on Ni(111), spin-averaged data: (a) Constant current overview image ($U = -1$ V, $I = 0.5$ nA), taken at $T = 8 \pm 1$ K, showing flat terraces and four monatomic steps. (b) Zoom-in on a terrace ($U = +2.5$ mV, $I = 5$ nA) showing the atomic lattice. (c) Height profile along the line depicted in (b). (d) Top and side views of the graphene/Ni top-fcc structure: Black color indicates carbon, blue color Ni atoms. Red dots indicate the positions of the empty spheres (see Section 5.5). The unit cell is highlighted by the diamond.

scan direction with the same bias voltage $U = -200$ mV as in Fig. 5.7(a,b). Again, areas of different $\mathrm{d}I/\mathrm{d}U$ contrast as a result of different magnetic domains in the image area can be seen. This means that the electron density a few Ångström above the surface (at the position of the tip) is substantially spin-polarized, despite the fact that the carbon atoms are expected to carry a very small magnetic moment [82; 73; 83]. Thus, the magnetic structure of Ni(111) under the graphene layer is probed. Evaluating the magnetic signal strength for the $\mathrm{d}I/\mathrm{d}U$ maps in Fig. 5.9(a,b), one can find a magnetic asymmetry of $A(-200\mathrm{mV}) = 4$ %. Two types of boundaries between homogeneously magnetized areas are observed: while the left one can clearly be identified as a domain wall with a width of $w = 51 \pm 6$ nm (see line profile and

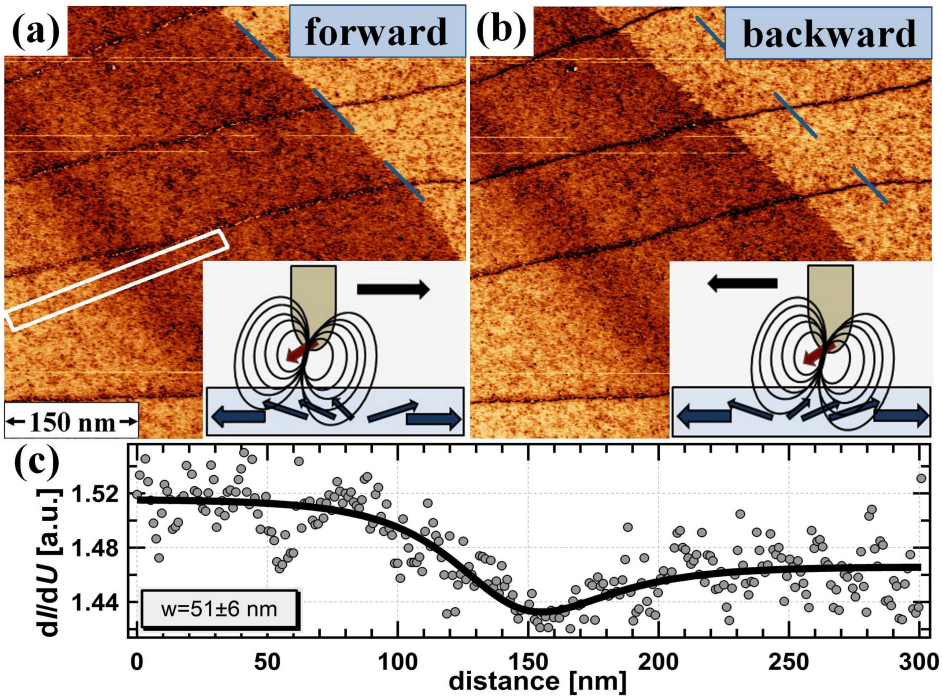

Figure 5.9: Graphene on Ni(111), spin-polarized data: Magnetic dI/dU maps measured in (a) forward and (b) backward scan directions ($U = -200$ mV, $I = 0.5$ nA). While the left wall is static, the right one is moved by the stray field of the tip (see text). (c) Line section as indicated in (a) and a fit of a general wall profile, yielding a wall width of about 50 nm. Data taken at $B = 0$ T.

fit in Fig. 5.9(c)[‡]), the right one displays a non-continuous transition which appears at different lateral positions in forward and backward scan direction. This sharp transition is therefore not a domain wall, but instead it is an artifact resulting from magnetostatic interaction with the tip (see sketches in Fig. 5.9(a,b)). Its lateral position depends on the scan direction (i.e. from left to right or vice versa) since the domain wall is pushed along the scan direction by the tip until it snaps back. This means that the tip used in this experiment exhibits a non-negligible stray field, most likely due to picking up magnetic material from the sample. Such an influence is frequently observed when using ferromagnetic tips to investigate soft magnetic materials both in SP-STM and MFM [47]. Reasons for the two walls in the image area responding non-equivalently might be different magnetization directions or different wall types. The fact that the magnetic structure of Ni(111) can easily be changed by small external magnetic fields (cf. Fig. 5.7(b)) suggests that already small amounts of ferromagnetic material at the tip apex are sufficient to observe interactions

[‡]In general, a domain wall profile measured by SP-STM strongly depends on the tip magnetization direction [84]. I used a fit: cos(arcsin(tanh((x)/(w/2))+θ), where θ is the angle between the tip and the domain wall magnetizations. If $\theta = 0$, the fit can be simplified into Eq. (5.1), thus, describes standard wall profiles shown in Fig. 5.7(c).

with the domain structure.

5.5 Theory results

To gain a detailed understanding of the observations made in the STM experiments, M. Karolak, B. Sachs and T. O. Wehling from Prof. A. I. Lichtenstein's group of the I. Institute of Applied Physics of Hamburg University performed DFT calculations of the pure Ni(111) and the graphene/Ni(111) system using the projector augmented wave [85] based Vienna-ab-initio-Simulation-Package (VASP) [86; 87]. The generalized gradient approximation (GGA) [88] to the exchange correlation potential was employed and van der Waals interactions in the calculations involving graphene in the framework of the DFT-D2 method [89] were accounted for. The electronic properties of a clean Ni(111) slab and a Ni(111) slab coated with graphene on one side, both containing 15 atomic layers of Ni and ~ 18 Å of vacuum between periodic images of the slabs, were calculated.

The triangular unit cell of the fcc Ni(111) surface and the triangular graphene unit cell exhibit a lattice mismatch of 1.8 %. In the calculations, a unit cell with the experimental lattice constant of the Ni(111) surface $a = 2.49$ Å [90] was used and the graphene layer deposited in the so-called *top-fcc* arrangement (Fig. 5.8(d)) was established as the energetically most favorable one in experimental and theoretical investigations [80; 81]. All geometries considered in the calculations were optimized until all forces were below 0.01 eV Å^{-1}. For obtaining the LDOS, the Brillouin zone integrations were performed with the tetrahedron method [91] using 36×36 **k**-point meshes.

M. Karolak *et al.* simulated high-resolution STM images by calculating the position dependent LDOS in the vacuum and integrating the energy window from -100 meV to 100 meV. To simulate STM spectra, the LDOS inside so-called empty spheres placed at 3.6 Å above the surfaces in the vacuum region of the slab was calculated. The LDOS inside the empty spheres was calculated assuming an STM tip with an *s*-wave symmetric apex state. The LDOS at lower/higher distances (between 2 Å and 7 Å) from the slab was carefully checked to show a smooth trend and yield qualitatively the same values. Spheres at four different lateral positions above the surfaces (see red dots in Fig. 5.8(d)) were considered to investigate lateral modulations in the STM spectra.

In STM experiments, there is an electric field between a tip and a sample, which modifies the shape of the tunneling barrier [92]. The exact shape of the tunneling barrier is unknown but can be approximated by a trapezoidal barrier in the most simple model. Besides any density of states effects, this leads to an energy and tip-height dependence of the $\mathrm{d}I/\mathrm{d}U$-signal according

to [93]

$$\frac{\mathrm{d}I}{\mathrm{d}U} \sim \exp\left(-\int_0^s \mathrm{d}z \left[\frac{8m}{\hbar^2}\left(\Phi + eU\frac{z}{s} - eU\right)\right]^{-\frac{1}{2}}\right), \tag{5.3}$$

where Φ is the work function of the tip and the sample and s is the distance between the tip and the sample. Expanding the exponent to first order in U one can arrive at

$$\frac{\mathrm{d}I}{\mathrm{d}U} \sim c_0 \exp\left(-\frac{eU}{E_0}\right), \tag{5.4}$$

where E_0 is a constant depending on the materials of the tip and the sample as well as on their distance.

To simulate STM spectra, the vacuum LDOS from the DFT calculations (which accounts for the tunneling barrier due to the sample work function) is therefore used and scaled by a factor of $\exp(-E/E_0)$ to account for electric field induced dependencies of the effective tunneling barrier height on the bias voltage. E_0 is treated as a fitting parameter. In Section 5.5 $E_0 = 2$ eV is used, which leads to good agreement of our first-principles calculations with the experimental data.

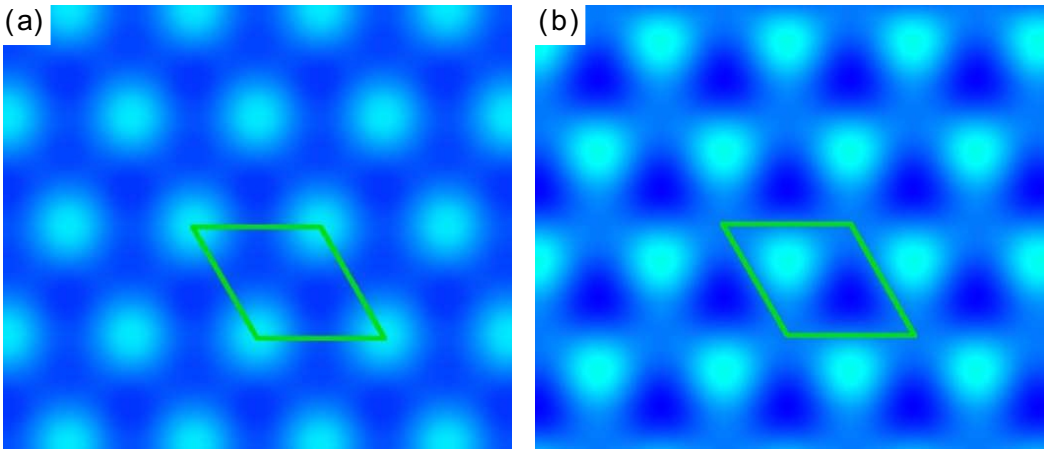

Figure 5.10: Simulated STM images calculated at a height of 3.6 Å over (a) clean Ni(111) and (b) graphene/Ni(111). The orientation of the graphene lattice is the same as in the unit cell depicted in Fig. 5.8(d): the C atoms visible in the image belong to the B sublattice.

I would like to start with the simulated STM images (Fig. 5.10) and compare them to the experiments (Figs. 5.5(b) and 5.8(b)). Over the clean Ni(111) surface, M. Karolak *et al.* find a triangular lattice of protrusions visible as bright spots (Fig. 5.10(a)), which is in good agreement with the experimental STM image (Fig. 5.5(b)). The calculations show that the protrusions are centered above the atoms of the topmost Ni layer.

The calculations, as well as results in [80; 90], yield graphene adsorbing at a distance of ~ 2.10 Å above the Ni surface with the graphene layer being almost flat, the height difference between the carbon sublattices (the structural corrugation) is about 0.5 pm. However, due to an electronic effect, the simulated STM images of graphene/Ni(111) also show a triangular lattice structure (Fig. 5.10(b)) again in good agreement with the experiment (Fig. 5.8(b)). In the convention of Fig. 5.8(d), the calculations yield the highest vacuum LDOS above carbon atoms of the B sublattice, i.e. those carbon atoms not located above a Ni atom from the topmost Ni(111) layer. This feature is stable with the simulated tip height and bias voltage. Thus, the highest protrusions in the STM images of graphene on Ni(111) correspond to carbon atoms in sublattice B.

In the STM experiments of graphene on Ni(111), the graphene sublattices A and B exhibit an apparent height difference on the order of 10 pm. Since the structural corrugation is only about 0.5 pm, this enhanced corrugation in the experiments must have an electronic but *not* a structural origin. The electronic states responsible for this corrugation will be discussed together with the calculated STM spectra below.

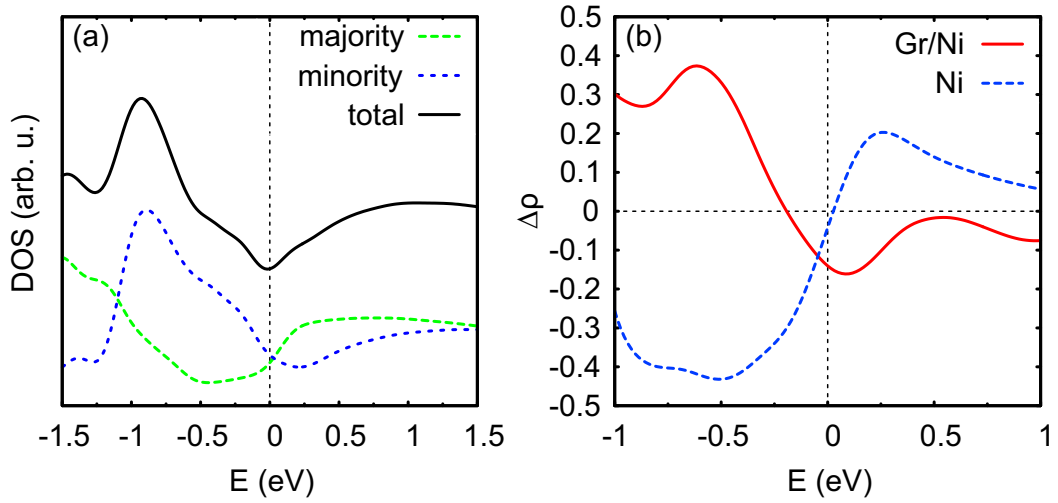

Figure 5.11: (a) Simulated STS spectrum at 3.6 Å above the clean Ni(111) surface. (b) Spin contrast $\Delta\rho$ (see text) at 3.6 Å over the pristine Ni(111) surface and the graphene-coated Ni(111) surface, respectively.

In the experiment energy resolved STM spectra and spin-resolved differential conductance ($\mathrm{d}I/\mathrm{d}U$) maps were obtained, which now can be compared to spectra from our DFT calculations. The calculated STS spectrum for the pristine Ni(111) surface is shown in Fig. 5.11(a). It exhibits broad maxima in the energy range between -1 eV and -0.5 eV as well as above E_F at energies $\gtrsim 0.5$ eV. The Ni spectrum is found to be unchanged with the lateral position of the tip. A comparison to Fig. 5.5(d) shows that the calculated spectrum is in qualitative agreement with the experimental results.

The calculations show that the contribution to the STS signal arising from majority (spin-up) and minority spin states (spin-down) differs clearly, which is well in line with spin contrast being achievable in our SP-STM experiments. To simulate the magnetic contrast provided by SP-STM the spin contrast $\Delta\rho = (\rho_\uparrow - \rho_\downarrow)/(\rho_\uparrow + \rho_\downarrow)$ from the spin polarized density of states, $\rho_{\uparrow\downarrow}$, was calculated. The spin contrast, averaged over the four different spheres in the vacuum (Fig. 5.8(d)), for the clean Ni(111) surface and the graphene-coated surface is shown in Fig. 5.11(b). In agreement with the experiment a pronounced spin contrast over clean Ni as well as over the graphene-coated surface is found. Thus, the spin polarization in the vacuum above the surface is not suppressed by the graphene coating and the ferromagnetic domain structure remains visible in SP-STM. Interestingly, the sign of the spin polarization in the vacuum LDOS is reversed for graphene-coated Ni as opposed to pristine Ni at energies below -0.23 eV as well as above E_F. This spin contrast change may be accessed in future experiments, where one would have to perform an SP-STM measurement on a partially graphene-coated and partially clean Ni(111) sample.

The next aim is to identify which states of the Ni(111) and the graphene/Ni(111) systems give major contributions to the tunnel current in the STM experiments and thus understand the physics behind the calculated and observed STM images, spectra, and spin contrasts. To this end, the band structure was calculated and the corresponding wave functions of the clean and the graphene-coated Ni surface were analyzed. The band structure of a clean Ni slab is shown in Fig. 5.12 for majority (a) and minority (b) spin states. In this figure one can use a so-called "fat band analysis" [94] where the displayed thickness of a band represents the strength of the property of interest. Here the wave function, $|\Psi_{n,k}\rangle$, belonging to a given band n at a given k-point is projected onto an s orbital, $|L\rangle$. Since vacuum LDOS is measured in experiments, the wave function is localized inside an empty sphere at 3.6 Å above the respective surface. The overlap $|\langle\Psi_{n,k}|L\rangle|^2$ is then depicted as the thickness of the corresponding band, which is relevant for our STM measurements.

For clean Ni(111), the dominant contributions to the vacuum LDOS (blue) above E_F arise from upward dispersing bands, which have their energy minima at the Γ point at energies of 10 meV (majority spin electrons) and 140 meV (minority spin electrons). These states can be characterized as surface states or surface resonances. The upward dispersing feature with a minimum at the Γ point for majority spin is the well-known Shockley surface state with mixed Ni p_z and $d_{3z^2-r^2}$ character at Γ and $d_{xz,yz}$ admixtures away from Γ [95; 96]. A similar feature for the minority spin was identified as a resonance of mixed p_z and $d_{xz,yz}$ character [95; 96].

The downward dispersing feature starting at -0.6 eV below E_F for the majority states and dispersing along the $\Gamma \rightarrow$ K and $\Gamma \rightarrow$ M directions in the Brillouin zone was identified as a surface resonance [58]. This specific resonance derives mainly from Ni $d_{xz,yz}$ states with a small admixture of Ni p_z states away from the Γ point. At the Γ point itself, however, it shows no

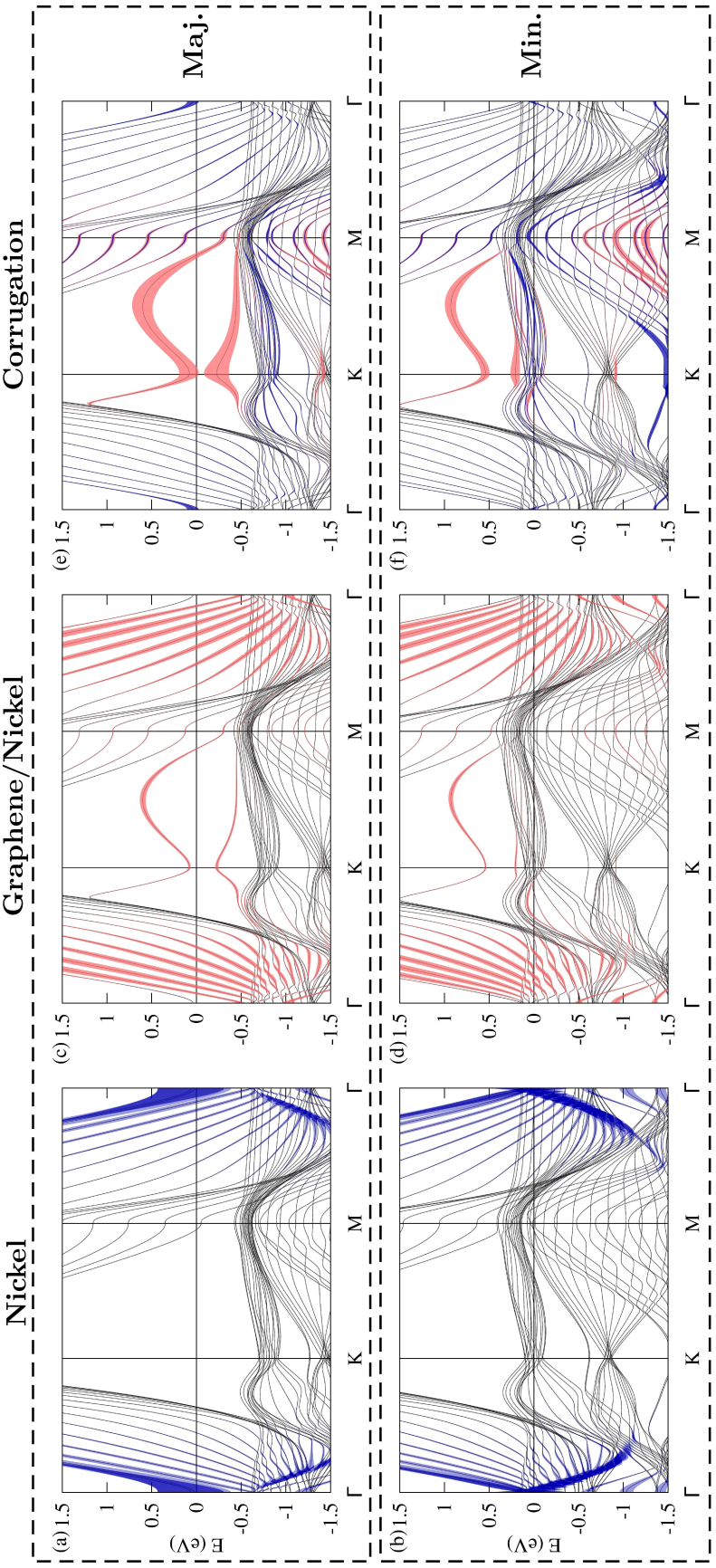

Figure 5.12: Band structure of a clean 15-layer slab of Ni(111) for majority (a) and minority spin (b) components. The same slab, coated with graphene on one side, is shown in (c) for the majority and in (d) for the minority case. The projections of the bands onto empty spheres in the vacuum at 3.6 Å, averaged over their lateral position (red dots in Fig. 5.8(d)), are shown as fat bands. Here, the vacuum projections above the Ni are indicated by blue color, over graphene by red color. In (e) and (f) the contributions of each band to the corrugations measured in STM are visualized as fat bands (see Eq. (5.5)) in the same color code. For visualization purpose, the corrugation above Ni has been enhanced by a factor of 4.

spectral weight in vacuum. For the minority spin component a similar state begins slightly above E_F and disperses down below -1 eV along the $\Gamma \to K$ and $\Gamma \to M$ directions. This feature, showing pronounced weight in the vacuum, was identified as a surface resonance with the same orbital characteristics as the Shockley state described above [96; 58]. This state is responsible for the minority spin polarization dominating in the energy region from ~ -1 eV up to ~ 0.1 eV seen in the spin contrast in Fig. 5.11(b). The STS spectrum shown in Fig. 5.11(a) also becomes clear now: The features of the spin-resolved spectra can be attributed to surface electronic features of Ni. The broad peak below E_F stems mostly from the downward dispersing feature of the minority spin states in Fig. 5.12(b), whereas the unoccupied spectrum is dominated by the Shockley state of both spin character.

Over the graphene-coated surface the situation changes qualitatively. Figures 5.12(c,d) show the fat band analysis for the Ni slab coated on one side with graphene. Over graphene, dominant contributions to the spectral weight in the vacuum (red fat bands) are found arising from free electron like states as can be seen along $\Gamma \to K$ and $\Gamma \to M$ directions. The graphene p_z-derived bands between the K and M points show some smaller weight in the vacuum as well. The pronounced surface states and resonances seen over the Ni surface cannot be seen over graphene, even at very low heights over the surface. The band derived from the Shockley state vanishes explicitly over the graphene-coated slab surface. Only a band from the uncoated surface of the slab remains. Thus, graphene quenches the surface resonances and surface states. Since the surface states are mainly responsible for the sign of the spin contrast in the vacuum over the Ni surface the quenching of these states leads to the predicted reversal of the sign of the contrast (cf. Fig. 5.11(b)).

It is important to note that this reversal of the spin contrast in the vacuum LDOS above graphene does not mean that the Ni magnetization is reversed beneath graphene. In agreement with earlier studies [73], the magnetic moment in the Ni interface layer to graphene is about 20 % smaller (0.51 μ_B) compared to the bulk value of 0.65 μ_B. Additionally, a small spin magnetic moment of -0.02 μ_B for C_A and 0.03 μ_B for C_B atoms respectively is induced in the graphene layer [73; 83].

Finally, I would like to address the question why the apparent height corrugations measured in STM (see Section 5.4) are larger in the graphene/Ni system than on the bare Ni(111) surface. To this end, the vacuum amplitudes of the states of clean Ni(111) and graphene-coated Ni systems at different lateral positions within the unit cell (red dots in Fig. 5.8(d)) are compared. The variation of the state amplitude with the lateral position is visualized in Fig. 5.12(e,f): for each band $|\Psi_{n,k}\rangle$, the thickness d of the colored curves (blue: Ni, red: graphene) corresponds to the standard deviation of the vacuum projections $|\langle\Psi_{n,k}|L_r\rangle|^2$ with lateral sphere position r:

$$d \sim \sqrt{\sum_r \left(|\langle\Psi_{n,k}|L_r\rangle|^2 - \overline{|\langle\Psi_{n,k}|L_r\rangle|^2}\right)^2} / \rho_{\uparrow\downarrow}(E). \tag{5.5}$$

The line thicknesses are normalized to the (Brillouin zone integrated) local density of states $\rho_{\uparrow\downarrow}(E)$ at the respective energies.

The variation of the wave function amplitudes with the lateral sphere position is clearly higher over graphene than above clean Ni, which can be seen in Fig. 5.12(e,f). It is visible that the corrugations measured above graphene on Ni mainly arise from graphene derived p_z states. Similar to the case of graphite [97], the peculiar symmetry of these states induces an asymmetry in STM images. For small bias voltages, hence close to E_F, the upper graphene p_z-derived band crossing E_F near the M point contributes strongly to the corrugation in the majority spin channel. The lower p_z band and small contributions from Ni d bands induce the corrugation in the minority spin case. Above clean Ni(111) the STM experiments measure smaller corrugations, which mainly originate from slight lateral variations in the surface states near the center of the Brillouin zone. It becomes clear that the corrugations above the graphene sheet are of electronic origin and are also brought about by the quenching of the Ni surface states as can be seen in the data.

5.6 Kerr-Microscopy results

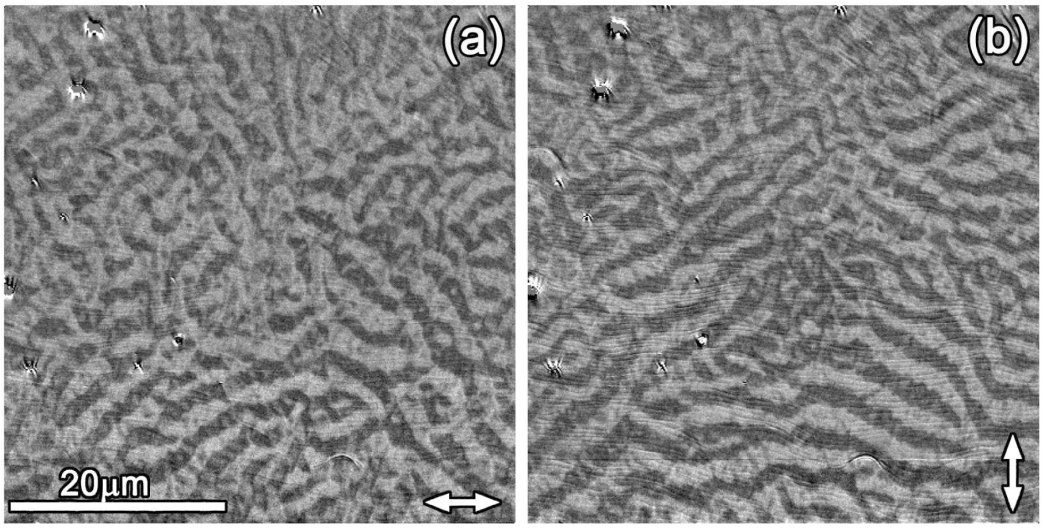

Figure 5.13: Kerr microscopy images of the magnetic structure of the Ni(111) single crystal. The gray-scale amplitude of the images is proportional to the in-plane magnetization component which is indicated by a double arrow in the lower right corner.

To identify the large-scale magnetic domain structure, the domain pattern of Ni(111) was studied by means of Kerr microscopy. Measurements were done by F. Lofink, S. Hankemeier and R. Frömter from Prof. H. P. Oepen's group of Applied Physics of Hamburg University. Kerr microscopy utilizes the

magneto-optic Kerr effect (MOKE) to visualize the magnetic surface structure at ambient conditions. An arbitrary magnetization component can be selected for imaging by using appropriate apertures in the back focal plane. A lateral resolution of 300 nm was achieved and imaging in external fields was possible.

An in-plane measurement shows a recurring magnetic pattern that varies slightly for different demagnetization cycles while no indication for an out-of-plane component is found. In Fig. 5.13 the horizontal (a) as well as the perpendicular component (b) of the in-plane magnetization is shown. The in-plane magnetic pattern is characterized by magnetic structures of two length scales: a stripe domain pattern with a stripe width in the range of 3 μm to 6 μm which varies the orientation in different sample areas. Inside each of these stripes one can see a wavy pattern indicative of a magnetic fine structure on a smaller length scale. A real-time observation of the Ni(111) single crystal during the application of an external magnetic in-plane field shows that at about 13 mT the domain walls begin to move. A field of 140 mT is sufficient to create a single domain state.

5.7 SEMPA results

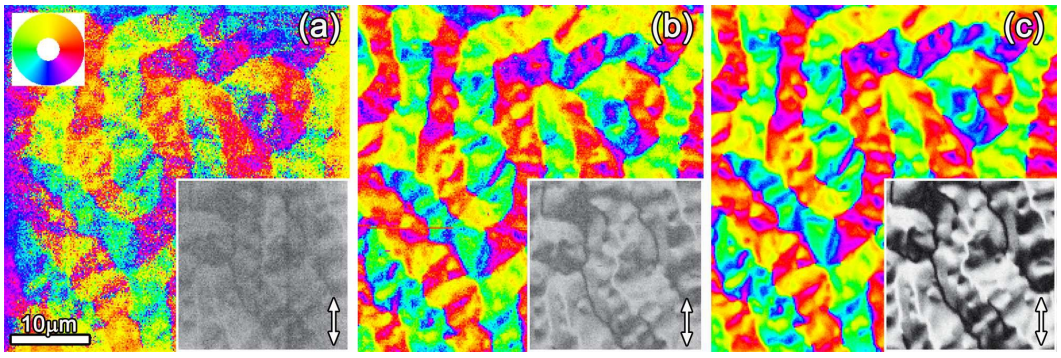

Figure 5.14: SEMPA images of the magnetic structure of the Ni(111) surface at the same position, but with different surface preparations. Encoded in color is the direction of the in-plane magnetization, as defined by the 360° color wheel. In (a) the surface is covered with graphene. (b) gives the signal from the clean Ni surface after sputter-cleaning. For contrast enhancement, in (c) a thin iron layer has been deposited. To emphasize the changes in contrast, the lower right part of each image gives the y-component of the magnetization in a gray-scale representation.

To get a more detailed picture of the surface magnetic domain structure, high-resolution SEMPA measurements were performed. Experiments were conducted by F. Lofink, S. Hankemeier and R. Frömter from Prof. H. P. Oepen's group of Applied Physics of Hamburg University. With SEMPA, a simultaneous vectorial mapping of both orthogonal in-plane magnetization components at the surface [98] was achieved. Magnetization images of 20 nm

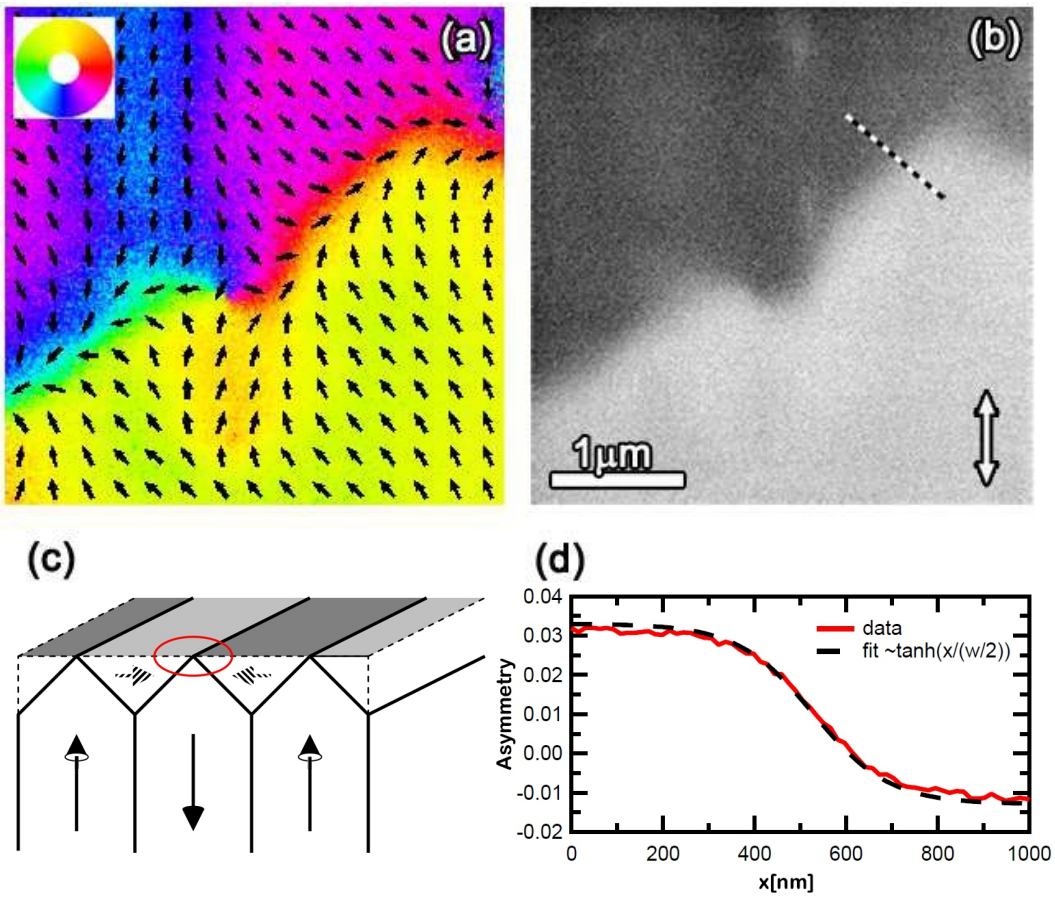

Figure 5.15: High resolution SEMPA images of the Néel-like walls at the Ni(111) surface. In (a) the in-plane distribution of the magnetization of the Ni(111) surface is shown. Encoded in color is the direction of the in-plane magnetization, as defined by the 360° color wheel. In addition, the direction is illustrated by the arrows. In (b) the y-component of the magnetization is shown in a gray-scale representation. The striped line indicates the path of the wall profile shown in (d). (c) Sketch of a section across a V-line on the surface, illustrating the corresponding volume domain structure. The striped arrows indicate the branched structure of the corresponding domains. (d) The wall-profile is fitted by Eq. (5.1) This fit yields a wall width $w = 330 \pm 6$ nm.

lateral resolution were acquired at RT using a primary beam of 6 nA at 8 keV. The SEMPA instrument is located in a separate UHV-facility at 5×10^{-11} mbar base pressure, into which graphene-coated Ni(111) samples were transferred. To remove the graphene layer, Ar^+ ion etching at 600 eV without post annealing was used. For contrast enhancement, 4 AL of Fe were deposited from an e-beam evaporator at 0.2 AL/min.

The SEMPA image in Fig. 5.14(a) shows a characteristic section of the magnetization pattern of the graphene-covered Ni(111) single-crystal surface, after transfer under ambient conditions. Although no further treatment of

the surface was performed, a distinct magnetic contrast, i.e. a polarization asymmetry of 1.2 %, can be observed. The observation of magnetic contrast in SEMPA without in situ cleaning of the sample is most unusual, because of the sub-nm surface sensitivity of secondary-electron (SE) spin polarization. Therefore, the Ni(111) surface is effectively passivated by the graphene layer, which is in accordance with recent spectroscopy data [75].

To check for any graphene-induced change of signal and/or domain pattern, Figure 5.14(b) shows the same area of the sample as in (a) after argon ion sputtering. While the domain structure is unchanged, the clean Ni surface exhibits a much stronger magnetic contrast corresponding to a 2.4 % asymmetry. The sign of the SE spin polarization is preserved, which indicates, that in the SE cascade process the graphene does not cause a polarization inversion. This should not be confused with the calculations given in Fig. 5.11, as SEMPA detects free electrons in vacuum at energies above > 5 eV with respect to the Fermi level, which carry a spin information originating from scattering events mostly in the topmost Ni layers [75]. The image quality can be improved by depositing a small amount of iron (≈ 4 AL) onto the surface. Due to its higher saturation magnetization and the sub-nm surface sensitivity of SEMPA the iron acts as polarizer for the secondary electrons. The result can be seen in Fig. 5.14(c) and again the domain pattern is identical to (a) and (b), while the contrast is enhanced to give a polarization of 6.7 %. To emphasize the changes in contrast, the lower right part of each image gives the y-component of the magnetization in a gray-scale representation.

The SEMPA measurements confirm the results from Kerr microscopy and provide images of the surface magnetic domain pattern at higher resolution: it consists of a larger length-scale stripe pattern with a width from 3 μm to 6 μm. However, these larger stripes are not single domains but instead the magnetization within the stripes is more or less regularly modulated by a second type of stripes, on a smaller length-scale from 1 μm to 3 μm. From one of these small stripes to the next, the magnetization changes by approximately 60 degrees, which results in a net magnetization of the large stripes. The transitions between the smaller stripes are very broad yielding a rather wavy pattern without sharp domain walls. In contrast, the large stripes are separated by sharp Néel-like walls, which are of the 180° type. Figure 5.15(a) shows a higher magnification of the domain structure around such a head-to-head domain wall. The y-component of the magnetization is shown in (b). The striped line indicates the position of the wall profile plotted in Fig. 5.15(d). It can be described by Eq. (5.1), and a fit yields a domain wall width $w = 330 \pm 6$ nm. The observation of much narrower domain walls by SP-STM does not contradict the SEMPA results: in first order approximation the width of a Néel wall is proportional to $K_1^{-1/2}$, where K_1 is the first order magneto-crystalline anisotropy constant. It was shown in Section 5.1 that K_1 is strongly temperature dependent. Works in Refs. [99; 100] report on $K_1 = -0.0045\ MJ/m^3$ at RT compared to $K_1 = -0.12\ MJ/m^3$ at 4 K. Therefore, a reduction of wall width with temperature is expected. Using the width from the SEMPA measurements as

starting point, one can estimate a wall width at 4 K of approximately 70 nm, in reasonable agreement with the wall width found using SP-STM. Furthermore, SEMPA measurements found that the magnetic pattern of Ni(111) changes completely after cooling down to $T = 80$ K (Fig. 5.16(a)), and does not recover at RT to the structure observed before the cooling (cp. Fig. 5.16(b) and Fig. 5.14). Such an unusual behavior of the magnetic pattern with temperature was not studied in detail in the framework of my PhD thesis, thus requires further experimental investigations.

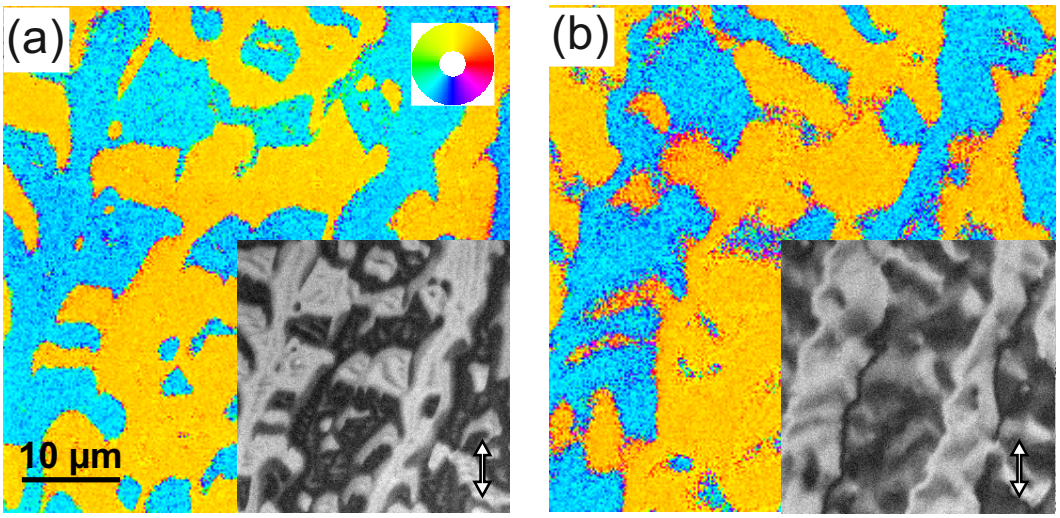

Figure 5.16: SEMPA images of the magnetic pattern of Ni(111) at the same position, but at different temperatures: (a) $T = 80$ K and (b) RT. Encoded in color is the direction of the in-plane magnetization, as defined by the 360° color wheel. To emphasize the changes in contrast, the lower right part of each image gives the y-component of the magnetization in a gray-scale representation. By comparison to Fig. 5.14, the observed magnetic structure is completely different and does not recover at RT after the cooling.

To reveal the origin of the observed surface magnetic pattern it is crucial to understand why the Néel walls have a head-to-head or tail-to-tail configuration as seen in the SEMPA images. If this pattern persisted into the volume, it would imply a huge amount of dipolar energy. Instead, this pattern is indicative of a so-called V-line structure [51], where two volume domain walls with different orientations merge at the surface into a single line. In a cross-section perpendicular to the line, this structure appears like a V where the magnetization of the center domain collects all the flux that originates from the oppositely magnetized side domains (see Fig. 5.15(c)). So the surface pattern is flux compensated in the volume to reduce the dipolar energy. As the magnetic surface structure of the V-lines imaged in Fig. 5.15 shows only an in-plane magnetization one can interpret it as the Néel cap of a V-line, in analogy to the well-understood Néel cap of a Bloch wall e.g. in Fe(001) [101]. Indeed, the measurements give no indication of an out-of-plane component of

the magnetization in the domains or the domain walls, in agreement with the Kerr-microscopy measurement. Thus, the conclusion is that the magnetization at the surface is entirely in-plane. This may be surprising, as none of the magnetically easy ⟨111⟩-directions of the Ni crystal lies within the (111) surface of the sample. This finding can only be explained as a consequence of a reduction of stray field energy at the expense of local anisotropy within a certain depth of subsurface volume. A comparison of the upper limit of the shape anisotropy of the crystal $K^V_{shape} = 0.17\ MJ/m^3$ [21] to the magneto-crystalline anisotropy constant in first order K_1 at RT, a ratio of 38:1 is obtained. This might explain the in-plane orientation of the observed magnetic pattern.

The above-described features of the magnetic pattern of the surface of the Ni(111) crystal can be understood qualitatively using the quasi-domain branching approach for large crystals with strongly misoriented surfaces given by Hubert and Schäfer [51] (see Section 5.1). For a Ni platelet with (111) surfaces the model assumes 180°-oriented base domains in the volume, which reduce the magnetostrictive energy of the crystal. The lateral extent of these domains would be responsible for the length scale of the larger stripes found on the surface. In the mentioned quasi-domain branching concept, quasi-domains with a net magnetization parallel to the surface are introduced, which close the flux of the basis volume domains. They are composed of alternating domains oriented along the easy directions. Each of these first-level branching domains acts as basis domain for second-level branching and thus forms its own closure quasi-domain at the surface to further reduce the stray-field energy. In the model, the energy gain by branching of the closure domains in comparison to the amount of domain wall energy needed for further branching determines the branching depth that is finally observed. In SEMPA measurements, a two-level branching is observed only, where at least the surface of the second level domains is already fully in-plane oriented. This is in contrast to the model of Hubert, where quasi domains along the out-of-plane canted easy axes are expected even on the final level of branching.

5.8 Single magnetic atoms on graphene/Ni(111)

As it was mentioned in Chap. 1, the main goal of this thesis is to investigate properties of individual atoms on different decoupling layers on magnetic surfaces. Graphene/Ni(111) becomes the focus of the current research due to its role as a perfect substrate for a single atoms study. After investigating graphene/Ni(111) in detail (see previous Sections), individual magnetic atoms were adsorbed on top and studied by means of STM and STS. In order to prevent diffusion, atoms were deposited onto the cold sample inside the STM ($T_{\max} = 20$ K).

Magnetic atoms can, in general, adsorb to the high-symmetry sites of the

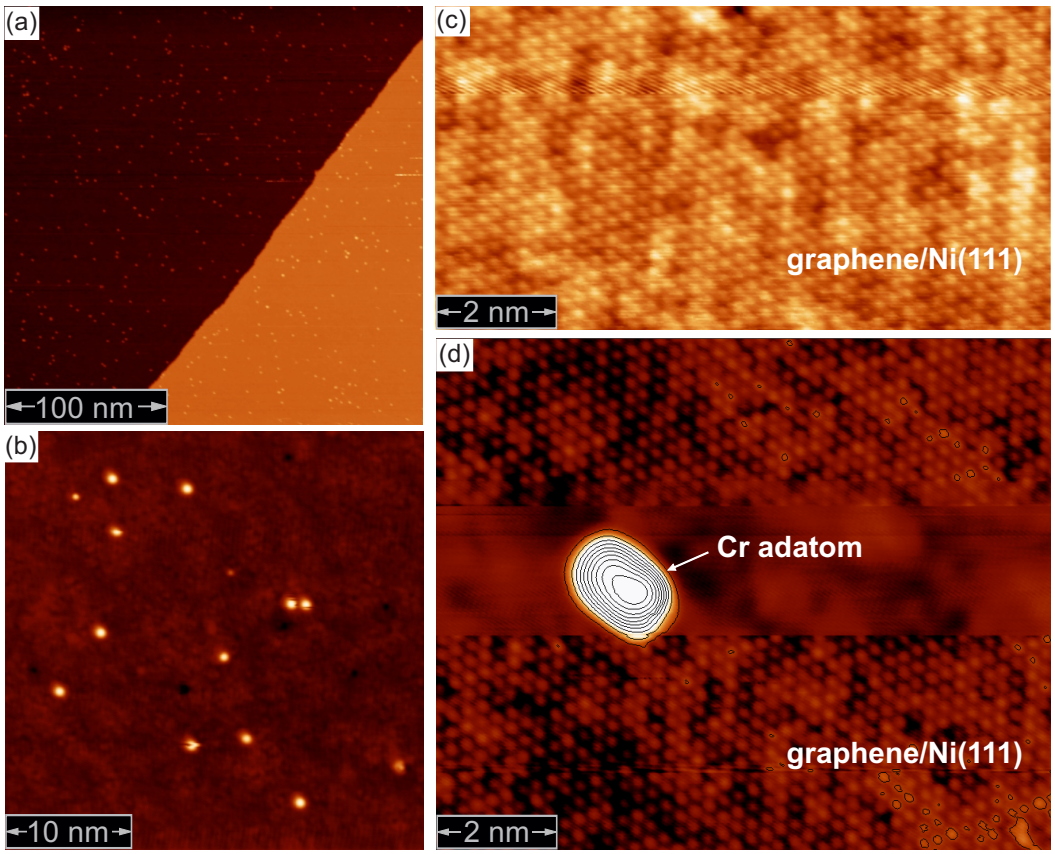

Figure 5.17: Constant-current images of individual Cr atoms on graphene/Ni(111): (a,b) Overview of the sample surface, (c) adatom-free area and (d) a single adatom adsorbed on top. Measurement parameters: (a,b) $U = 100$ mV and $I = 0.1$ nA, (c) $U = 2$ mV and $I = 10$ nA, (d) $U = 2.5$ mV and $I = 10$ nA for graphene/Ni(111) area and $U = 10$ mV and $I = 0.8$ nA for a region with a Cr adatom. All data were taken at $T = 8$ K.

graphene lattice: above the center of a hexagon (h-site), on top of a C atom (t-site) and above the middle of the bridge (b-site) [102; 103]. However, magnetic $3d$ adatoms including Fe, Co and Ni were predicted theoretically to occupy the h-site on free-standing graphene [104; 105] under the assumption of moderate local Coulomb interactions [102; 106]. In fact, the h-site of Ni adatoms on graphene/SiC(0001) was determined experimentally using the atomically resolved STM topographies [107]. Here, Figs. 5.17(a,b) show typical constant-current images of a sample where Cr atoms on graphene/Ni(111) appear as protrusions of about 0.12 nm height at $U = 100$ mV. At higher magnification, atomic resolution of graphene/Ni(111) was observed (Fig. 5.17(c)). Since adatoms are weakly bounded to graphene and can be easily affected by a tip, I performed measurements in two tunneling regimes by varying values of U and I in order to simultaneously image a single Cr adatom on graphene/Ni(111) and getting atomic resolution on the substrate (see

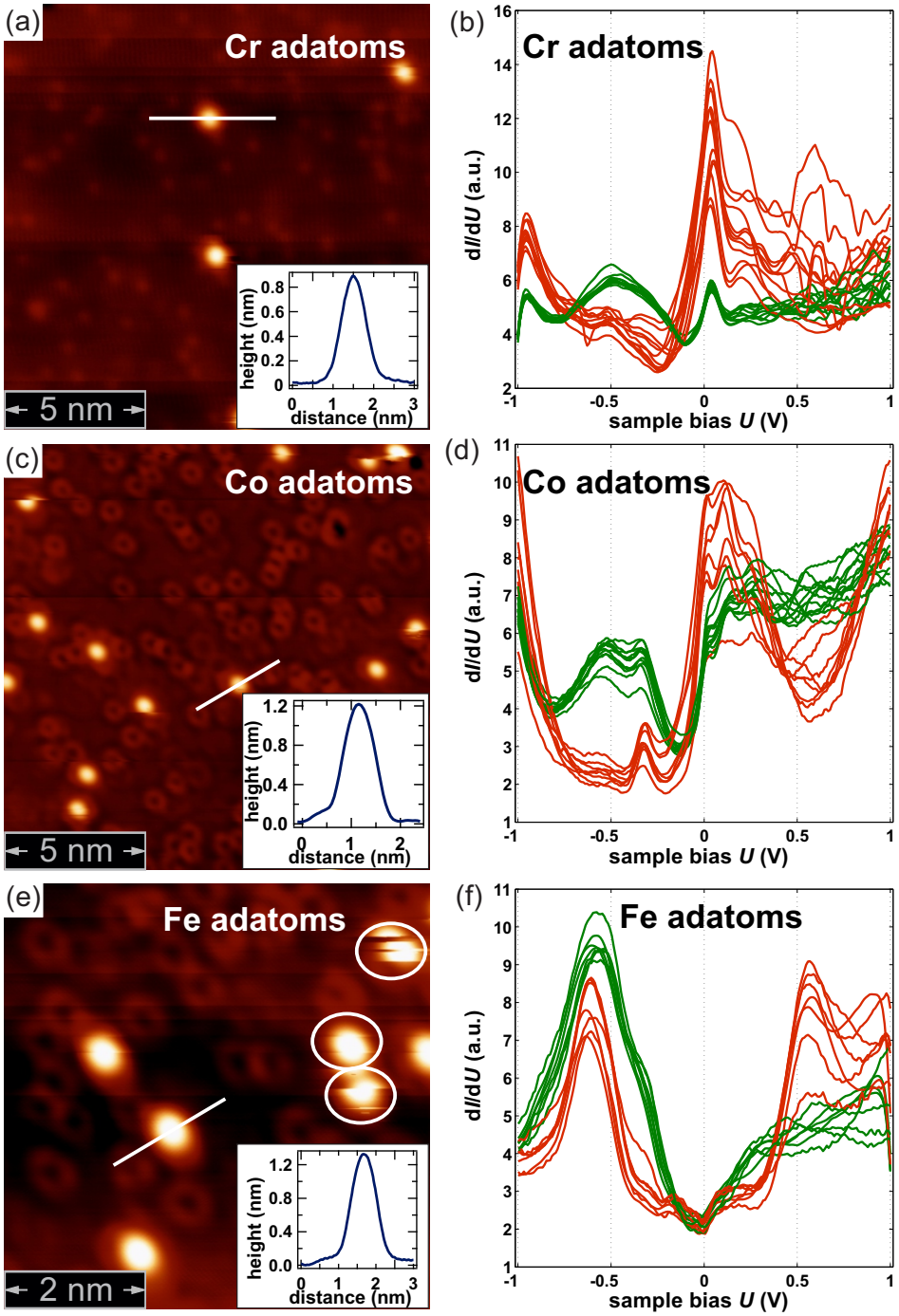

Figure 5.18: Cr, Co and Fe adatoms on graphene/Ni(111): (a,c,e) constant-current images and (b,d,f) single spectra of magnetic atoms (red) and substrate (green). Inserts in (a,c,e) show profiles of the apparent height of the adatoms, taken along lines indicated in respective STM images. White circles in (e) indicate the fact that adatoms are weakly bounded to the substrate. Measurement parameters: (a,b) $U = -1$ V, $I = 0.5$ nA, $U_{\mathrm{mod}} = 18$ mV; (c,d) $U = 1$ V, $I = 0.5$ nA, $U_{\mathrm{mod}} = 15$ V; (e,f) $U = 1$ mV, $I = 0.5$ nA, $U_{\mathrm{mod}} = 18$ mV.

Fig. 5.17(d)). The tunneling regime to image single atoms without inducing diffusion with $U = 100$ mV and $I = 0.8$ nA and that for graphene/Ni(111) with $U = 3$ mV and $I = 10$ nA were used. The adatom, however, appears asymmetric in Fig. 5.17(d), which means that its lateral position was changed. Based on these measurements, it is therefore not possible to identify the adsorption site of the adatom with respect to the underlying substrate.

To investigate the energy-resolved electronic structure of magnetic atoms such as Cr, Co and Fe on graphene/Ni(111), I performed STS measurements with bare W tips. Figures 5.18(a,c,e) and (b,d,f) show topographies of the samples and spectroscopic data. Spectra of the substrate (green) were recorded at areas located far from adatoms, while spectra of adatoms (red) were acquired by positioning the tip over the center of atomic protrusions. Though measurements were done with different tips, all graphene/Ni(111) spectra in Figs. 5.18(b,d,f) show a common broad maximum at $U = -500$ mV, whereas they are rather featureless in the positive bias regime. The resonance at $U = -0.5$ V most likely arises from a Ni(111) surface state since it is also found on the bare surface (see Fig. 5.5(d)). Several features can be observed in spectra of single adatoms: Cr adatoms show resonances around E_{F} and at $U \approx -1$ V in Fig. 5.18(b); those of Co atoms appear at $U \approx -0.3$ V and $U \approx 0.1$ V (Fig. 5.18(d)), and Fe atoms have peaks at $U \approx \pm 0.6$ V (Fig. 5.18(f)). However, since spectroscopic features of Cr and Co adatoms also present in spectra of the substrate, they are either tip states or caused by adsorbate contamination, most probably hydrogen. In general, all spectra of the substrate and those of adatoms show some deviations, i.e. each single spectrum differs from others. This observation can be attributed to the following reasons:
(i) Graphene/Ni(111) was still contaminated. Indeed, numerous sub-surface defects can be clearly seen in STM images (Figs. 5.18(a,c,e));
(ii) The spectrum of graphene/Ni(111) does not show any outstanding features. Since graphene fully covers the Ni surface, a comparison to the well-investigated spectrum of the bare Ni(111) is complicated. The interpretation of the spectra of adatoms is therefore also difficult.
(iii) Adatoms can occupy different adsorption sites which are mentioned above.
(iv) All atoms show high mobility at the measurement temperature of $T = 8$ K (see atoms marked by white circles in Fig. 5.18(e)). The similar phenomenon was observed in [108] where Fe adatoms are reported to be weakly bounded to graphene/Ru(0001) at $T = 5$ K.
In order to observe purely magnetic spectroscopic features of adatoms on graphene/Ni(111), it is therefore required to prepare an atomically clean Ni(111) surface which is partially covered with graphene, and perform SP-STM measurements using Cr-coated W tips. This was not possible within the framework of this thesis since I could not get rid of residual contamination of Ni(111) and the island growth of graphene failed.

5.9 Summary

Finally, I would like to summarize the main aspects of the graphene/Ni(111) study. (i) The differential conductance of bare Ni(111) was probed by STM and compared to DFT calculations: the observed features could be attributed to a minority spin surface resonance below, and the Shockley state of both spin character above E_{F}. (ii) For graphene/Ni(111), STM images showed a triangular lattice of the atomic structure and an enhanced corrugation compared to bare Ni(111). DFT showed that both properties are a purely electronic effect originating from graphene p_z states around E_{F} and the quenching of Ni surface states. (iii) Kerr microscopy and SEMPA measurements revealed an entirely in-plane magnetic pattern of Ni(111) which stems from a two-level branching of the domain structure. (iv) Domain walls can be easily moved in low external magnetic fields or by the stray field of a magnetic tip. A single in-plane domain state was observed at RT in an in-plane magnetic field of 140 mT. (v) The reactive properties of Ni(111) are passivated by the graphene layer well enough for magnetic imaging after transfer through air. The magnetic structure of graphene-coated Ni is unchanged compared to that of bare Ni(111). (vi) As a result of surface state quenching, the DFT calculations predict an inversion of spin polarization above the graphene layer with respect to the pristine Ni(111) surface. (vii) Fe, Co and Cr atoms adsorbed on top of graphene/Ni(111) were studied by STS. However, due to residual sub-surface contamination of Ni(111), fully-closed monolayer growth of graphene, and high mobility of adatoms, more detailed investigations of the system are required.

Chapter 6

Polarized Pd adlayers and adsorbed Co atoms

This chapter covers the topic of emergent magnetism of Pd, introduces a previous study of the magnetic substrate Co/Ir(111) and shows experimental as well as theoretical results of the spin-resolved electronic properties of mono- and double-layer Pd on Co/Ir(111) and Co atoms adsorbed on top.

6.1 Emergent magnetism

Emergent magnetism is a phenomenon of the onset of magnetic ordering in nanostructures of materials that are non-magnetic in the bulk. The materials are usually strongly exchange-enhanced Pauli paramagnets such as Pd, Rh and Pt, which nearly satisfy the Stoner criterion (see Chap. 2). The physical origin of the emergent magnetism depends on the materials, but is generally linked to defects, doping, surface effects, quantum size effects and direct contact to magnetic materials [22].

Here, I will discuss emergent magnetism on the example of Pd. The free Pd atom with a $4d^{10}5s^0$ configuration is non-magnetic, though it is directly below the strong ferromagnet Ni in the periodic table. In bulk Pd the $4d$ band is not entirely filled: approximately $0.6d$ holes are available for polarization [109]. However, the repulsive intra-atomic Coulomb or electron-electron ($e-e$) interactions are so strong that the $4d$ band is near the threshold of becoming ferromagnetic. For bulk fcc Pd, $ID(E_\mathrm{F}) \approx 0.8$, where I is the Stoner parameter, and $D(E_\mathrm{F})$ is the density of states at E_F. The intra-atomic $e-e$ interactions can be enhanced by increasing the atomic volume, or by neighboring Fe or Co atoms. In fact, an onset of ferromagnetism in fcc Pd for a 4 %−6 % increase in the lattice constant was predicted in [110; 111]. G. G. Low et al.

showed that a Co atom induces ferromagnetic polarization of the surrounding Pd atoms and that the polarization extends to about 10 Å [112]. As a result, giant magnetic moments of 10 μ_B of Co impurities in Pd were found [28]. Furthermore, the Co and Fe overlayers were reported to induce a noticeable magnetic moment in the two nearest layers of a Pd substrate [113]. A similar phenomena was observed in Co/Pd multilayers. H. J. G. Draaisma et al. and J. V. Harzer et al. observed that the saturation magnetization of Co/Pd multilayers with n_{Co}=1 and 2 was larger than the magnetization of Co bulk [114; 115]. R. H. Victora et al. calculated the magnetic moment of Co/Pd multilayers with n_{Co}=1 and reported that it was larger than the moment of Co bulk [109].

In my thesis, I have investigated electronic and magnetic properties of ML and double-layer (DL) Pd on a system of Co/Ir(111), and Co atoms adsorbed on top. SP-STM experiments showed that a spin contrast can be achieved on both Pd adlayers and Co adatoms. The magnetic nature of the observed contrasts was clarified by DFT calculations.*

6.2 Previous study of Co/Ir(111)

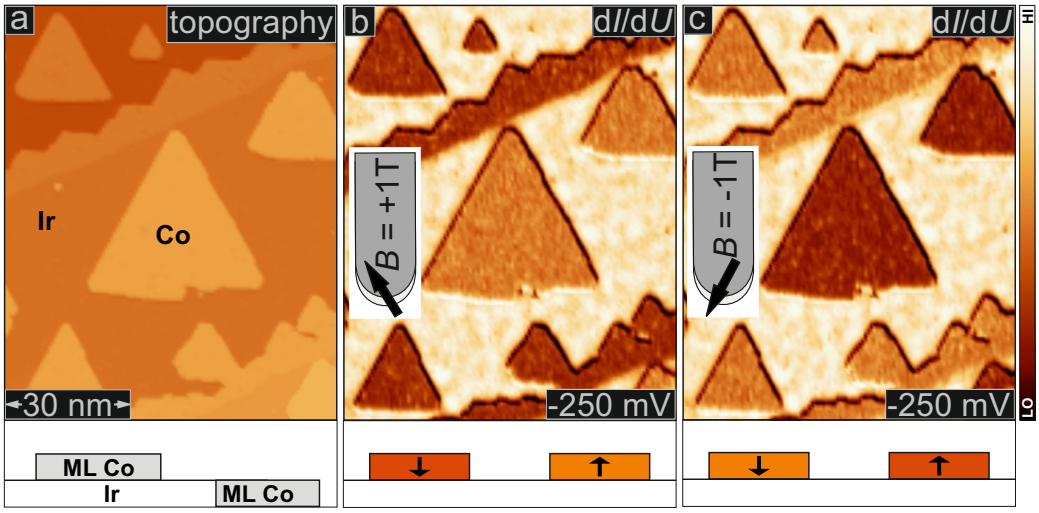

Figure 6.1: SP-STM measurements of Co/Ir(111) with Fe-coated W tips: (a) Constant current image measured at $B = +1$ T. (b) and (c) Spin-polarized dI/dU maps measured at $B = +1$ T and $B = -1$ T, respectively. Color bar shows variations of the spin-polarized dI/dU signal. Sketches in (b) and (c) schematically illustrate the principle of inversion of the magnetic out-of-plane contrast. Measurement parameters: $I = 2$ nA, $U = -250$ mV and $U_{mod} = 20$ mV.

*Corresponding to calculated fcc lattice constants of Pd a_0 = 3.863 Åand Ir a_0 = 3.89 Å, there is a 0.7 % lattice mistmatch between film and substrate.

As a basic magnetic substrate, a system of Co/Ir(111) was chosen since its morphology, electronic as well as magnetic properties are well-investigated in a previous study [116]. An Ir(111) single crystal was prepared by sputtering, annealing to $T = 1300$ K for 1 min, and then cooled down for 10 min. Cobalt was deposited by electron bombardment heating of a Co rod to evaporate material in a line of sight to the Ir substrate. It was shown in Ref. [116] that submonolayer amounts of Co grow pseudomorphically on Ir(111), though there is a 7% lattice mismatch between film and substrate. The deposited Co forms ML high triangular islands on the Ir terraces and ML high wires attached to the Ir step edges (see Fig. 6.1(a)). With very few exceptions, Co was found to grow in one stacking, namely fcc, with respect to the underlaying Ir substrate.

Magnetic properties were investigated with Fe-coated W tips. It was shown that Co islands are single-domain ferromagnetic islands with out-of-plane magnetic anisotropy (Figs. 6.1(b,c)) [116]. A magnetic field of $B = \pm 1$ T was used to align the Fe-coated W tip's magnetization such that it possesses a significant out-of-plane component, whereas the magnetization of Co/Ir(111) was observed to stay unaffected. I found that this is also the case for Pd-covered Co/Ir(111) and therefore I will make use of the possibility to align the tip magnetization in an external magnetic field ($1\text{T} \leq |B| \leq 2\text{T}$) throughout this study.

6.3 Pd adlayers

6.3.1 ML Pd on Co/Ir(111)

Sample morphology and cleanness

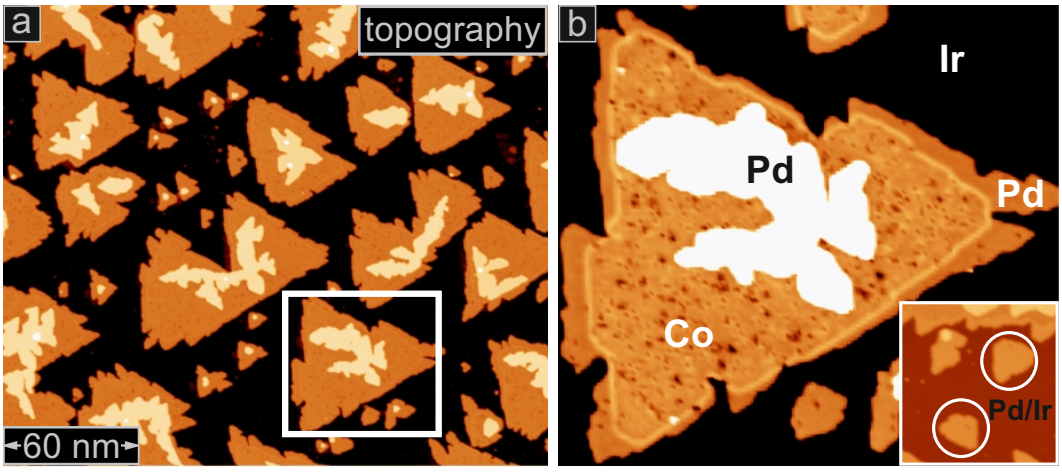

Figure 6.2: (a) and (b) Constant-current images of ML Pd on Co/Ir(111) in the submonolayer regime. The inset of (b) indicates two stackings of ML Pd on bare Ir(111). Measurement parameters: $I = 0.8$ nA and $U = -200$ mV.

After cooling the Co/Ir(111) sample for 30 - 60 min, Pd was evaporated from a 1 mm palladium rod heated by electron bombardment at a rate of about 0.05 ML/min. In the submonolayer regime, Pd of ML height grows on top of Co and decorates Co rims (see Fig. 6.2). Triangular edges of Co rims are rounded compared to those of a pure island, most likely due to a rearrangement of Co atoms under the influence of Pd. A small amount of ML Pd can be found on the Co-free area of the bare Ir(111), too. The inset of Fig. 6.2(b) shows two islands pointing into opposite directions, which indicates different stackings of ML Pd on bare Ir(111). In this coverage regime the growth of both Co and Pd is pseudomorphic with no sign of intermixing. In the following, I focus on Pd/Co.

I observe a fractal growth of Pd with a randomly branched structure with no preferential orientation [117; 118]. In fact, it was shown in experimental studies of Ag/Pt(111) [118], Pt/Pt(111) [119; 120], Au/Ru(0001) [121] and Ag/Pt(111) [117; 118] that fractal growth is expected when randomness dominates (random motion of atoms before they attach), whereas dendritic growth is caused by the influence of anisotropy (due to the lattice symmetry). Theoretical results in Ref. [122] also predict that the fractal growth of thin films is non-linear, i.e. the island size $S(t)$ grows with time t as t^k, where the growth exponent k is slightly less than 1 because of the competition between nucleation and the growth of islands. Moreover, it was indicated that the branch width of islands b increases with increasing island size S as $b \sim S^\alpha$, where α is approximately equal to 1/3 because of the geometrical structure of the triangular substrate. Thus, the fractal fine structure varies according to the experimental conditions such as the deposition rate, the amount of deposited material and temperature of the substrate, which can lead to the individual details of the fractal trees being smeared out.

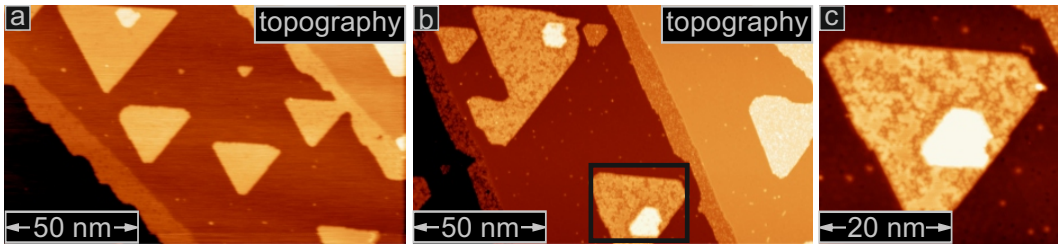

Figure 6.3: Constant-current images of Co/Ir(111) measured on different samples. The sample in (b,c) was exposed to contamination coming from a running Pd evaporator. Contamination is most likely hydrogen (see text). Measurement parameters: $I = 0.8$ nA and $U = -200$ mV.

The fractal growth of Pd can also be attributed to defects in Co. In fact, though Pd films are very smooth with almost no surface defects, I observed that a Co layer underneath becomes contaminated after the deposition of Pd. It is known that Pd is a perfect storage for hydrogen [123]. Since Co is very reactive towards hydrogen [124], contamination likely originates from this gas.

To verify this assumption, I prepared a Co/Ir(111) sample and checked its cleanness in STM (see Fig. 6.3(a)). Again, a newly prepared sample was moved into the chamber with a running Pd evaporator (standard evaporation parameters are $I_{\mathrm{fil}} = 2$ A, $I_{\mathrm{em}} = 7$ mA, $I_{\mathrm{flux}} = 1$ nA and $U = 1$ kV), where it was held *out* of sight of a direct deposition of Pd material for 10 min. As a result, Co films were imaged strongly contaminated (cp. Figs. 6.3(a) and 6.3(b,c)). This indicates that there is indeed some contamination coming out from a hot Pd rod. It was reported in [125; 126] that H_2 adsorbates may change the magnetization of a Co layer due to the hybridization of the $1s$ with $3d$ electrons responsible for magnetism. In my measurements, I observed that the magnetization direction of Pd-capped Co islands is the same as that of pure Co shown in Section 6.2. For samples with a higher coverage of Pd, it was however difficult to achieve a spin contrast on Pd-free Co areas due to hydrogen contamination (see Section 6.3.2)).

Electronic and magnetic properties

I studied the electronic and magnetic properties of Pd-capped Co islands by means of SP-STM using Fe-coated W tips. Figure 6.4(b) shows a constant-current image of the same region as Fig. 6.4(a) colorized with the simultaneously acquired $\mathrm{d}I/\mathrm{d}U$ signal at $U = +100$ mV; to simplify the discussion at this point I chose an image taken at a bias voltage where the spin-polarized contribution to the signal vanishes for both Co as well as Pd on Co layers. In agreement with previous results [116] I observe a single $\mathrm{d}I/\mathrm{d}U$ level on all Co ML areas, due to the preferred growth with only one type of stacking. In contrast, for Pd/Co two different contrast levels are observed which I interpret as the two possible stackings of the Pd monolayer on Co/Ir(111), labeled Pd_A and Pd_B in the following.

Next, I show the sample measured at a bias voltage such that both stacking and magnetic contrasts are observed. Figure 6.4(c) displays the constant-current image colorized with the $\mathrm{d}I/\mathrm{d}U$ signal at $U = -400$ mV, for which the magnetism of Co is detected as well. In the following, Co islands presenting the higher $\mathrm{d}I/\mathrm{d}U$ signal at $U = -400$ mV are referred to as Co↑, while Co islands with the lower $\mathrm{d}I/\mathrm{d}U$ signal are denoted by Co↓ (for tip magnetization along $+B$). This notation is arbitrary since the relative orientation of tip and island magnetization is unknown. A significant contrast is also visible on Pd/Co, which has its origin in a different stacking as well as different magnetization directions. The two contributions can be disentangled by either comparing with the non-spin-polarized $\mathrm{d}I/\mathrm{d}U$ map of Fig. 6.4(b) or comparing with a $\mathrm{d}I/\mathrm{d}U$ map with opposite z-magnetization component of the tip, Fig. 6.4(d). For the latter case, the magnetic contributions to the contrast are inverted. The observation of spin contrast on Pd means that the LDOS measured a few Ångströms above the surface is substantially spin-polarized. By comparison to Fig. 6.4(b), I denote Pd films of one particular stacking as Pd_A↑ (Pd_B↑) if residing on Co↑ islands, and Pd_A↓ (Pd_B↓) if residing on Co↓ islands.

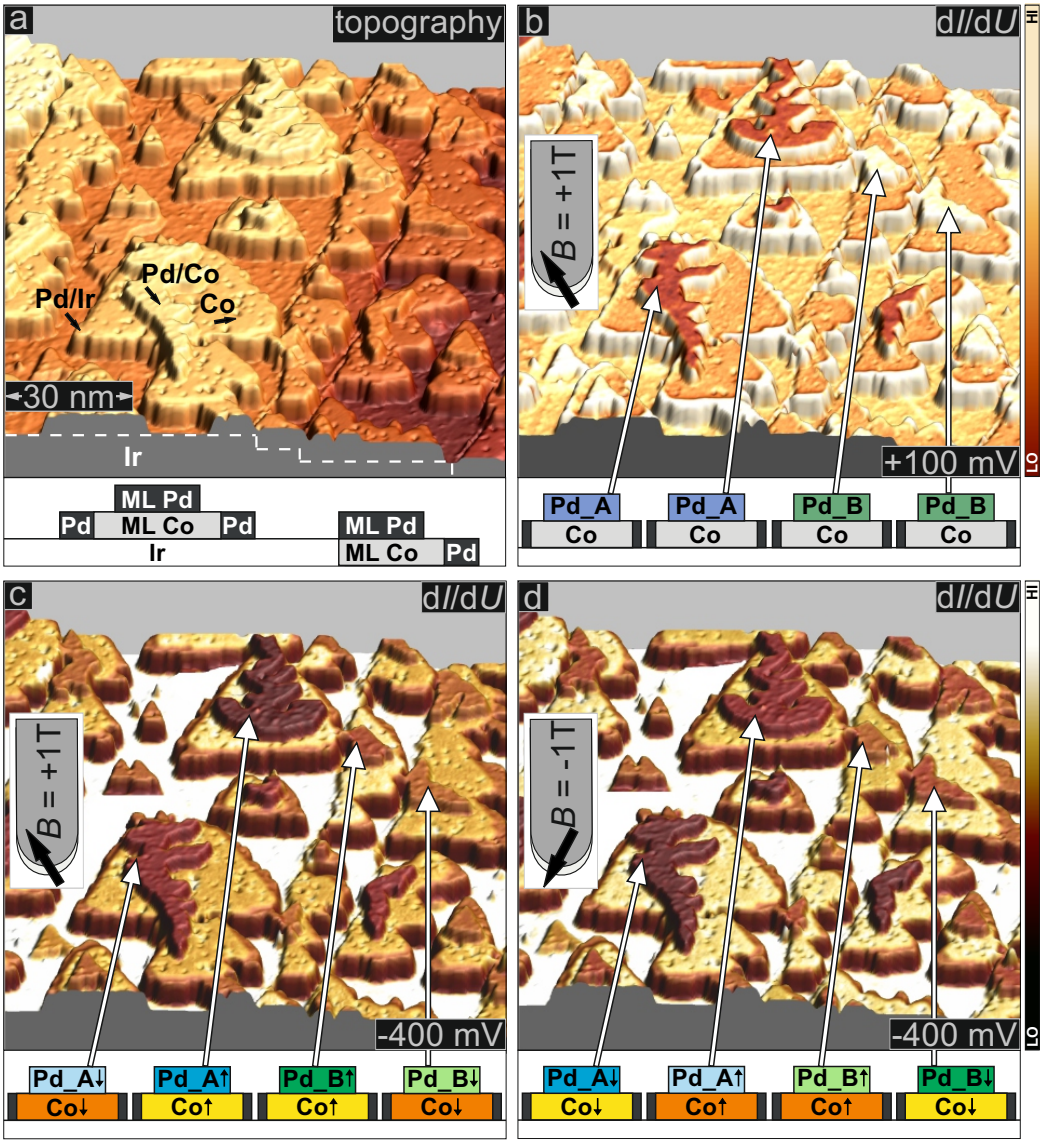

Figure 6.4: SP-STM measurements of ML Pd on Co/Ir(111): (a) Constant-current image and (b) Constant-current image colorized with the simultaneously acquired $\mathrm{d}I/\mathrm{d}U$ signal at $U = +100$ mV where the spin-polarized contribution vanishes, measured at $B = +1$ T. (b) and (c) Constant-current images of the same sample area colorized with the simultaneously acquired spin-resolved $\mathrm{d}I/\mathrm{d}U$ signal at $U = -400$ mV, measured at $B = +1$ T and $B = -1$ T, respectively. Color bars show variations of the spin-polarized $\mathrm{d}I/\mathrm{d}U$ signal. Sketches schematically demonstrate contrast levels observed on Co and Pd/Co. Measurement parameters: $I = 0.8$ nA and $U_{\mathrm{mod}} = 25$ mV.

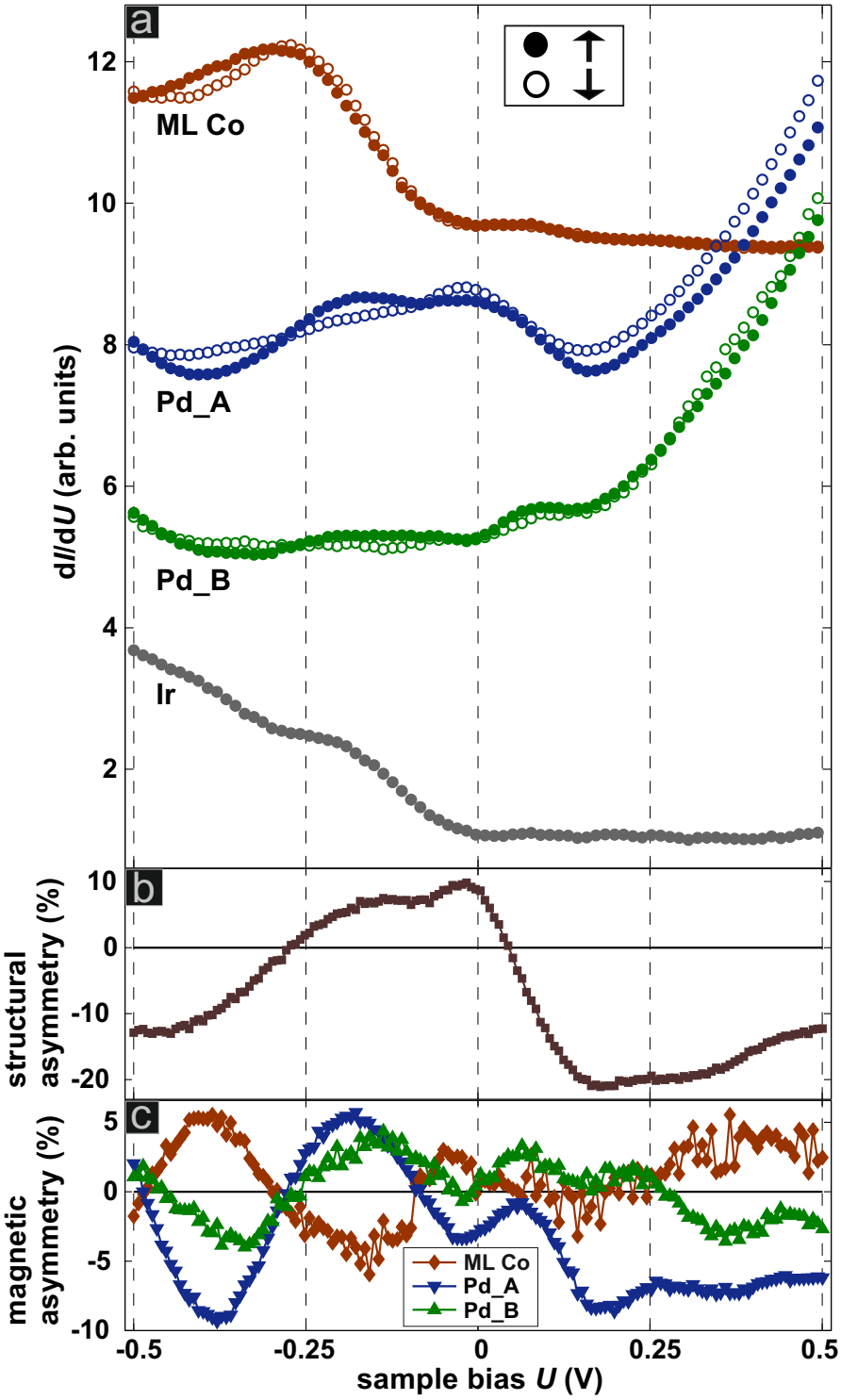

Figure 6.5: SP-STS measurements of ML Pd on Co/Ir(111): (a) Spin-resolved $\mathrm{d}I/\mathrm{d}U$ spectra ($U_{\mathrm{stab}} = -500$ mV, $I_{\mathrm{stab}} = 0.8$ nA, $U_{\mathrm{mod}} = 25$ mV) measured at $B = +1$ T. Each spectrum displayed is an average of 5 single spectra. Co and Pd/Co spectra are shifted vertically by multiples of 3 arb. units for clarity. (b) Structural asymmetry calculated for spin-averaged spectra of Pd/Co of different stacking, namely Pd_A and Pd_B. (c) Magnetic asymmetries calculated for spin-resolved spectra of ML Co, Pd_A and Pd_B.

All contrast levels of the sample are schematically shown in the sketches of Figs. 6.4(c,d).

To get access to the spin- and energy-resolved electronic structure of the surface I performed SP-STS. Figure 6.5(a) shows the spin-resolved $\mathrm{d}I/\mathrm{d}U$ spectra obtained above Ir(111), ML Co↑,↓, Pd_A↑,↓, and Pd_B↑,↓, at $B = +1$ T. The Ir(111) spectrum exhibits an increasing $\mathrm{d}I/\mathrm{d}U$ signal towards more negative bias below E_F, and the spin-polarized $\mathrm{d}I/\mathrm{d}U$ spectra of ML Co are rather featureless in the positive bias regime but have a characteristic peak at $U \approx -270$ mV, in good qualitative agreement with the previous study in Ref. [116]. I observe that all spectra of Pd/Co exhibit an increasing $\mathrm{d}I/\mathrm{d}U$ signal above E_F and no outstanding spectroscopic features below E_F.

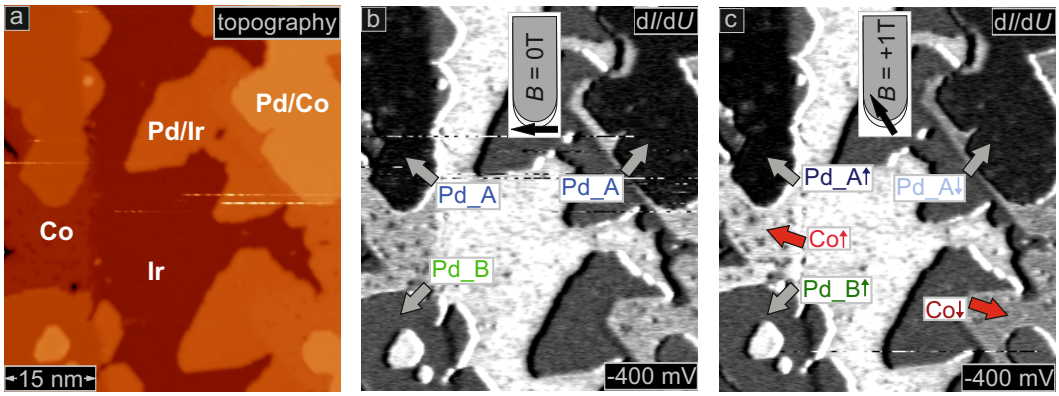

Figure 6.6: Pd/Co/Ir(111) sample: (a) Topography, (b) and (c) spin-resolved $\mathrm{d}I/\mathrm{d}U$ maps measured at $B = 0$ T and $B = +1$ T, respectively. Measurement parameters: $I = 1.5$ nA, $U = -400$ mV and $U_\mathrm{mod} = 30$ mV.

To distinguish the spectroscopic differences due to stacking from those due to magnetism, I calculate the structural and the magnetic asymmetry of the spectra. The asymmetry is defined by

$$A(U) = \frac{\mathrm{d}I/\mathrm{d}U(U)_1 - \mathrm{d}I/\mathrm{d}U(U)_2}{\mathrm{d}I/\mathrm{d}U(U)_1 + \mathrm{d}I/\mathrm{d}U(U)_2}. \tag{6.1}$$

For the structural asymmetry I use $\mathrm{d}I/\mathrm{d}U_\mathrm{A}$ and $\mathrm{d}I/\mathrm{d}U_\mathrm{B}$ which are the calculated spin-averaged spectra[†] of Pd_A and Pd_B, respectively; for the magnetic asymmetry I use $\mathrm{d}I/\mathrm{d}U_\uparrow$ and $\mathrm{d}I/\mathrm{d}U_\downarrow$ which are the spin-resolved spectra of Co↑ (Pd_A↑, Pd_B↑) and Co↓ (Pd_A↓, Pd_B↓), respectively. The structural asymmetry is plotted in Fig. 6.5(b) and shows that the two different stackings can be distinguished easily in the whole bias regime studied. The magnetic asymmetries of ML Co, Pd_A and Pd_B are shown in Fig. 6.5(c). Interestingly, asymmetries of Pd_A and Pd_B go mostly parallel in the negative bias

[†]The spin-averaged spectra were calculated by $\mathrm{d}I/\mathrm{d}U_i = (\mathrm{d}I/\mathrm{d}U_{i\uparrow} + \mathrm{d}I/\mathrm{d}U_{i\downarrow})/2$, where i is A or B indicating different stackings of Pd.

regime and have the opposite sign compared to that of ML Co. All magnetic asymmetries are in the same range of values up to 5 - 10 %.

To investigate whether I can achieve a spin-polarized signal for Pd at $B = 0$ T, I performed zero- and in-field measurements, i.e. when Fe-coated W tips possess an in-plane and a significant out-of-plane spin component, respectively (see Chap. 4). Figure 6.6 shows the topography of a surface studied, and $\mathrm{d}I/\mathrm{d}U$ maps obtained at $B = 0$ T and $B = +1$ T. In accordance with a previous study of Co/Ir(111) [116], no spin contrast is observed for Pd-free Co areas at $B = 0$ T in Fig. 6.6(b). However, two contrast levels can be clearly seen for Pd, which is due to different stacking. In fact, I observe a magnetic $\mathrm{d}I/\mathrm{d}U$ contrast for Pd films assigned to one stacking, namely Pd_A, and residing on oppositely magnetized Co wires at $B = +1$ T (see Fig. 6.6(c)). These measurements therefore show that the magnetic properties of the surface can only be detected if the magnetization direction of Fe-coated W tips exhibits a significant out-of-plane component. Thus, from this experiment together with the contrast change in magnetic field inversion measurements in Figs. 6.4(c,d), I conclude that Pd-capped Co islands are single domain ferromagnetic with an easy magnetization axis normal to the sample surface.

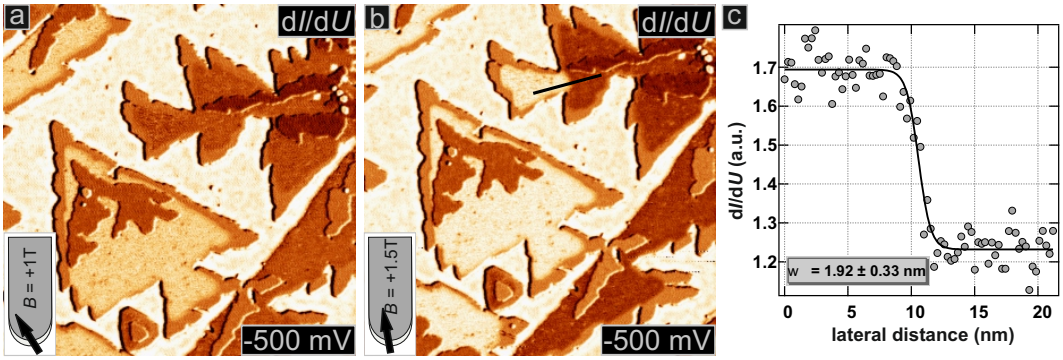

Figure 6.7: (a) and (b) Magnetic $\mathrm{d}I/\mathrm{d}U$ maps of a ML Pd on Co/Ir(111) measured at $B = +1$ T and $B = +1.5$ T, respectively. (c) A line section across a domain wall marked by a black line in (b). Gray circles and a black line represent experimental data and a fitted profile, respectively. Measurement parameters: $I = 1.5$ nA, $U = -500$ mV and $U_{\mathrm{mod}} = 30$ mV.

Few domain walls are present in Pd/Co/Ir(111). They occur only at constrictions in wires or at a coalescence point between two islands (wires) or an island and a wire [116]. For example, with increasing magnetic field from $B = +1$ T to $B = +1.5$ T, I observed a single switching event of the Co magnetization, which caused a domain wall formation in a Pd-free Co layer (see Figs. 6.7). The line section across the domain wall in Fig. 6.7(b) was fitted by a standard wall profile for a 180° Bloch wall, described in Chap. 5. As a result, the fitting yields a domain wall width of $w = 1.92 \pm 0.33$ nm (Fig. 6.7(c)), which is in good agreement with that found for pure Co/Ir(111) (w =2.0 ± 0.14 nm) in Ref. [116]. The domain wall was also detected in a

Pd/Co layer, as marked by red arrows in Figs. 6.8(b,c): the width of the wall is w =1.52 ± 0.33 nm at $B = +1$ T, and it is shifted down by swapping a magnetic field to $B = -1$ T. At $B = -1$ T, a new domain wall also appeared, which was pinned by the coalescence line between two Co wires, as highlighted by a red circle in Fig. 6.8(c). In Fig. 6.14(b) of Section 6.4, I will show another domain wall observed in Pd/Co film, which has a width of w =1.41 ± 0.11 nm (see Fig. 6.16(b), Section 6.4). The fact that the width of walls in the Pd/Co films is comparable to that measured for a pure Co/Ir(111) indicates a high anisotropy of Pd/Co due to the universal relationship between wall width and magnetic anisotropy [116; 21]. The high anisotropy suggests that it will be difficult to switch the magnetization of the Pd-capped Co islands and the remanent magnetization and coercivity values will be high. This is confirmed by the observation of the different spin contrast levels in Pd/Co islands at $B = \pm 1$ T.

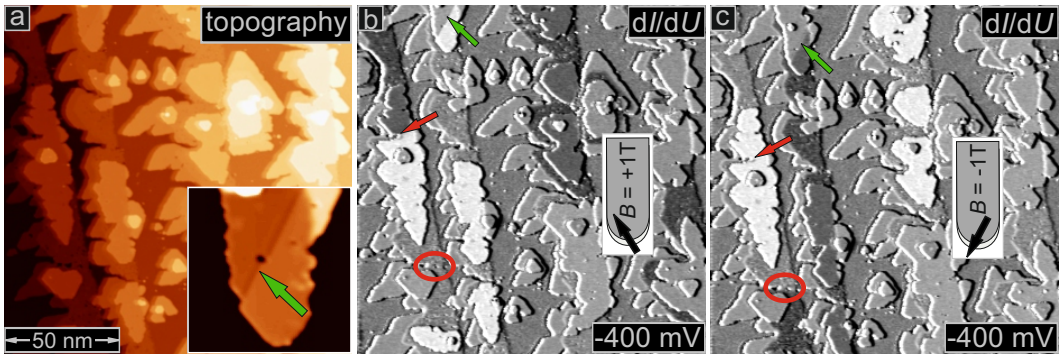

Figure 6.8: (a) Constant-current image and (b,c) magnetic dI/dU maps of Pd wires on Co/Ir(111) measured at $B = \pm 1$ T. A red arrow and a red circle indicate a domain wall, whereas a green arrow marks a dislocation line. Measurement parameters: $I = 1$ nA, $U = -400$ mV and $U_{\mathrm{mod}} = 25$ mV.

It is worth highlighting that surface defects such as dislocation lines can occur during Pd growth. Dislocation lines can be observed in STM images, for example, like that between two stackings of Pd and marked by a green arrow in the inset of Fig. 6.8(a). In Figs. 6.8(b,c), this dislocation line (green arrows) indicates that the dI/dU contrast measured on a Pd film has electronic origin. Thus, the observation of dislocation lines can help to distinguish stacking from magnetism detected for Pd on Co/Ir(111).

So far, I concentrated on studying Pd films grown on top of Co islands. However, I was also interested in a transition area where Pd is attached to Co rims. Since Co grows in only one type of stacking, namely fcc, with respect to the Ir(111) substrate [116], the stacking of Pd attached to Co is most likely fcc too. To check for magnetism, I performed spectroscopic field measurements where, at every pixel of a topographic image, a single spectrum was simultaneously recorded for a bias range from $U = -1$ V to $U = 1$ V. From the spectra, I obtained dI/dU maps. Figures 6.9(a-c)and 6.10(a) show such maps

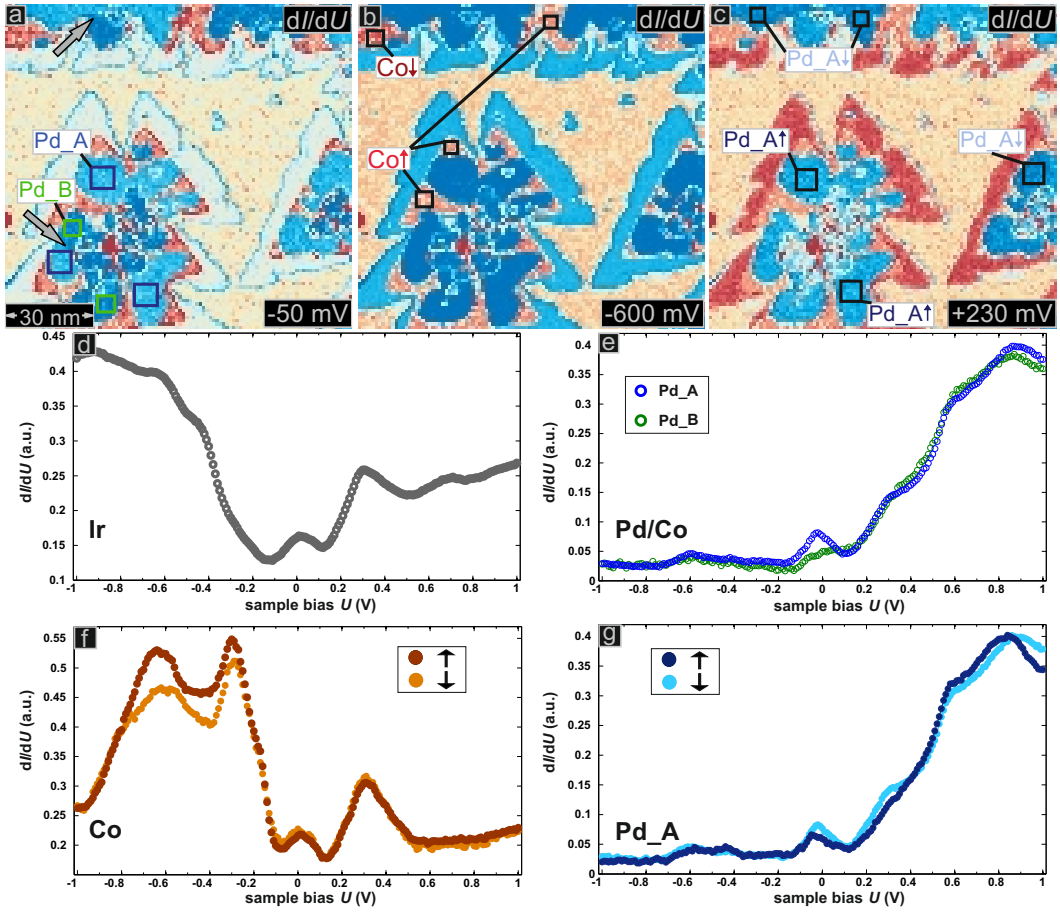

Figure 6.9: Spectroscopic field measurements:(a-c) Magnetic dI/dU maps with a lateral resolution of 1.5 nm/pixel. (d-g) Spin-resolved spectra. Arrows of (a) indicate dislocation lines between two stackings of Pd. Measurement parameters: $B = +1$ T, $I = 1.5$ nA, $U_{\mathrm{stab}} = 1$ V, $U_{\mathrm{mod}} = 30$ mV and $\tau_{\mathrm{mod}} = 3$ ms. Number of spectroscopic points is 201, total time of measurements was about 12 hours.

for different U with a spatial resolution of 1.5 nm per pixel. The spectrum of Ir(111), those of Pd/Co of both stackings and the spin-resolved spectra of Co and Pd_A are displayed in Figs. 6.9(d-g), respectively. Spectra of Pd/Ir taken at a different lateral distance from the area where Pd attached to Co↑ and Co↓ are plotted in Figs. 6.10(b) and (c), respectively. For comparison, spectra in Fig. 6.10(c) also include those shown in Fig. 6.10(b). All Pd/Ir(111) spectra exhibit a characteristic feature at $U = -300$ mV. Though there are some small spectroscopic differences, no spin-related contrast was observed for Pd/Ir(111) at $B = +1$ T and $T = 8$ K. This is, however, not surprising since SP-STS measurements on Pt(111) in proximity to Co nanostripes showed that the vacuum spin polarization decays exponentially as a function of the distance from Co with a decay length of about 1 nm at $T = 0.3$ K [127]. Thus, in this case, measurements of higher magnification images with a spatial reso-

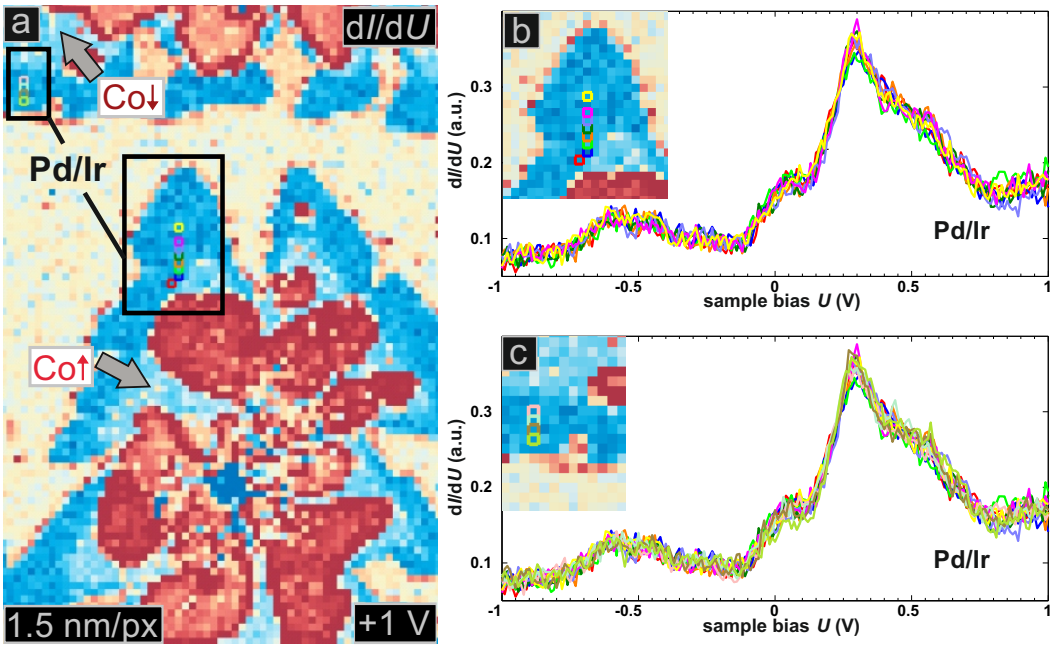

Figure 6.10: Spectroscopic field measurements of the same area shown in Fig. 6.9: (a) a magnetic dI/dU map and (b,c) spin-resolved spectra of Pd/Ir. Measurement parameters: $B = +1$ T, $I = 1.5$ nA, $U_{\mathrm{stab}} = 1$ V, $U_{\mathrm{mod}} = 30$ mV and $\tau_{\mathrm{mod}} = 3$ ms. Number of spectroscopic points is 201, total time of measurements was about 12 hours.

lution of < 1 nm per pixel and at lower temperatures (milliKelvin regime) are necessary.

In summary, I examined ML Pd on Co/Ir(111) in detail. Due to the stacking and magnetism, four dI/dU contrast levels can, in general, be observed. However, I usually measure three contrasts: two magnetic contrast levels for Pd_A and one for Pd_B. From spin-resolved spectra of Fig. 6.5, it can be clearly seen that spectroscopic differences between Pd_A↑,↓ are larger compared to those between Pd_B↑,↓, indicating that the vacuum spin-polarization differs for Pd, differently stacked, meaning that the magnetic contrast can easier be observed for Pd_A. Furthermore, a small peak at $U \approx 0$ V is usually measured for the Pd_A spectra, whereas those of Pd_B do not show any outstanding features around zero bias voltage (see also Appendix A).

To separate magnetic from electronic properties of the system studied, I use the following possibilities:
(i) An observation of dislocation lines, indicating electronic origin of a contrast.
(ii) An inversion of a tip magnetization direction, resulting in an inversion of a contrast that has a magnetic origin; domain walls are shifted.
(iii) SP-STS measurements.
I exploit these possibilities to investigate more complicated systems such as DL Pd on Co/Ir(111) and magnetic atoms adsorbed on top of Pd adlayers,

which are described in the next Sections.

6.3.2 DL Pd on Co/Ir(111)

To investigate whether I can still achieve a spin-polarized signal for a DL of Pd on Co/Ir(111), i.e. Pd_2Co, I prepared a sample as shown in Fig. 6.11(a). In this image, three buried monoatomic steps of the Ir(111) substrate can be observed. The inset of Fig. 6.11(a) schematically illustrates the surface studied: while ML Pd covers and decorates ML Co, nucleation of DL Pd on top of it also occurs. Figure 6.11(b) shows a spin-resolved $\mathrm{d}I/\mathrm{d}U$ map of the same sample area; again stacking- as well as magnetism-dependent contributions account for the $\mathrm{d}I/\mathrm{d}U$ signal. To extract the magnetic contributions only, again a field inversion measurement is performed. Fig. 6.11(c) displays a spatially-resolved magnetic asymmetry map obtained by measuring $\mathrm{d}I/\mathrm{d}U$ maps at $U = -400$ mV and at magnetic fields of $B_\uparrow = +1$ T (Fig. 6.11(b)) and $B_\downarrow = -1$ T and using Eq. 6.1. In such an asymmetry map, areas which are colored exhibit magnetic contrast while those which appear white are non-magnetic.[‡] Here, both PdCo and Pd_2Co areas are colored (for the latter cf. gray arrows), which means that the LDOS in the vacuum is spin-polarized not only above the ML Pd, but also above the DL Pd.[§] It should be noted that the absolute size of the asymmetry is similar for both ML and DL Pd, even though possibly different stackings are involved; the sign of the asymmetry is determined by the magnetization direction of the sample, i.e. if it is parallel or antiparallel to the tip magnetization at $B = +1$T.

The nature of the spin contrast achieved on ML Pd and DL Pd can in general be of two different origins: Pd is magnetic since it gets polarized by the underlying Co layer, or Pd is non-magnetic but the magnetism of the Co layer underneath the Pd is probed, like in the case of graphene/Ni(111) (see Chap. 5). While experimentally it is difficult to distinguish between the two effects the DFT calculations in the next section will clarify the origin.

6.3.3 Theory and discussion

The theoretical study has been performed by M. Hortamani using first-principles calculations based on DFT. She employed the full-potential linearized augmented plane wave method in film mode as implemented in the FLEUR code [128]. The generalized gradient approximation of Perdew, Burke and Ernzerhof was applied. The system with a slab containing 7 layers of Ir with in-plane lattice constant of 2.75 Å (corresponding to the calculated fcc lattice constant of $a_0 = 3.89$ Å) and equivalent layers on each side of the slab were modeled. The systems were relaxed including the two topmost layers of

[‡]Strictly speaking, white color in an asymmetry map means no spin contrast at a *chosen* bias voltage.

[§]Note that no spin contrast is observed for Pd-free Co films, most likely due to H_2 contamination (see Section 6.3.1). However, this does not mean that Co is not magnetic.

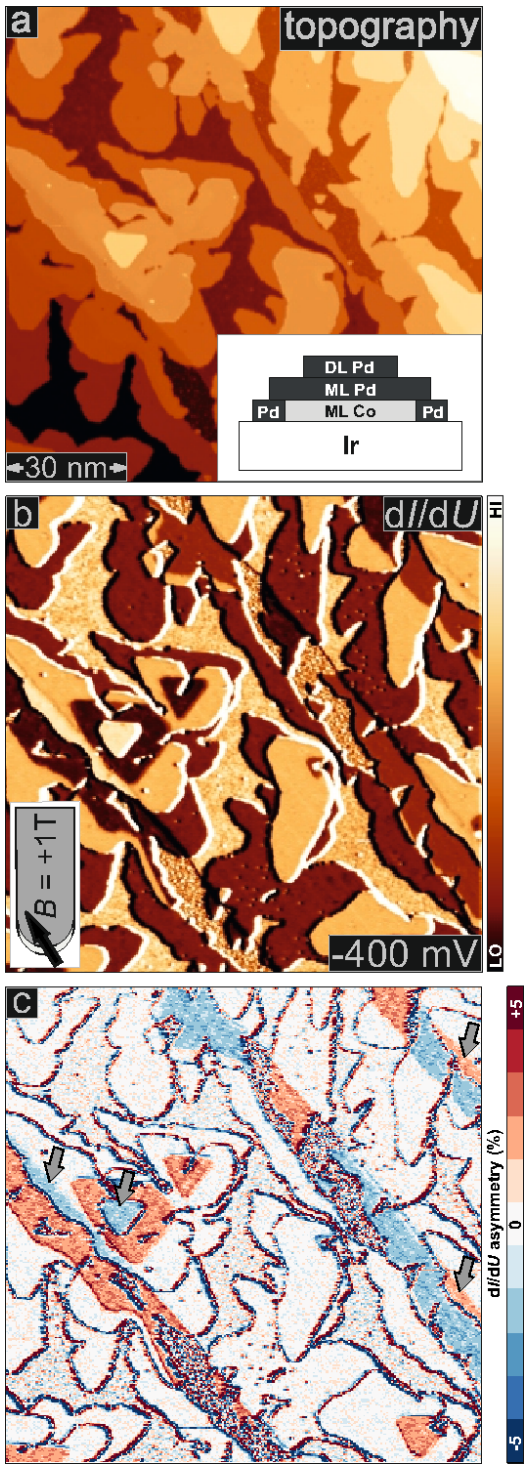

Figure 6.11: SP-STM measurements of a sample exhibiting ML Pd as well as DL Pd on Co/Ir(111): (a) Constant-current image and (b) simultaneously acquired spin-resolved $\mathrm{d}I/\mathrm{d}U$ map measured at $B = +1$ T. Color bar shows variations of the spin-polarized $\mathrm{d}I/\mathrm{d}U$ signal. (c) Spatially-resolved magnetic asymmetry map derived from spin-resolved $\mathrm{d}I/\mathrm{d}U$ maps taken at magnetic field values of $B = \pm 1$ T; DL Pd areas are indicated by gray arrows. Measurement parameters: $I = 1$ nA, $U = -400$ mV and $U_{\mathrm{mod}} = 30$ mV.

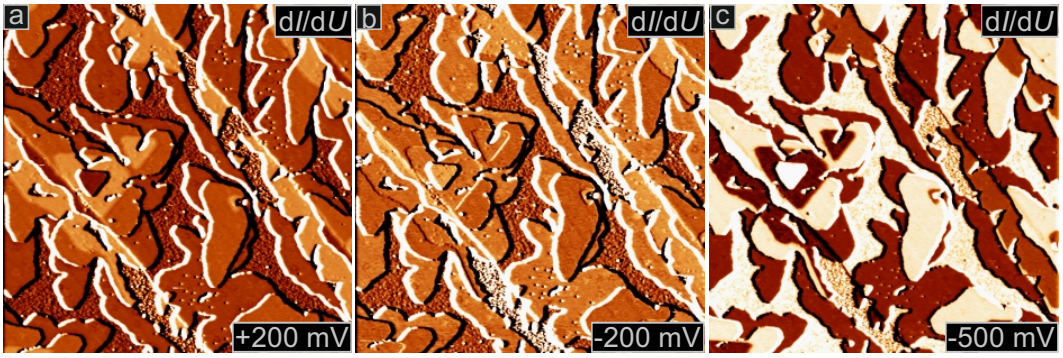

Figure 6.12: Magnetic $\mathrm{d}I/\mathrm{d}U$ maps of the same sample area shown in Fig. 6.11 but scanned at different bias voltages: (a) $U = +200$ mV, (b) $U = -200$ mV and (c) $U = -500$ mV. Measurement parameters: $B = +1$ T, $I = 1$ nA and $U_{\mathrm{mod}} = 30$ mV.

the Ir substrate in the direction of the surface normal until the atomic forces were smaller than 3×10^{-5} hrt/a.u..[¶] Muffin-tin radii of 2.4 a.u. for both Ir and Pd and 2.3 a.u. for Co atoms were chosen. Self-consistency of the calculation is reached by setting the plane wave cut-off for the basis function to $k_{\mathrm{max}} = 3.8$ a.u.$^{-1}$ and 72 $\mathrm{k}_{\parallel}$ points in the irreducible Brillouin zone.

Closed pseudomorphic layers of Co/Ir(111) and Pd_nCo/Ir(111) ($n = 1 - 2$) with different stackings were considered. Calculations found that fcc Co is energetically favored over hcp by an amount of 25 meV/atom, in agreement with the experimental observation of only one type of stacking of Co (cf. Fig. 6.1). The calculation of a row-wise AFM Co/Ir(111) layer covered with a ML Pd (both stackings fcc) yields an increase in energy of $E = 167$ meV/Co atom compared to the FM state.

			↓1% Pd	0.20
		↓6% Pd	0.31 ± 0.01	0.37
↓7%	Co	1.83 ± 0.05	1.96 ± 0.03	2.05
↓0.03%	Ir	0.21 ± 0.03	0.19 ± 0.07	0.19

Figure 6.13: Results of DFT calculations of layers of Co/Ir(111) and Pd_nCo/Ir(111) ($n = 1 - 2$): Values inside the layers indicate magnetic moments (μ_{B}/atom). Values with standard deviations are averages of different stacking combinations. For Pd_2Co/Ir(111) calculations were done for the most stable stacking, namely *fcc*. The inward relaxations for Pd, Co, and the topmost Ir layer compared to the bulk Ir inter-layer distance are shown in %.

In SP-STM experiments I observed that ML Pd grows in two stackings on Co/Ir(111) (for example, see Fig. 6.4(b)). Indeed, DFT calcula-

[¶]Here, hrt/a.u. indicates hartree energy (27.211 eV) per atomic unit (0.529177 Å).

tions show that fcc and hcp stackings of PdCo/Ir(111) are coexisting since $E_{\mathrm{fcc}} - E_{\mathrm{hcp}} \approx 2$ meV/atom. Calculations also found that the ground state of PdCo/Ir(111) is FM with magnetic moments of Co and Pd of 1.96 ± 0.03 and 0.31 ± 0.01 μ_{B}/atom, respectively; the given values are an average of the different possible stacking combinations and the small standard deviation demonstrates that the value is nearly independent of the stacking. In a Pd_2Co/Ir(111) system the magnetic moments amount to 0.20 for the top Pd layer, 0.37 for the subsurface Pd layer and 2.05 μ_{B}/atom for the Co layer (all in fcc stacking), see Fig. 6.13. These values are in good qualitative agreement with results in Ref. [113] where it was reported that the Co overlayer induces a magnetic moment of 0.33 μ_{B} and 0.24 μ_{B} in the first and second layer of the Pd substrate, respectively.

6.4 Adsorbed Co atoms

6.4.1 Co atoms on ML Pd on Co/Ir(111)

After having demonstrated that both the Pd ML and Pd DL are polarized by the underlying Co/Ir(111) system I study the properties of Co atoms adsorbed on top, using Fe-coated W tips. Figure 6.14(a) shows a representative topography of a sample where Co adatoms were deposited onto ML Pd on Co/Ir(111) at $T_{\mathrm{max}} = 20$ K to prevent diffusion. The image exhibits one buried atomic Ir(111) step going from the bottom-left to the upper-right side of the image; a ML Co wire is attached to the Ir step edge and Pd of ML height is grown on top of the Co and decorating Co rims. The individual Co atoms on Pd/Co are imaged as protrusions of about 2 Å height. The Pd film is of stacking A (Pd_A) in this case. Different stackings of Pd were observed in magnetic $\mathrm{d}I/\mathrm{d}U$ maps with a larger field of view at positive bias voltages (see Fig. 6.15(b-d)), and measured by spin-resolved spectra plotted in Fig. 6.15(e).

Figure 6.14(b) displays the topography colorized with the simultaneously acquired $\mathrm{d}I/\mathrm{d}U$ signal at $U = -500$ mV. In this sample area I find two opposite magnetization directions for Co as well as Pd/Co, separated by a domain wall (white dashed line) with a width (gray line) of $w = 1.41 \pm 0.11$ nm (see Fig. 6.14(b))[‖] which is slightly smaller compared to that shown for pure Co/Ir(111) ($w = 2.0 \pm 0.14$ nm) [116]. In the $\mathrm{d}I/\mathrm{d}U$ map at this bias voltage I also observe a different signal intensity for Co adatoms residing on the oppositely magnetized domains of Pd/Co. Indeed, by inverting the z-component of the tip magnetization direction in the external magnetic field, all contrast levels which are of magnetic origin reverse, i.e. Co/Ir(111), Pd/Co and Co adatoms on Pd/Co (cp. Figs. 6.14(b,c) measured at $B = +1$ T and $B = -1$ T, respectively). Note that the domain wall has moved by about 1.3 nm within the constriction upon field reversal as seen in Fig. 6.14(c). The magnetic contrast

[‖]The line section across the domain wall is shown in Fig. 6.16(a) and was fitted by a standard wall profile described in Chap. 5.

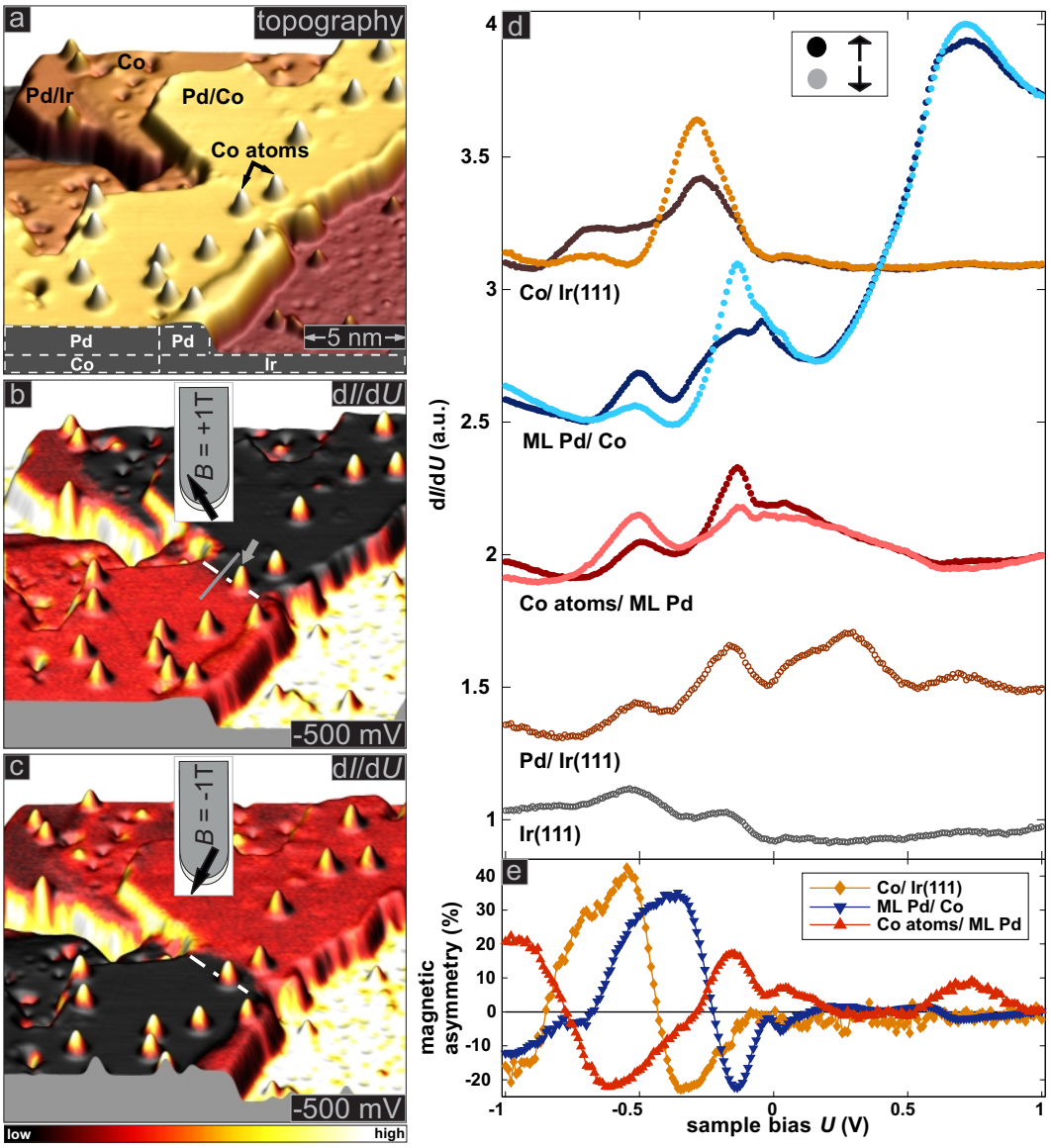

Figure 6.14: SP-STM measurements of Co atoms on ML Pd on Co/Ir(111) using a Fe-coated W tip: (a) Constant-current image measured at $B = +1$ T. (b) and (c) Constant-current images colorized with the simultaneously acquired spin-resolved $\mathrm{d}I/\mathrm{d}U$ signal measured at $B = +1$ T and $B = -1$ T, respectively; dashed white line indicates a domain wall being moved upon field reversal. Color bar shows variations of the spin-polarized $\mathrm{d}I/\mathrm{d}U$ signal. Measurement parameters: $I = 1.5$ nA, $U = -500$ mV and $U_{\mathrm{mod}} = 25$ mV. (d) Spin-polarized $\mathrm{d}I/\mathrm{d}U$ spectra ($U_{\mathrm{stab}} = -1$ V, $I_{\mathrm{stab}} = 1.5$ nA, $U_{\mathrm{mod}} = 25$ mV) measured at $B = +1$ T. Each spectrum is an average of five single spectra. All spectra except that of Ir are vertically shifted by 0.6 a.u. for clarity. (e) Magnetic asymmetries calculated for a Co monolayer, Pd/Co and Co adatoms on Pd/Co, using Eq. 6.1.

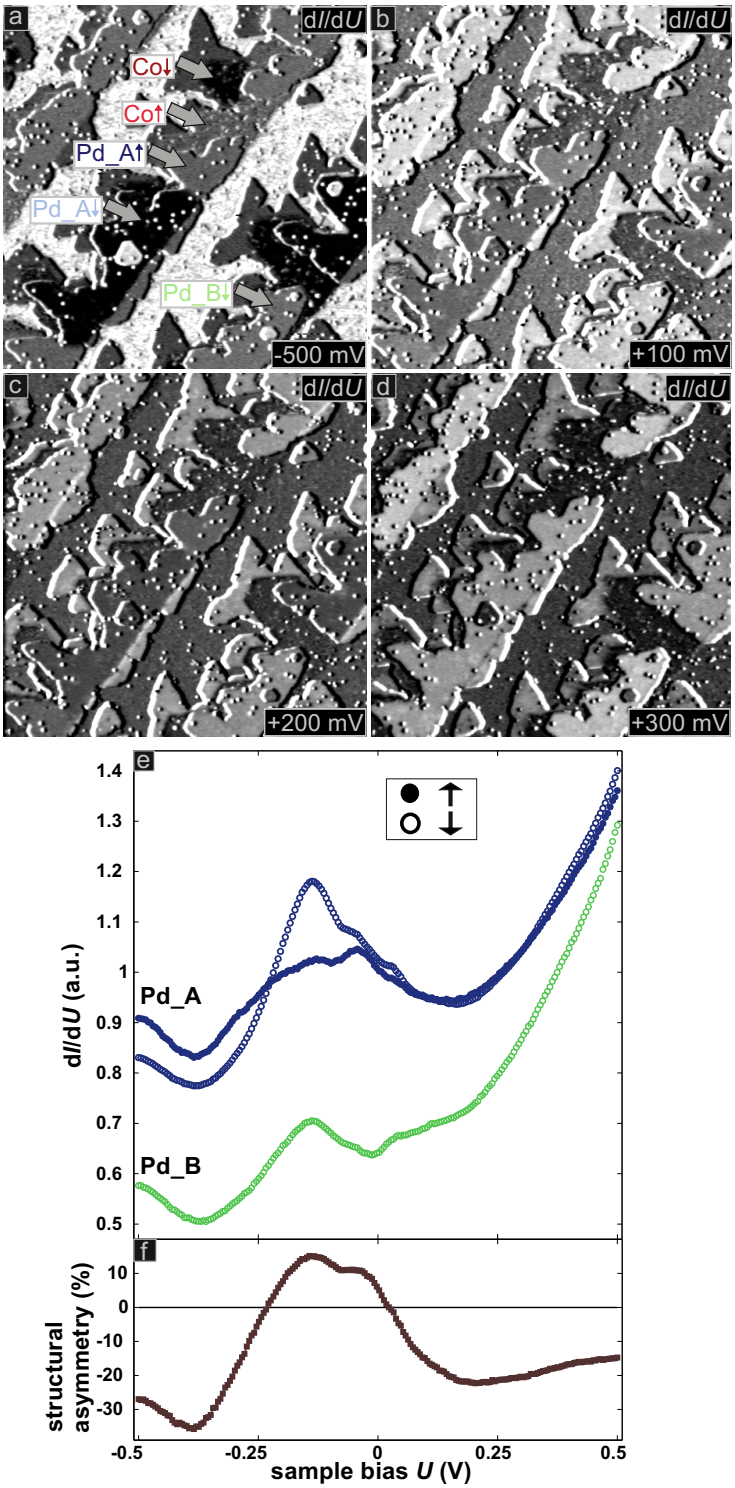

Figure 6.15: The same area of the sample, shown in Fig. B.2: (a-d) Magnetic $\mathrm{d}I/\mathrm{d}U$ maps recorded at different bias voltages. (d) Spin-resolved $\mathrm{d}I/\mathrm{d}U$ spectra of Pd of two stackings ($U_{\mathrm{stab}} = -500$ mV, $I_{\mathrm{stab}} = 1.5$ nA, $U_{\mathrm{mod}} = 30$ mV). Each spectrum is an average of five single spectra. The spectra of Pd_A are vertically shifted by multiples of 0.4 arb. units for clarity. Measurement parameters: $B = -1$ T, $I = 1.5$ nA and $U_{\mathrm{mod}} = 30$ mV.

can also be seen in spatially-resolved magnetic asymmetry maps. I derived such maps from dI/dU maps measured at $B = \pm 1$ T (see Figs. 6.17(a,b)) by evaluating Eq. 6.1. The magnetic asymmetry maps shown in Figs. 6.17(c) and (d) were obtained for different surface regions marked by solid and dashed boxes in Figs. 6.17(a,b), respectively. As a result, I find that magnetism is clearly seen for Co/Ir(111), Pd/Co and Co adatoms, while no spin contrast is observed for Pd/Ir(111), which is in agreement with a study of Pd/Ir(111) described in Section 6.3.1.

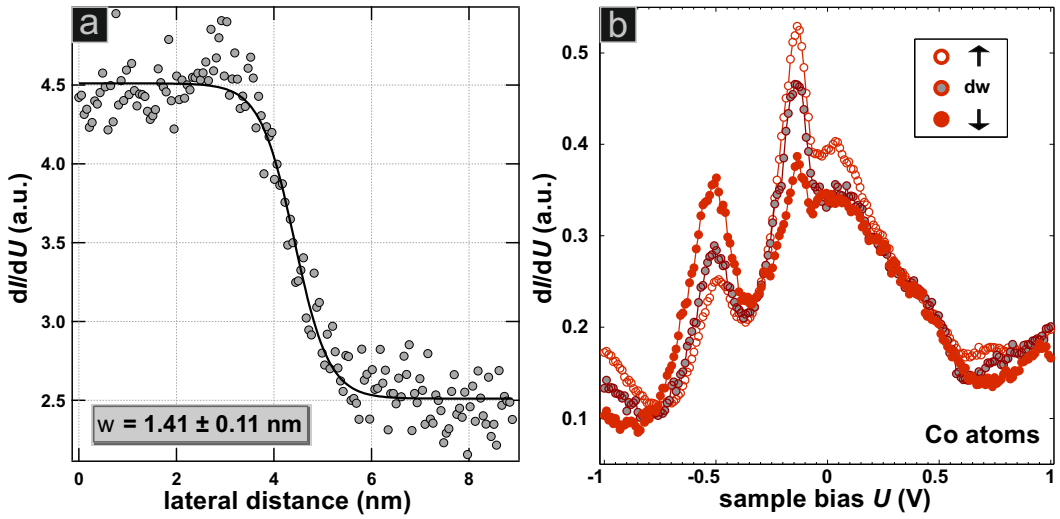

Figure 6.16: (a) A line profile across the domain wall marked by a gray line in Fig. 6.14(b). Gray circles and a black line represent experimental data and a fitted profile, respectively. (b) SP-STS of Co atoms residing on oppositely magnetized domains of a Pd/Co wire (open and closed circles), and of that sitting on a domain wall (gray-filled circles) (see Fig. 6.14(b)). Measurement parameters: $I = 1.5$ nA, $U_{\mathrm{stab}} = -1$ V and $U_{\mathrm{mod}} = 30$ mV.

To investigate the spin- and energy-resolved electronic structure of Co atoms on ML Pd on Co/Ir(111), I performed SP-STS measurements. Spectroscopic data obtained at $B = +1$ T for adatoms and substrate shown in Fig. 6.14(b) is plotted in Fig. 6.14(d).** Spin-polarized dI/dU spectra of Co/Ir(111) with a pronounced resonance at $U = -270$ mV were used as a reference to calibrate the magnetic tip. I observe that this resonance is followed by another feature at $U \approx -650$ mV, which can be attributed to a tip state since it is often measured with different tips and varied significantly in shape and intensity [129]. Spin-resolved spectra of Pd/Co were recorded over defect free areas of the film, and show a sharp peak at $U = -140$ mV which is also followed by a tip feature at $U \approx -500$ mV. Since the peak at $U = -140$ mV (and that at $U \approx -500$ mV) appears in spectra of Ir(111) and Pd/Ir(111), and was not observed for different samples (see Section 6.3.1), I

**Spin-resolved spectra measured at different U_{stab} can be found in Appendix B.

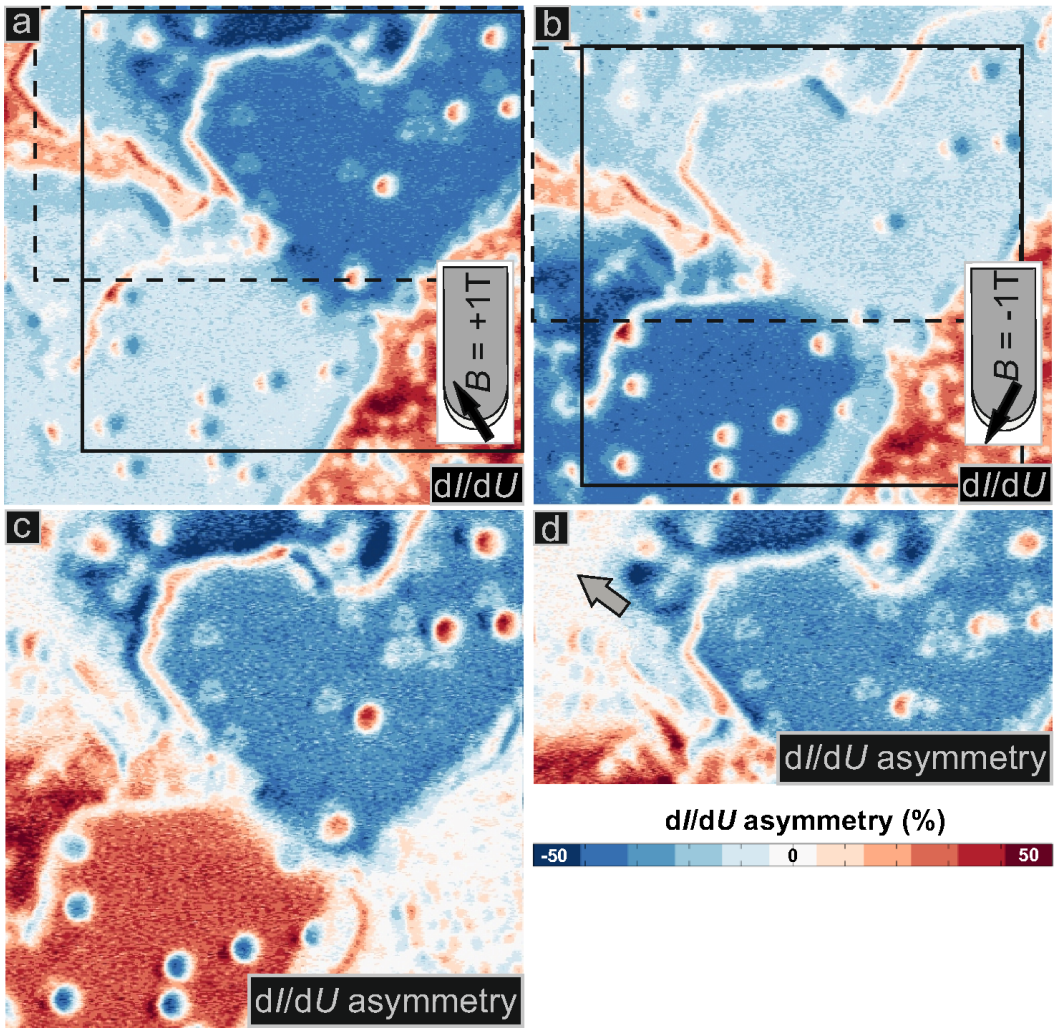

Figure 6.17: (a) and (b) Spin-resolved dI/dU maps of the same surface area as in Fig. 6.14 taken at $B = +1$ T and $B = -1$ T, respectively. (c) and (d) Spatially-resolved magnetic asymmetry maps derived from dI/dU maps for different surface regions which are marked by solid and dashed boxes, respectively. While magnetic signals are clearly seen for Co, Pd/Co films and Co adatoms in (c), no spin-related contrast is observed for Pd/Ir(111) in (d) (see arrow). Measurement parameters: $I = 1.5$ nA, $U = -500$ mV and $U_{\mathrm{mod}} = 30$ mV.

attribute it to a tip state as well. Furthermore, spectra of Pd/Co show a resonance at $U = +700$ mV, whereas those of Co/Ir(111) are relatively flat and do not show any spectroscopic differences at positive bias voltages. Thus, the observed feature appears to be characteristic for Pd/Co.

Spin-resolved spectra of Co atoms were acquired by positioning the tip over the center of protrusions, and averaging over five different spectra which were obtained for adatoms residing on the same Pd/Co domain. Single adatoms can occupy fcc and hcp three-fold hollow sites on a substrate. However, no intensity

difference was observed in spectra of Co adatoms sitting on a Pd/Co domain of a given magnetization direction. This suggests that there is a preferential adsorption site, i.e. only one type of three-fold hollow sites is occupied. Also, care was taken to record spectra on atomic protrusions adsorbed on the center of Pd/Co to prevent an influence of the local environment, such as a different lateral distance from the island edge. Interestingly, spin-resolved data obtained for a Co adatom residing on the domain wall (see a gray arrow in Fig. 6.14(b)) lies between those of Co atoms residing on different domains, over the whole bias range studied from $U = -1$ V to $U = +1$ V, as seen in Fig. 6.16(b).

I observed that the spin-polarized spectra of Co atoms show intense peaks at $U = -140$ mV and $U = -500$ mV. Similar to the Pd/Co spectra, these peaks are due to the tip states. Furthermore, the spectra of Co adatoms also show a spin-polarized resonance at $U = +700$ mV which is similar to that found for Pd/Co at the same bias voltage but is absent for spectra of Co/Ir(111). The fact that spectra of Co adatoms inherit a characteristic feature of those of Pd/Co indicates that the magnetic coupling between adatoms and a Co monolayer is mediated via Pd, as will be shown by our DFT calculations in Section 6.4.3.

Important information about the system studied can be obtained from magnetic asymmetries calculated from spin-resolved spectra. Magnetic asymmetries calculated for Co/Ir(111), Pd/Co and Co adatoms using Eq. 6.1 are plotted in Fig. 6.14(e). I find an *inversion* of the magnetic asymmetry of Co atoms with respect to that of ML Pd over the whole bias range studied from $U = -1$ V to $U = +1$ V. The inversion is independent of U_{stab} and observed for a different sample measured with a different magnetic tip (see figures in Appendix B).

The following mechanisms are suggested to be responsible for the observed phenomenon:
(i) In the tunneling process, the spin character of adatom orbitals is opposite to that of the substrate. L. Zhou and co-workers have recently showed that the spin polarization[††] at E_{F} above Co adatoms is reversed with respect to that of the Co layer [7]. The authors attributed their observation to *sp* electrons, whose spin polarization is opposite to that of *d* electrons due to the hybridization. Since the *d* electrons decay faster, the *sp* electrons contribute most strongly to the spin polarization in the vacuum above adatoms [7; 130; 14].
(ii) Adatoms are coupled antiferromagnetically to the magnetic substrate underneath. As it was reported by Y. Yayon and co-authors, a reversed sign of the spin polarization of Cr adatoms with respect to that of Co/Cu(111) implies an AFM coupling between Cr adatoms and a Co island [9].[‡‡]
However, our DFT calculations in Section 6.4.3 predict a FM coupling of Co atoms to a Co layer across ML Pd. Thus, the inversion is likely a particular

[††]A magnetic asymmetry A_{mag} can be linked to the spin polarization of the sample P_{s} via $A_{\mathrm{mag}} = P_{\mathrm{t}} P_{\mathrm{s}}$, where P_{t} is the spin polarization of the tip.
[‡‡]A change in sign of the spin polarization of Co atoms with respect to Co/Cu(111) was, however, attributed to a FM coupling of adatoms in Ref. [13].

property of single adatoms on atomically flat surfaces, as it was pointed out by L. Zhou *et al.* in Ref. [7].

6.4.2 Co atoms on DL Pd and ML Pd on Co/Ir(111)

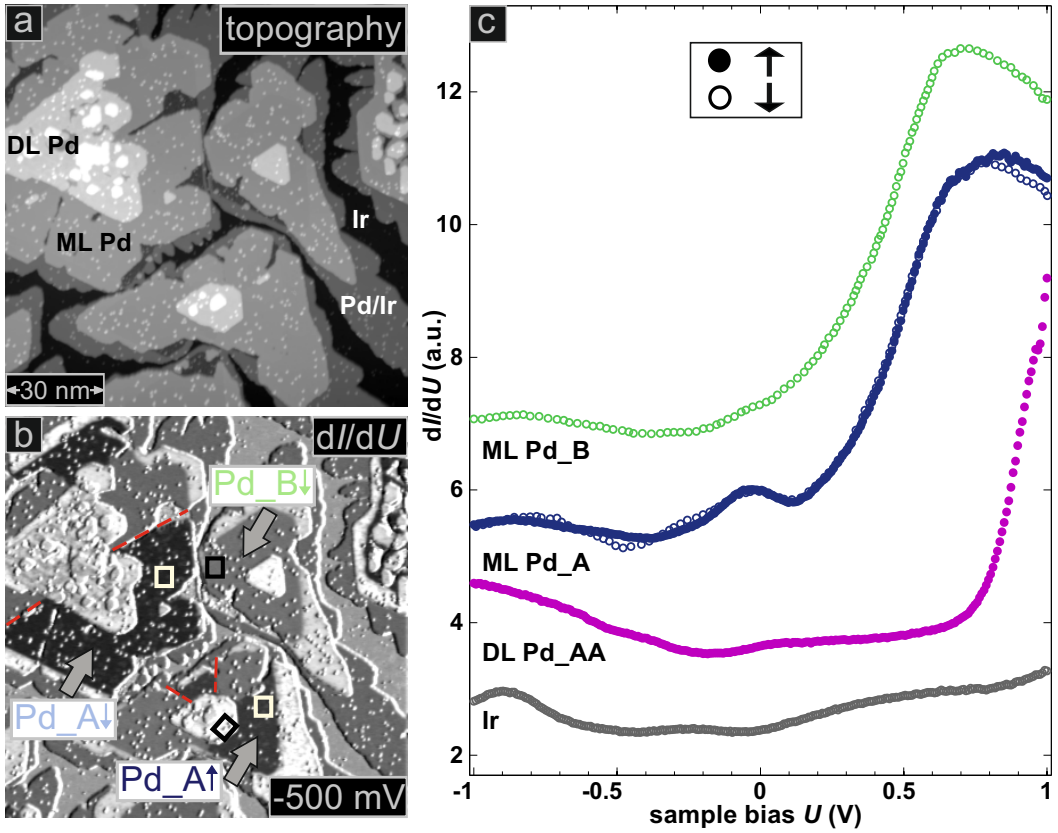

Figure 6.18: SP-STM measurements of DL Pd and ML Pd on Co/Ir(111), with Co atoms adsorbed on top: (a) Constant-current image and (b) simultaneously acquired spin-polarized dI/dU. (c) Spin-resolved dI/dU spectra of ML Pd of two stackings, DL Pd on ML Pd of stacking A (DL Pd_AA), and the spectrum of Ir(111) ($U_{\mathrm{stab}} = -1$ V, $I_{\mathrm{stab}} = 1$ nA, $U_{\mathrm{mod}} = 30$ mV). Boxes highlight regions where spectra of ML and DL Pd were taken. Each spectrum is an average of five single spectra. All spectra except that of Pd/Ir are vertically shifted by multiples of 2 arb. units for clarity. Dashed lines in (b) indicate dislocations between two stackings of ML Pd. Measurement parameters: $B = +1$ T, $I = 1$ nA, $U = -500$ mV and $U_{\mathrm{mod}} = 30$ mV.

To investigate the evolution of the spin- and energy-resolved electronic structure of Co atoms with Pd spacer thickness, me and C. Hanneken performed SP-STS measurements of adatoms on ML and DL Pd on Co/Ir(111) using Fe-coated W tips. Figures 6.18(a) and 6.19(a) show topographies of such a sample. The spectra of ML Pd and DL Pd were recorded on defect free areas, as indicated by boxes and crosses in Fig. 6.18(b) and Fig. 6.19(a), respectively.

Though there are, in general, two possible stackings of DL on ML Pd, I measured DL Pd on ML Pd of stacking A only. I assign the observed films of DL Pd to Pd_AA (see Fig. 6.18(c)). The spectroscopic data measured on Co atoms on ML and DL Pd at $B = \pm 2$ T are shown in Fig. 6.19(b). The spectra were acquired by positioning the tip over the center of each adatom protrusion. All displayed plots are an average over five spectra.

Spectra of ML and DL Pd as well as that of Pd/Ir(111) in Fig. 6.19(b) are in qualitative agreement with results obtained for different samples (see Fig. 6.18(c), Fig. 6.14(d) and Appendixes A and B). Spectra of ML Pd show a characteristic peak around $U = +650 - +700$ mV, while that of DL Pd does not exhibit any outstanding features over the bias range studied from $U = -1$ V to $U = +1$ V. Since the same Co atoms and also positions on Pd_nCo were measured at $B = +2$ T and $B = -2$ T, the electronic features related to differences in the local environment such as different stacking and different lateral distances to the island edge, are the same for the spectra shown in Fig. 6.19(b). Therefore the observed spectroscopic differences on the Co adatoms and the Pd layers are purely magnetic in origin.

The spin-resolved spectra of ML Pd and Co atom/ML Pd in Fig. 6.19(b) are, however, in quantitative disagreement with those shown in Fig. 6.14(d). Spectra do not exhibit crossing points at $U = -230$ mV and $U = -670$ mV ($U = -290$ mV and $U = -760$ mV), and pronounced peaks at $U = -140$ mV and $U = -500$ mV ($U = -140$ mV and $U = -500$ mV) observed for the ML Pd (Co atom/ML Pd) in Fig. 6.14(d). The peaks were, however, attributed to the tip states (see Section 6.4.1), which might also cause the spin-resolved spectra crossing.

Magnetic atoms deposited on a metallic surface can show Kondo-type physics which is usually detected as a Fano resonance at E_F in an experimental STM spectrum, below a characteristic temperature known as the Kondo temperature [131]. In case of spectra of Co adatoms on ML and DL Pd in Fig. 6.19(b), peaks around zero bias are not split in an external magnetic field [132; 133], and their widths of about 200 mV for Co atom/ML Pd and 100 mV for Co atom/DL Pd are much larger than one should expect for a Kondo system [131; 133]. These observations suggest that either the magnetic coupling between Co adatoms and the Co layer underneath is much stronger than the Kondo effect, therefore the latter is suppressed; or the Kondo temperature is lower compared to the measurement temperature of $T = 8$ K. Similar to experimental results in Ref. [6] and theoretical investigations in Refs. [134; 135], the observed spectroscopic features can be interpreted in terms of strong correlation effects which can be solved by using a many body Anderson-type Hamiltonian.

Magnetic asymmetries of the spin-polarized spectra were calculated using Eq. 6.1 and are plotted in Fig. 6.19(c). C. Hanneken finds that the Co adatoms on both ML and DL Pd show a similar energy-dependent asymmetry over the whole bias range studied from $U = -1$ V to $U = +1$ V (the same trend can be seen for the Pd layers as well). This means that the spin-polarized

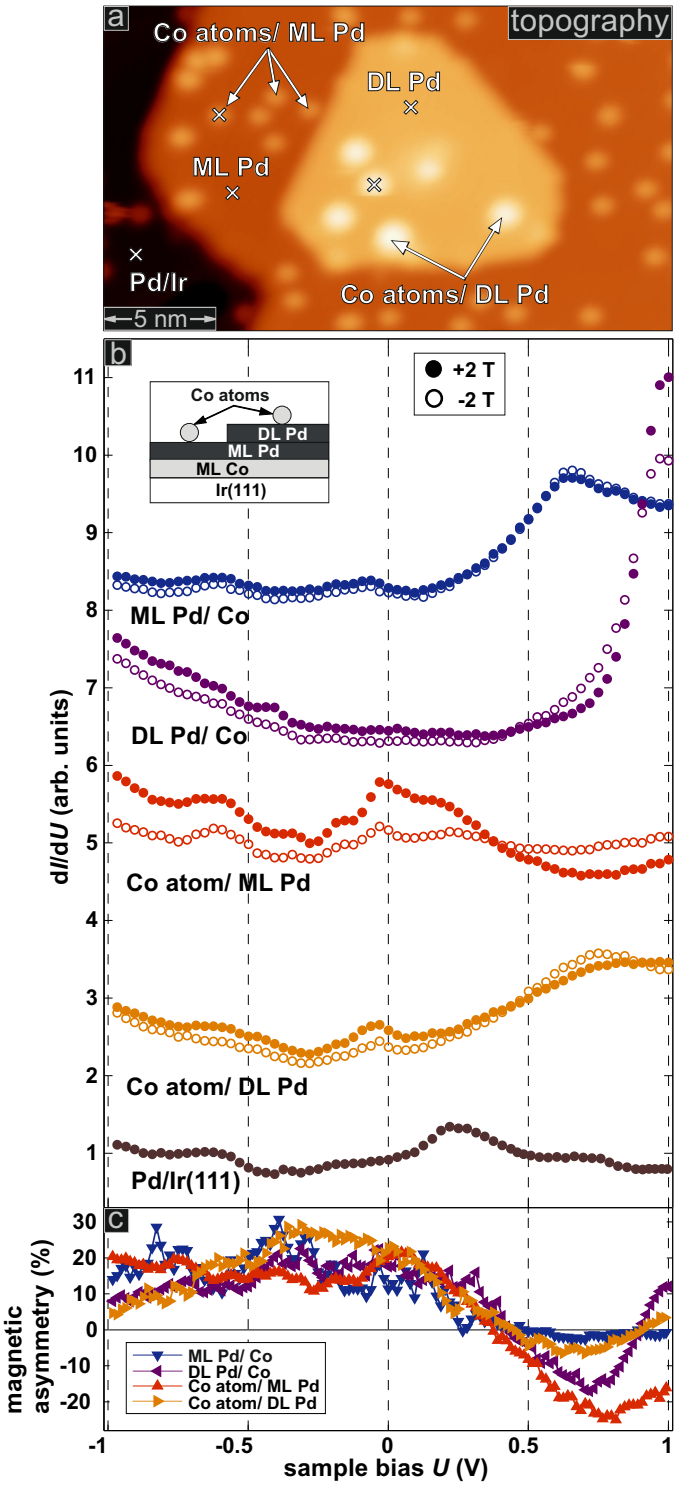

Figure 6.19: SP-STM measurements of Co atoms on DL Pd as well as on ML Pd on Co/Ir(111) using a Fe-coated W tip: (a) Constant-current image measured at $B = +2$ T. (b) Spin-polarized $\mathrm{d}I/\mathrm{d}U$ spectra ($U_{\mathrm{stab}} = +1$ V, $I_{\mathrm{stab}} = 1$ nA, $U_{\mathrm{mod}} = 30$ mV) measured at $B = \pm 2$ T at locations marked by crosses in (a). Each spectrum is an average of five single spectra. All spectra except that of Pd/Ir are vertically shifted by multiples of 2 arb. units for clarity. (c) Magnetic asymmetries calculated for the spin-resolved spectra. Measurements were done by C. Hanneken.

LDOS measured in vacuum above the Co adatoms (and Pd layers) does not change significantly with increasing Pd spacer thickness from ML to DL. This observation indicates the same nature of the magnetic properties of Co adatoms on ML and DL Pd. However, C. Hanneken does not observe the magnetic asymmetry inversion for Co atoms on ML Pd, as it was shown in Section 6.4.1. Though this might mean that different sample states of opposite spin character compared to that measured in Fig. 6.14(d) were involved into the tunneling process, the explanation of these observations remains an open question.

6.4.3 Theory and discussion

To investigate the coupling of Co adsorbed on the polarized Pd layers on Co/Ir(111) M. Hortamani first considered fully closed Co layers on $Pd_nCo/Ir(111)$ ($n = 1 - 3$) with different stackings. In addition to the fully closed Co ML on PdCo/Ir(111), she also calculated a (2×2) Co atom superstructure on top of PdCo/Ir(111). A larger Pd spacer thickness was not considered for the (2×2) Co atom superstructure calculations due to the tremendous increase in computation time, and lack of experimental data for ($n > 2$). The exchange energy of the system is calculated as the difference between the total energies of fully self-consistent FM and AFM configurations.

DFT calculations show that, regardless of the stacking, Co adlayers on ML, DL, and also three layers of Pd carry a magnetic moment of about 2.04 μ_B/atom, with a magnetic moment of Pd of $0.29 - 0.35$ μ_B/atom, except for the middle of the Pd trilayer (see Fig. 6.20). The values are in good qualitative agreement with results in Ref. [136] where it was reported that the magnetic moments of Co layers are $2.08 - 2.18$ μ_B/atom with magnetic moments of ML and DL Pd of $0.19 - 0.30$ μ_B/atom. However, it was found that the calculated values of the exchange energy between the top Co layer and the Co/Ir(111) layer strongly decrease (see Fig. 6.20). While the Co layers align ferromagnetically for both the ML as well as the DL Pd spacer, the size of the coupling is reduced by a factor of three with increasing Pd thickness; the coupling across the Pd trilayer is almost zero (see Fig. 6.20).

This finding of a reduced coupling having the same sign for ML and DL spacer is in contrast to the calculation in Ref. [26] for single Co atoms coupled through a Cu spacer to Co/Cu(111). They find that the coupling is oscillatory (changing sign) and mediated by conduction electrons of the spacer. The electrons scattered from the Co layer form spin-polarized interference patterns inside the spacer due to quantum confinement [25; 26]. These patterns vary with the spacer thickness, which causes the coupling of adatoms to oscillate between FM and AFM coupling, i.e. from parallel alignment for a ML Cu spacer to antialignment for a DL Cu spacer. The crucial difference to the system studied in my thesis is that the Pd layers carry a magnetic moment. This has a dramatic effect on the spacer thickness dependence of the interlayer exchange coupling, as also shown in the previous study of a $Fe/Pd_n/Fe$ layer system [29]: by varying the Pd spacer thickness they found that the oscillatory

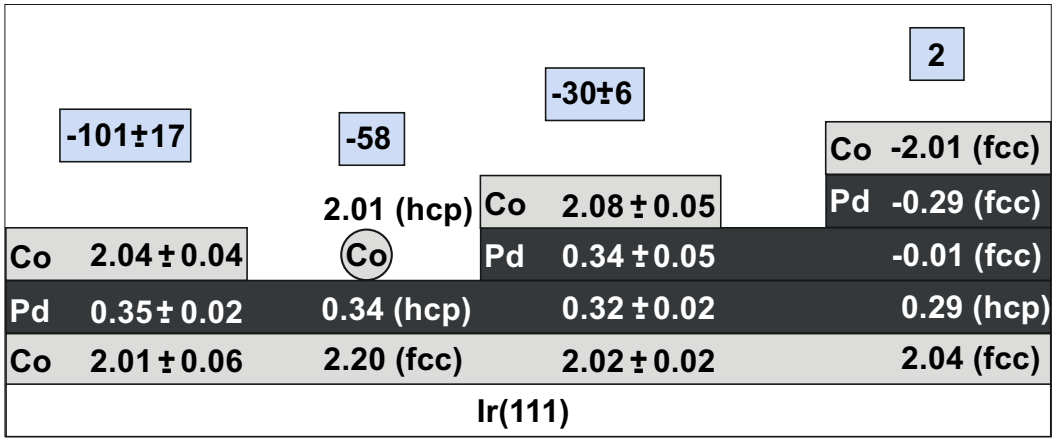

Figure 6.20: Results of DFT calculations of layers of $CoPd_nCo/Ir(111)$ ($n = 1-3$) and a (2×2) Co atom superstructure on PdCo/Ir(111): Values inside of each layer and over the atom are magnetic moments (μ_B/atom) averaged over different stacking combinations with standard deviation, or calculated for the most stable stackings (noted). Numbers in blue boxes are exchange energies (meV/atom) of Co overlayers or of a single Co atom coupled to an underlying Co layer across a Pd spacer.

behavior of the coupling between the magnetic layers is superimposed on the exponentially decreasing FM contribution. In their study this leads to an overcompensation of the AFM part of the oscillatory coupling for $n \leq 12$ ML of Pd spacer. Furthermore, the FM coupling of Co layers through ML and DL Pd was reported in the theoretical study in Ref. [136] supported by experimental results in Refs. [114; 115].

Coming back to the system studied here I suggest that the FM coupling via both the ML and DL Pd can be attributed to an additional FM contribution to the coupling which is due to the induced magnetic moments of the Pd spacer. To obtain values for the coupling close to the experiment, M. Hortamani also considered a (2×2) superstructure of Co atoms on a PdCo/Ir(111) system (cf. Fig. 6.20). Again the coupling between the Co structures is FM, but compared to the layered system it is reduced from about -100 to -58 meV/top Co atom. If we consider the trend found for the closed Co layers, i.e a decrease of the coupling via ML to DL Pd by a factor of three, we estimate a coupling of single Co atoms to the Co/Ir(111) through a Pd DL on the order of -17 meV/top Co atom. This also suggests a strong FM coupling, in line with the similar behavior of magnetic asymmetries of Co atoms on ML and DL Pd obtained in SP-STM experiments (see Section 6.4).

6.5 Summary

In this chapter, the system of Pd adlayers on Co/Ir(111) and Co atoms adsorbed on top have been examined. While for Co on Ir(111) only one type

of stacking is present, I observe two stackings of ML Pd on Co islands, in agreement with DFT calculations. The measured spin-polarized $\mathrm{d}I/\mathrm{d}U$ contrast on ML and DL Pd indicates that Pd-capped Co islands are single domain ferromagnetic with the easy magnetization axis normal to the surface. Spin contrast is also achieved on Co adatoms on ML and DL Pd. I observe an inversion of the magnetic asymmetry of Co adatoms with respect to that of ML Pd, which is attributed to the opposite spin character of adatoms and substrate orbitals contributing to the tunneling current. Magnetic asymmetries of the measured spin-polarized spectra of Co atoms on Pd ML and DL show a similar energy-dependent behavior over the whole bias range studied from $U = -1$ V to $U = +1$ V. Based on DFT calculations, Pd atoms are found to carry a magnetic moment on the order of $0.2 - 0.4\ \mu_\mathrm{B}$/atom. Calculations also predict that the coupling between Co structures through ML and DL Pd is ferromagnetic, which is supported by the spin-resolved STM measurements. Theory finds a reduction by a factor of three from a ML to DL Pd spacer, while it is close to zero for a spacer of three Pd layers.

Chapter 7

Summary and perspectives

In this work, individual magnetic atoms adsorbed on top of surfaces of non-magnetic materials on magnetic substrates are investigated. In particular, the systems are graphene on Ni(111), Pd adlayers on Co/Ir(111) and single adatoms are studied from both experimental and theoretical side.

The magnetism of the bare and graphene-capped Ni(111) is explored by SP-STM, SEMPA, and Kerr microscopy, covering length scales from the nanometer regime up to several millimeters. It is shown that domain walls with widths of 60 - 90 nm can be observed and moved by small perpendicular magnetic fields at $T = 8$ K. A stripe like domain pattern with stripe widths of 3 - 6 μm and a second type of modulation within stripes with widths of about 330 nm are found at room temperature. A single domain state is achieved at 140 mT. In agreement with DFT calculations, an enhanced atomic corrugation with respect to the bare surface is observed. The calculations also predict an inversion of the spin polarization with respect to the pristine Ni(111) as a result of the quenching of Ni surface states. Single atoms such as Fe, Co and Cr can be prepared on top of graphene/Ni(111) by low temperature deposition, imaged without inducing diffusion at large tip-sample distances and studied by means of STS. However, the systems were difficult to investigate due to residual contamination of Ni(111) and a fully-closed monolayer growth of graphene. When the substrate is clean and island growth of graphene is achieved, this is a promising sample system to study the magnetic interaction through graphene, and the predicted inversion of the spin polarization.

Pd adlayers on Co/Ir(111) are found to be a perfect substrate to study properties of single Co adatoms adsorbed on top. With SP-STM and SP-STS, the morphology and the spin-resolved electronic properties of ML and DL Pd on Co/Ir(111) are investigated, pseudomorphic growth with two stackings of ML Pd is observed, and spin contrast on both the Pd adlayers and on Co adatoms is achieved. Similar to theoretical predictions for graphene/Ni(111),

an inversion of spin polarization of Co adatoms with respect to that of ML Pd is observed experimentally in the vacuum region over the whole bias range studied from -1 V to +1 V. This observation is attributed to the opposite sign of spin states of adatoms compared to that of the substrate. A similar behavior of magnetic asymmetries obtained for spin-resolved spectra of Co atoms on ML and DL Pd indicates that the magnetic properties of adatoms do not change significantly with increasing Pd spacer thickness. In fact, DFT calculations predict that the magnetic moments for ML and DL Pd are about 0.3 μ_B/atom and 0.2 μ_B/atom, respectively; Co layers adsorbed on top of Pd films possess a magnetic moment of about 2.0 μ_B/atom. The calculations also show that Co adlayers are ferromagnetically coupled to the Co/Ir(111) underneath. The size of the magnetic exchange coupling is reduced by a factor of three going from ML to DL Pd spacer between the Co layers. The FM coupling between Co structures is attributed to Pd magnetic moments induced by the underlaying magnetic substrate.

Based on the results obtained in my PhD thesis, I find the following projects to be promising for future research:

(i) h-BN on Ni(111) or Co/Ir(111): The crystallographic and electronic band structure of h-BN are similar to those of graphene [72]. However, due to the symmetry breaking between the sublattices (one sublattice consists of B atoms, another of N), a band gap of a few electronvolts is opened. This means that h-BN is an insulator. It has been recently shown that h-BN perfectly grows on Ni(111), forming 1 ML high triangular islands on open terraces [137]. At such a sub-monolayer regime, it should be possible to experimentally observe an inversion of the spin polarization above h-BN/Ni(111) compared to the pristine surface, as it was predicted theoretically for graphene/Ni(111). Furthermore, since the preparation of h-BN is the same as that of graphene, h-BN can also grow on Ir(111), thereby be intercalated by Co, as it was shown for graphene-intercalated Co on Ir(111) [15]. H-BN on Ni(111) or Co/Ir(111) can, therefore, serve as an ideal template to electronically and magnetically decouple single atoms adsorbed on top from a magnetic substrate underneath.

(ii) H-terminated graphene nanoribbons (GNRs) on Au(111): *Ab initio* calculations in Ref. [138] predict that zigzag GNRs deposited on Cu(111), Ag(111) and Au(111) all possess edge states but do not exhibit significant edge magnetism, with the exception of H-terminated GNRs on Au(111), whose zero-temperature magnetization is comparable to that of free-standing GNRs. These results are explained by the different interaction and charge transfer between the GNRs and the substrates. Only in the case of H-terminated GNRs on Au(111), the interaction is sufficiently weak not to affect the electronic and magnetic properties of the edge states significantly. This suggests that experimental investigations on edge magnetism in GNRs deposited on metallic substrates should focus on that particular system.

(iii) Ag on Co/Ir(111): Due to the strong $3d$-$4d$ hybridization, overlayers of Mn, Fe, Co and Ni induce sizable magnetic moments in the two upper most layers of a Pd substrate [113]. For a Ag substrate this effect is, however, found

to be of minor importance since the $4d$ electrons are strongly localized and the in-plane $3d$-$3d$ and the $5sp$ hybridization are more important [113]. Thus, Ag is essentially non-magnetic. A spacer of Ag (or another noble metal) can be considered as good experimental realization to separate magnetically adatoms from an underlaying Co/Ir(111) substrate.

(iv) V on Ag(001): Bulk V is non-magnetic. However, there is a theoretical prediction that a ML of V on Ag(001) is antiferromagnetic with a magnetic moment of about 2.0 μ_B/atom [113]. Though the ferromagnetic order of 1-7 ML V/Ag(100) and the weak antiferromagnetism of 1-16 ML of V on Au films have been observed experimentally [139; 140], there is lack of measurements for similar systems with SP-STM.

Appendix A

Figures of ML Pd on Co/Ir(111)

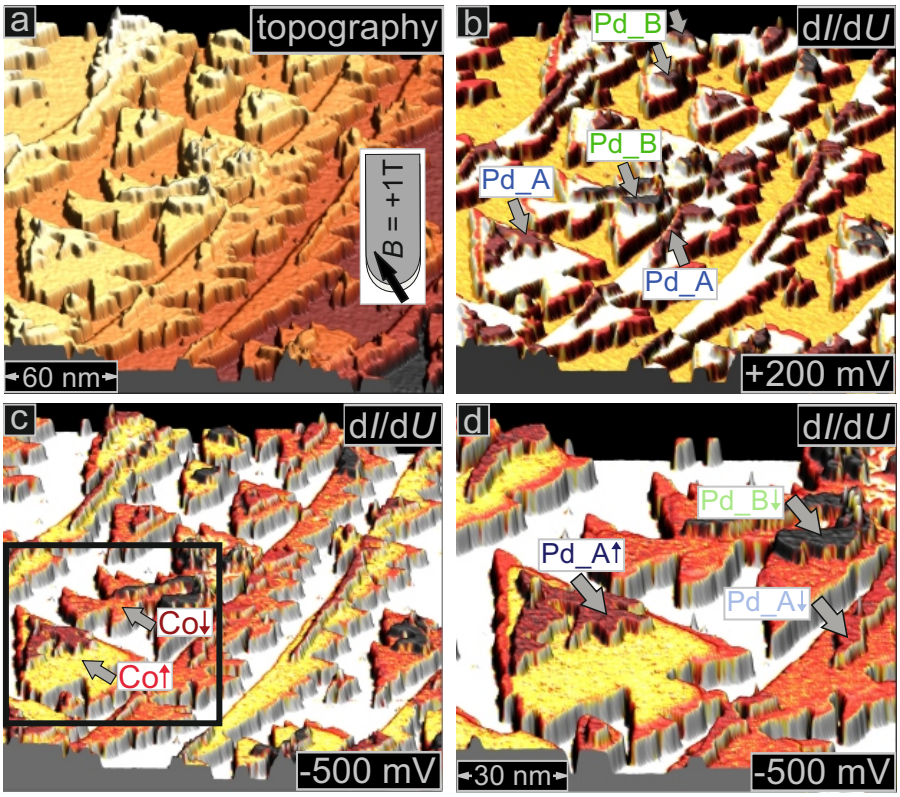

Figure A.1: SP-STM measurements of ML Pd on Co/Ir(111) using a Fe-coated W tip: (a) Constant-current image and (b-d) simultaneously acquired spin-resolved $\mathrm{d}I/\mathrm{d}U$ maps. Measurement parameters: $B = +1$ T, $I = 1.0$ nA and $U_{\mathrm{mod}} = 30$ mV.

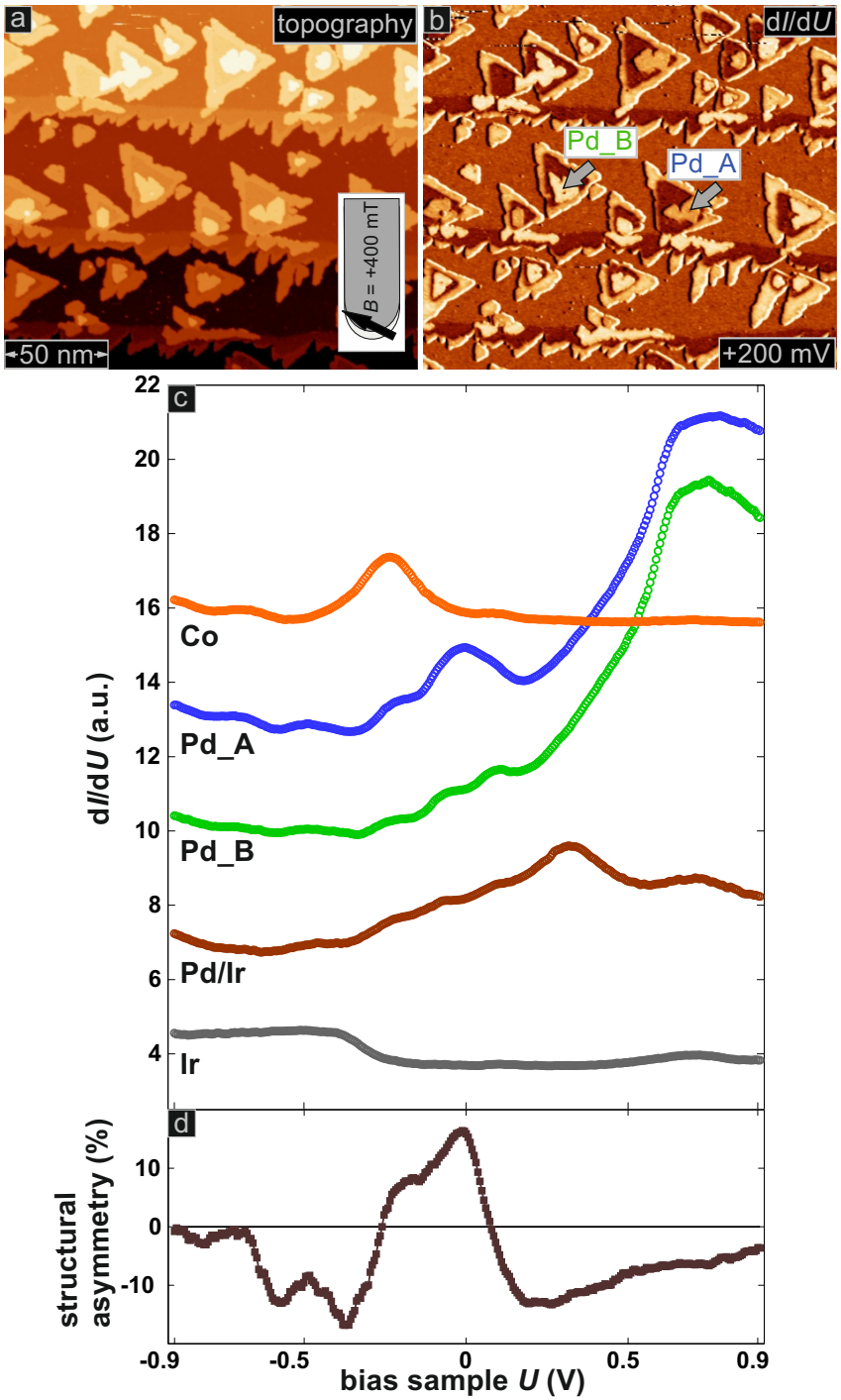

Figure A.2: SP-STM measurements of ML Pd on Co/Ir(111) using a Fe-coated W tip: (a) Constant-current image and (b) a simultaneously acquired $\mathrm{d}I/\mathrm{d}U$ map. Measurement parameters: $B = +400$ mT, $I = 1.5$ nA, $U = +200$ mV and $U_{\mathrm{mod}} = 30$ mV. (c) $\mathrm{d}I/\mathrm{d}U$ spectra of the sample: $U_{\mathrm{stab}} = -0.9$ V, $I_{\mathrm{stab}} = 1.5$ nA, $U_{\mathrm{mod}} = 30$ mV. Each spectrum displayed is an average of 5 single spectra. Spectra of Co, Pd of different stackings (Pd_A and Pd_B) and Pd/Ir are shifted vertically by multiples of 2 arb. units for clarity. (d) Structural asymmetry calculated for spectra of Pd of different stackings.

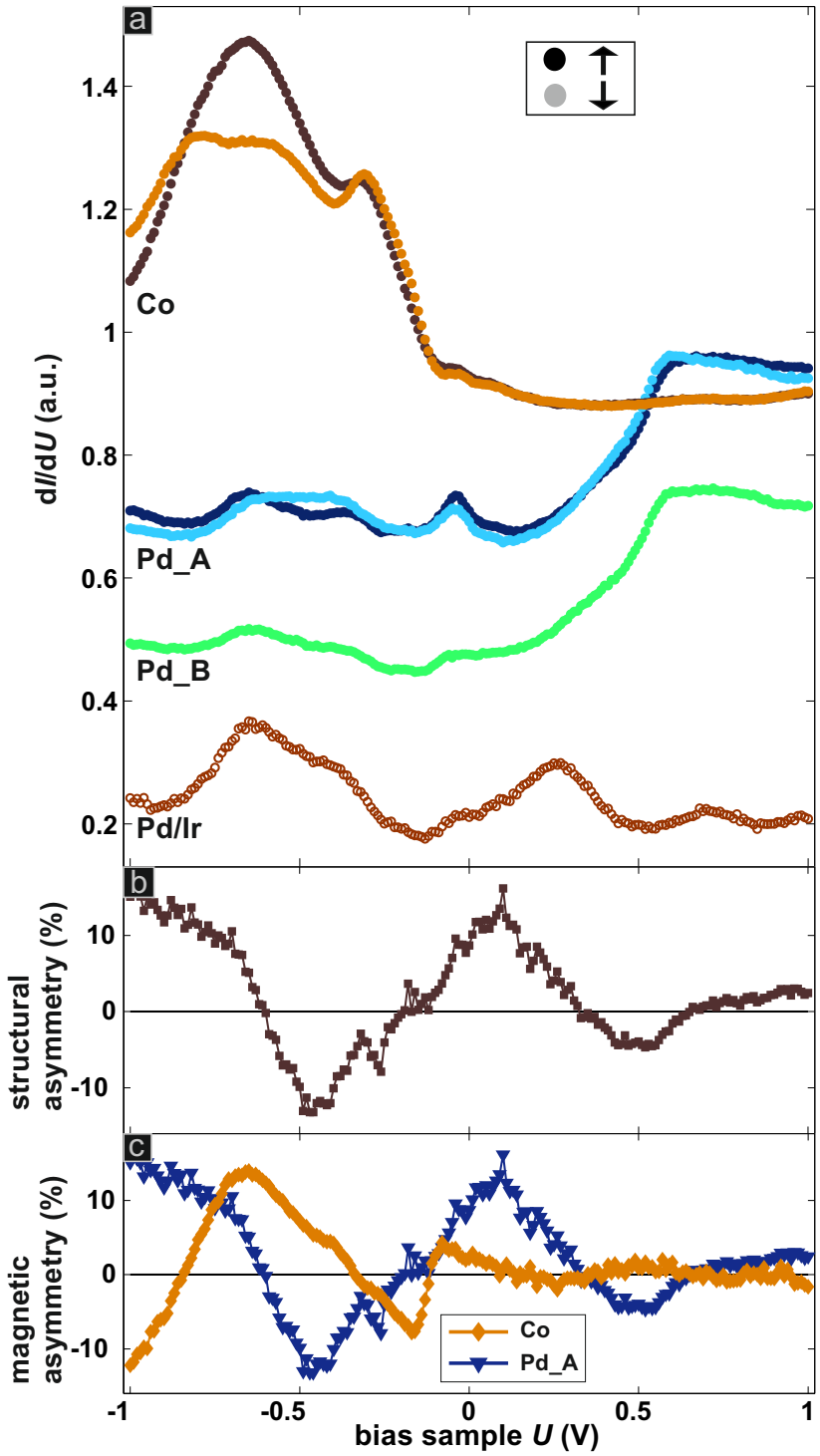

Figure A.3: SP-STS measurements of ML Pd on Co/Ir(111) using a Fe-coated W tip: (a) Spin-resolved dI/dU spectra of the sample: $U_{\mathrm{stab}} = +1$ V, $I_{\mathrm{stab}} = 0.8$ nA, $U_{\mathrm{mod}} = 25$ mV. Each spectrum displayed is an average of 5 single spectra. Spectra of Co and Pd of different stackings (Pd_A and Pd_B) are shifted vertically by multiples of 0.2 arb. units for clarity. (b) Structural asymmetry calculated for spectra of Pd of different stackings. (c) Magnetic asymmetries calculated for spin-resolved spectra of Co and Pd_A.

Appendix B

Figures of Co atoms on ML Pd on Co/Ir(111)

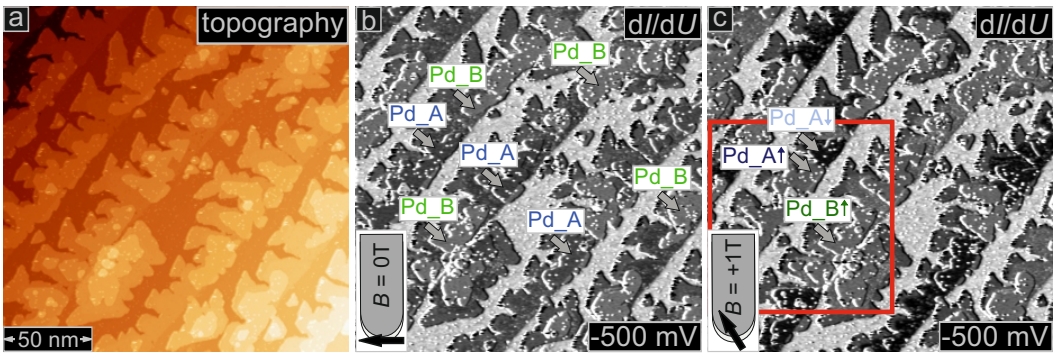

Figure B.1: SP-STM measurements of Co atoms on ML Pd on Co/Ir(111): (a) Constant-current image measured at $B = 0$ T, (b) and (c) the simultaneously acquired spin-resolved $\mathrm{d}I/\mathrm{d}U$ maps measured at $B = 0$ T and $B = +1$ T, respectively. Measurement parameters: $I = 1.5$ nA, $U = -500$ mV and $U_{\mathrm{mod}} = 30$ mV.

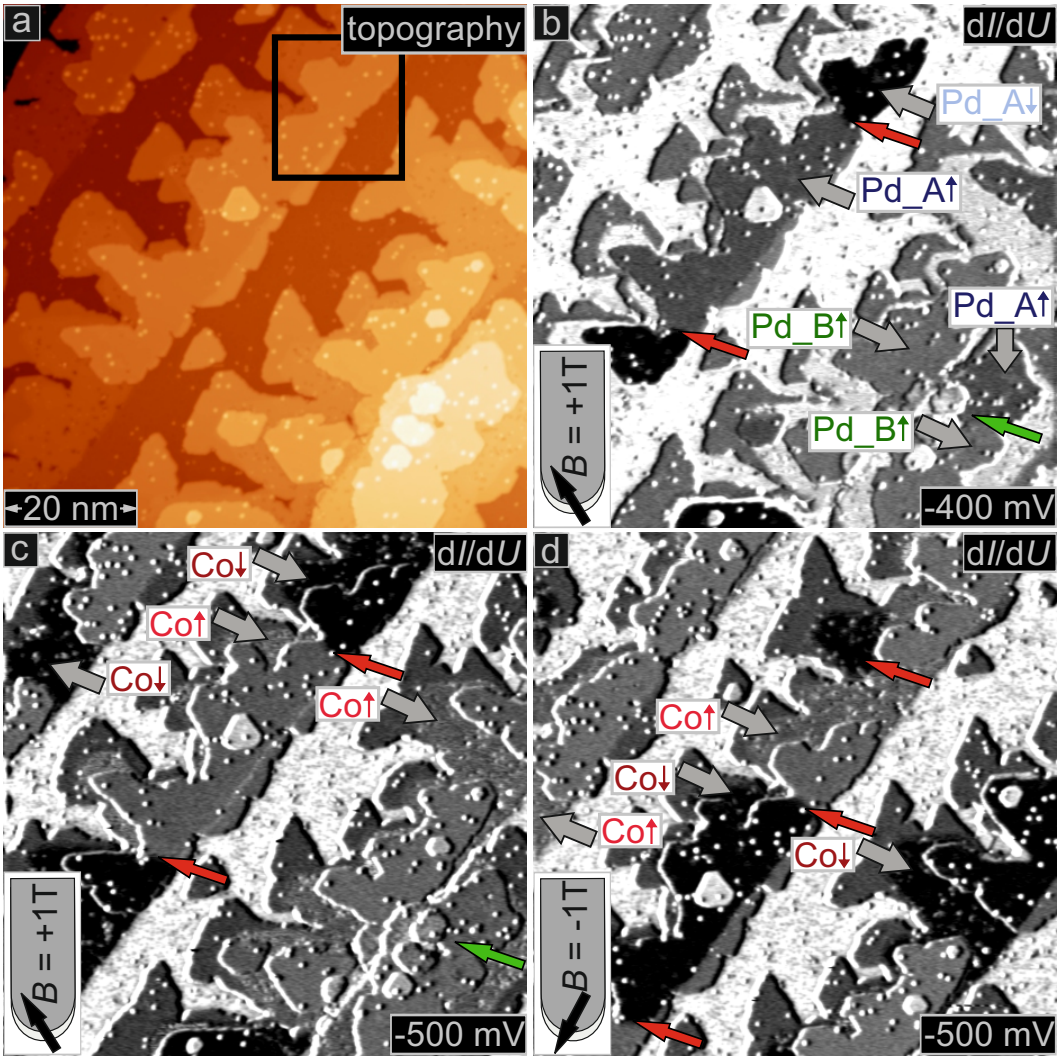

Figure B.2: A higher magnification SP-STM images of the area highlighted by a red box in Fig. B.1(c): (a) Constant-current image measured at $B = +1$ T, (b) and (c) the simultaneously acquired spin-resolved $\mathrm{d}I/\mathrm{d}U$ maps recorded at $U = -400$ mV and $U = -500$ nV, respectively. Both maps were measured at $B = +1$ T. (d) Spin-resolved $\mathrm{d}I/\mathrm{d}U$ map of the same sample area observed at $B = -1$ T. Green arrows of (b) and (c) indicate a dislocation line between two stackings of Pd, while red arrows mark domain walls of Pd/Co as well as of Co films. Measurement parameters: $I = 1.5$ nA and $U_{\mathrm{mod}} = 30$ mV.

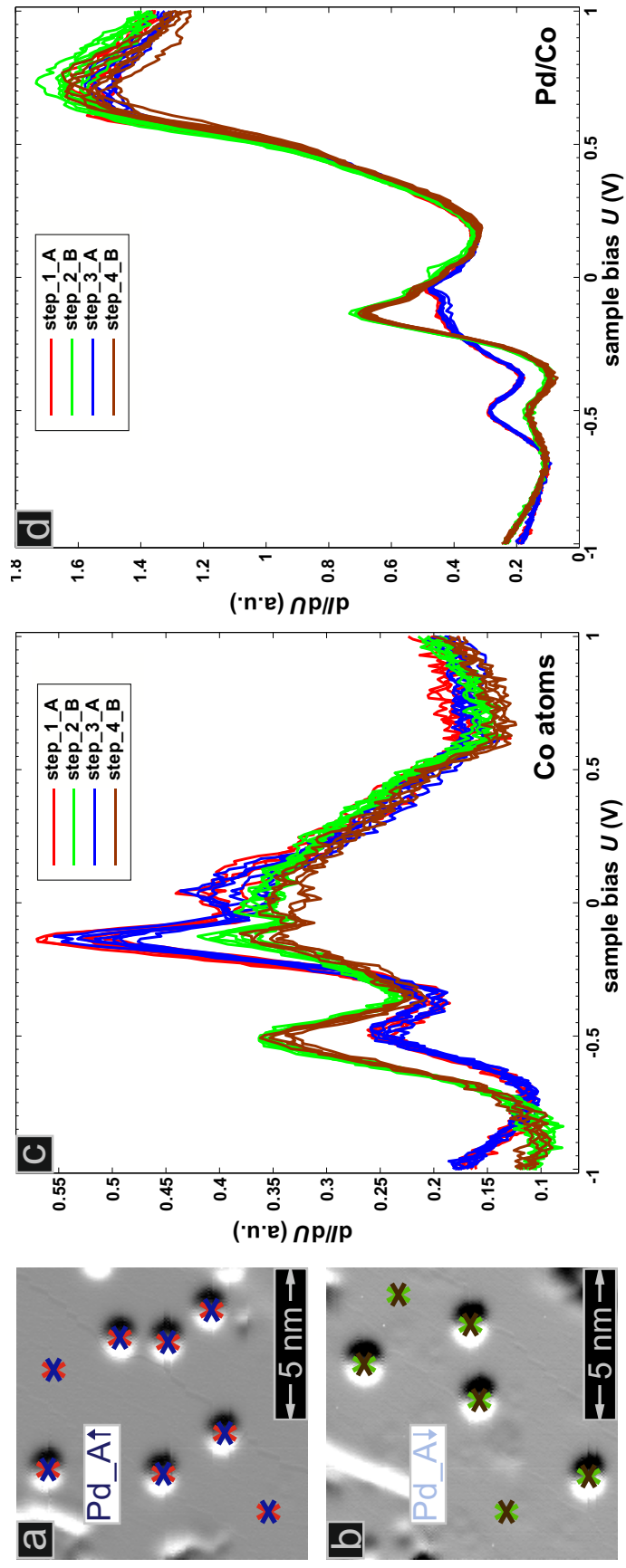

Figure B.3: SP-STS measurements of Co atoms residing on the oppositely magnetized domains of PdCo, as shown in Fig. 6.14(b): (a) and (b) Differentiated constant-current images. (c) and (d) Spin-resolved $\mathrm{d}I/\mathrm{d}U$ spectra of adatoms and substrate, respectively ($U_{\mathrm{stab}} = -1$ V, $I_{\mathrm{stab}} = 1.5$ nA, $U_{\mathrm{mod}} = 30$ mV). Spectroscopic data were taken at $B = +1$ T at locations marked by crosses in (a) and (b). Different colors of spectra are assigned as step_1_A, step_2_B, step_3_A and step_4_B, where indexes from 1 to 4 mean a sequence of measurements, and A and B indicate spectra recorded for (a) and (b), respectively. The fact that spectroscopic data of step_1_A and step_3_A (or those of step_2_B and step_4_B) look alike indicates that the magnetic tip did not change during measurements. This means that the observed spectroscopic differences are purely magnetic in origin.

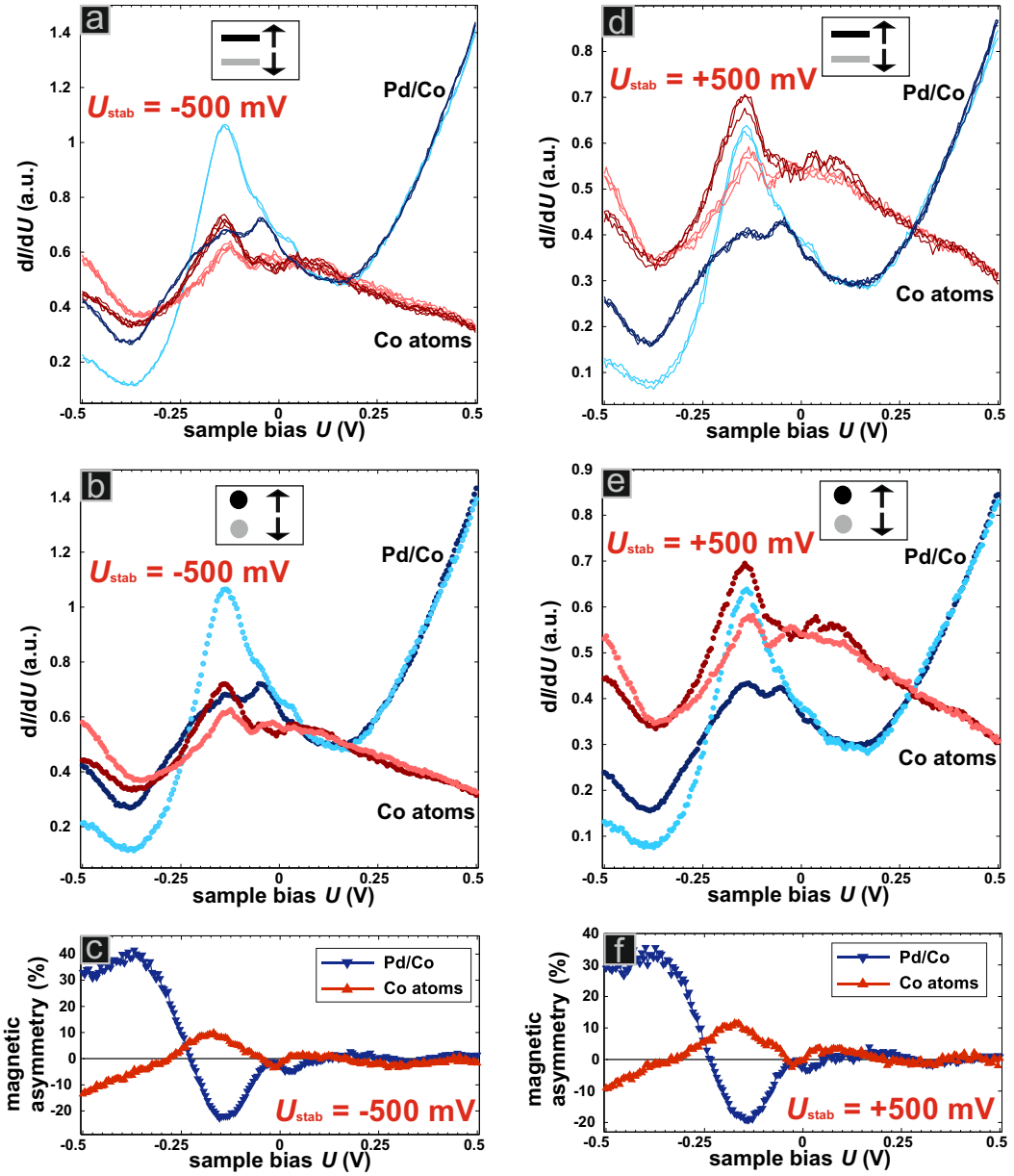

Figure B.4: Spin-resolved spectra of Co atoms and ML Pd: (a,d) Single spectra. (b,e) Averaged spectra from those in (a,d), respectively. (c,f) Magnetic asymmetries calculated for (b,e), respectively. Data in (a-c) were obtained at $U_{\mathrm{stab}} = -500$ mV, whereas those in (d-f) were taken at $U_{\mathrm{stab}} = +500$ mV. All measurements were done at $I_{\mathrm{stab}} = 1.5$ nA, $U_{\mathrm{mod}} = 30$ mV and $B = +1$ T. Light and dark colors indicate spectra recorded at locations marked by crosses in Figs. B.3(a) and (b), respectively.

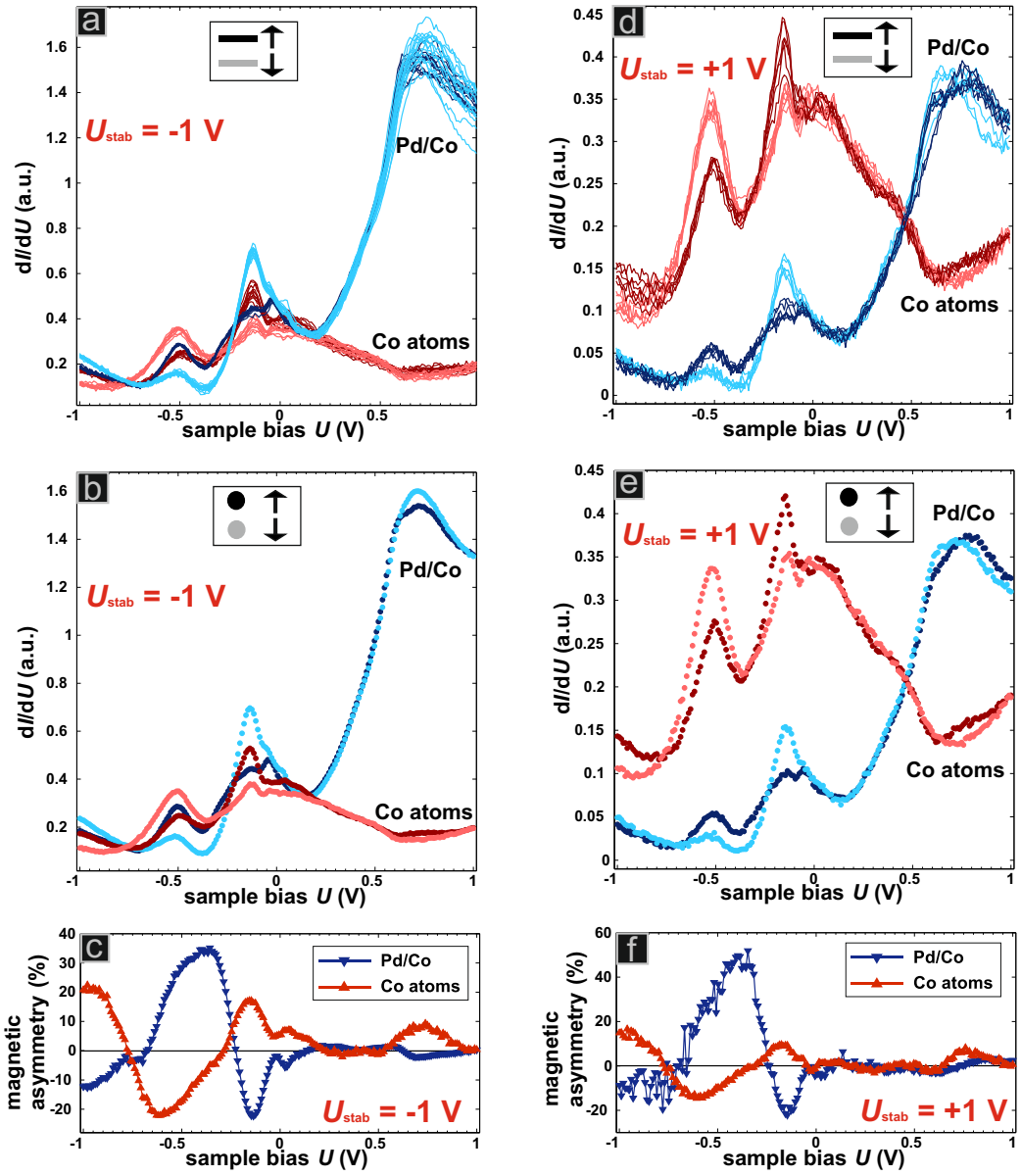

Figure B.5: Spin-resolved spectra of Co atoms and ML Pd: (a,d) Single spectra. (b,e) Averaged spectra from those in (a,d), respectively. (c,f) Magnetic asymmetries calculated for (b,e), respectively. Data in (a-c) were obtained at $U_{\mathrm{stab}} = -1$ V, whereas those in (d-f) were taken at $U_{\mathrm{stab}} = +1$ V. All measurements were done at $I_{\mathrm{stab}} = 1.5$ nA, $U_{\mathrm{mod}} = 30$ mV and $B = +1$ T. Dark and light colors indicate spectra recorded at locations marked by crosses in Figs. B.3(a) and (b), respectively.

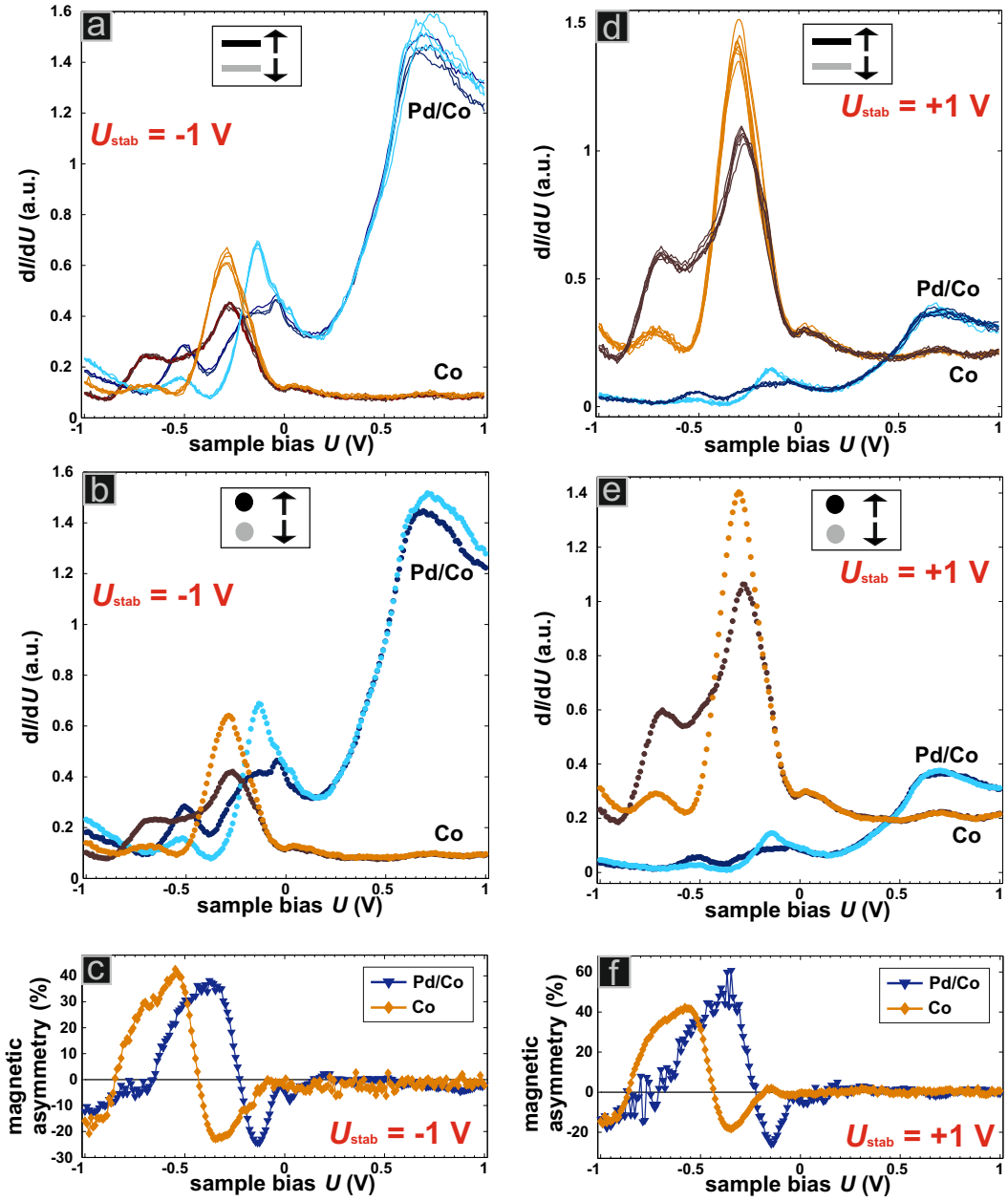

Figure B.6: Spin-resolved spectra of ML Co and ML Pd: (a,d) Single spectra. (b,e) Averaged spectra from those in (a,d), respectively. (c,f) Magnetic asymmetries calculated for (b,e), respectively. Data in (a-c) were obtained at $U_{\mathrm{stab}} = -1$ V, whereas those in (d-f) were taken at $U_{\mathrm{stab}} = +1$ V. All measurements were done at $I_{\mathrm{stab}} = 1.5$ nA, $U_{\mathrm{mod}} = 30$ mV and $B = +1$ T. Dark and light colors indicate spectra recorded for Pd/Co domains showing strong and weak $\mathrm{d}I/\mathrm{d}U$ signals in Figs. 6.14(b) Chap. 6, respectively.

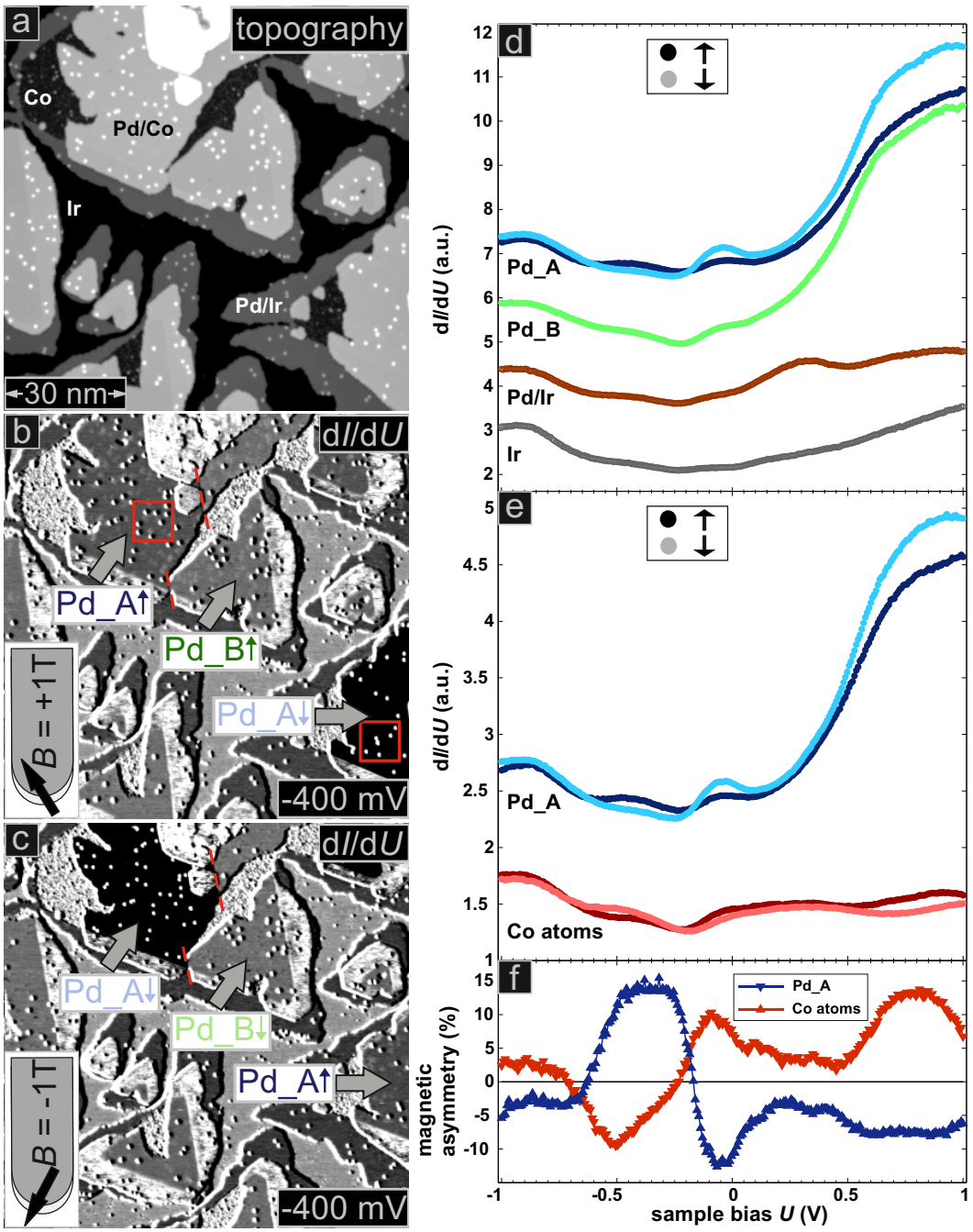

Figure B.7: SP-STM measurements of Co atoms on ML Pd on Co/Ir(111): (a) Constant-current image measured at $B = +1$ T. (b) and (c) Simultaneously acquired spin-resolved $\mathrm{d}I/\mathrm{d}U$ maps measured at $B = +1$ T and $B = -1$ T, respectively. (d) and (e) Spin-resolved spectra ($U_{\mathrm{stab}} = -1$ V, $I_{\mathrm{stab}} = 1$ nA, $U_{\mathrm{mod}} = 80$ mV). Dark and light colors indicate spectra recorded for the oppositely magnetized regions of the surface shown in (b). Each spectrum is an average of five single spectra. All spectra in (d) except that of Ir, and those of Pd_A in (e) are vertically shifted by multiples of 1.5 arb. units for clarity. (f) Magnetic asymmetries calculated for (e). Measurement parameters: $I = 1$ nA, $U = -400$ mV and $U_{\mathrm{mod}} = 80$ mV.

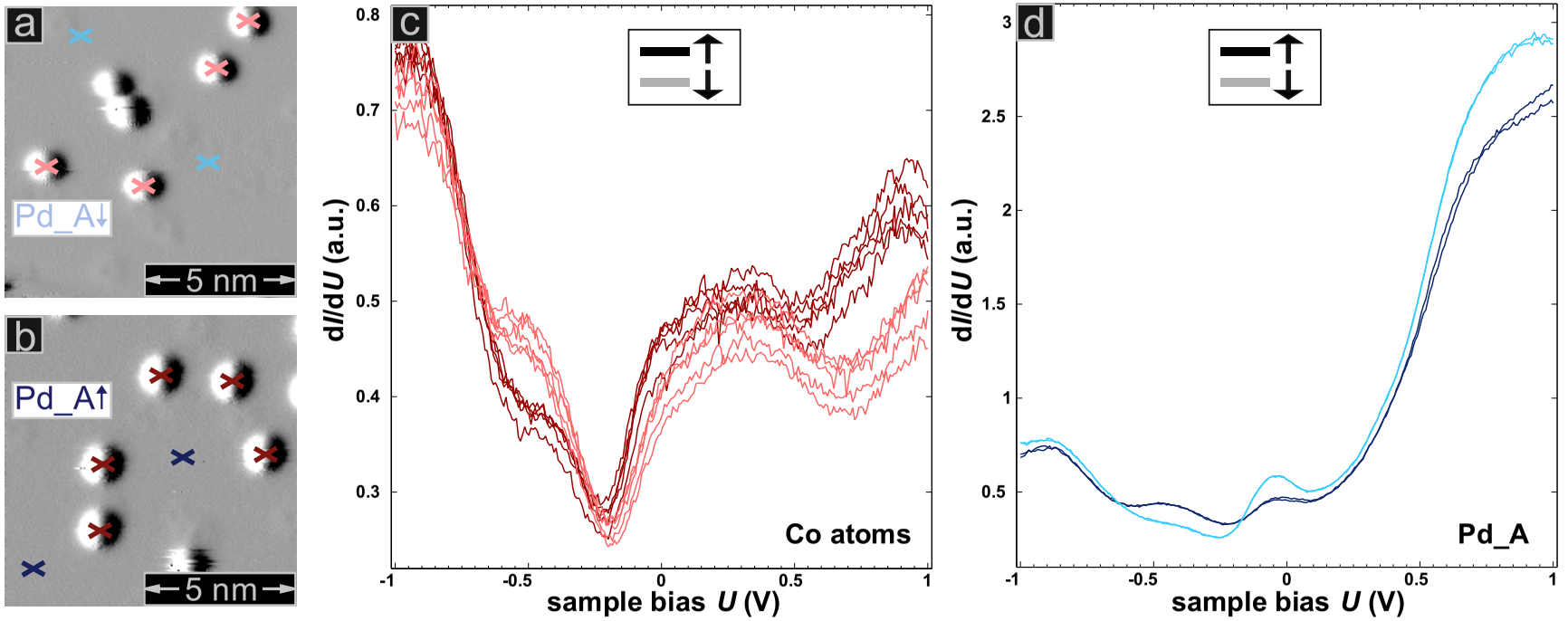

Figure B.8: SP-STS measurements of Co atoms residing on the oppositely magnetized Pd/Co islands, as highlighted by red boxes in Fig. B.7(b): (a) and (b) Differentiated constant-current images. (c) and (d) Spin-resolved $\mathrm{d}I/\mathrm{d}U$ spectra of adatoms and a substrate, respectively ($U_{\mathrm{stab}} = -1$ V, $I_{\mathrm{stab}} = 1$ nA, $U_{\mathrm{mod}} = 80$ mV). Spectroscopic data were taken at $B = +1$ T at locations marked by crosses in (a) and (b).

Bibliography

[1] H. Brune and P. Gambardella. Surf. Science **603**, 1812 (2009).

[2] G. Bergmann. Phys. Today **32**, 75 (1979).

[3] G. Bergmann. J. Magn. Magn. Mater. **35**, 68 (1983).

[4] J. S. Moodera and R. Meservey. Phys. Rev. B **34**, 379 (1986).

[5] P. Gambardella, S. S. Dhesi, S. Gardonio, C. Grazioli, P. Ohresser, and C. Carbone. Phys. Rev. Lett. **88**, 047202 (2002).

[6] F. Meier, L. Zhou, J. Wiebe, and R. Wiesendanger. Science **320**, 82 (2008).

[7] L. Zhou, F. Meier, J. Wiebe, and R. Wiesendanger. Phys. Rev. B **82**, 012409 (2010).

[8] A. A. Khajetoorians, S. Lounis, B. Chilian, A. T. Costa, L. Zhou, D. L. Mills, J. Wiebe, and R. Wiesendanger. Phys. Rev. Lett. **106**, 037205 (2011).

[9] Y. Yayon, V. W. Brar, L. Senapati, S. C. Erwin, and M. F. Crommie. Phys. Rev. Lett. **99**, 067202 (2007).

[10] D. Serrate, P. Ferriani, Y. Yoshida, S.-W. Hla, M. Menzel, K. von Bergmann, S. Heinze, A. Kubetzka, and R. Wiesendanger. Nature Nanotech. **5**, 350 (2010).

[11] A. J. Heinrich, J. A. Gupta, C. P. Lutz, and D. M. Eigler. Science **306**, 466 (2004).

[12] T. Balashov, T. Schuh, A. F. Takacs, A. Ernst, S. Ostanin, J. Henk, I. Mertig, P. Bruno, T. Miyamachi, S. Suga, and W. Wulfhekel. Phys. Rev. Lett. **102**, 257203 (2009).

[13] B. W. Heinrich, C. Iacovita, M. V. Rastei, L. Limot, J. P. Bucher, P. A. Ignatiev, V. S. Stepanyuk, and P. Bruno. Phys. Rev. B **79**, 113401 (2009).

[14] M. Ziegler, N. Néel, C. Lazo, P. Ferriani, S. Heinze, Kröger, and R. Berndt. New J. Phys. **13**, 085011 (2011).

[15] R. Decker, J. Brede, N. Atodiresei, V. Caciuc, S. Blügel, and R. Wiesendanger. submitted (2012).

[16] L. Berbil-Bautista, S. Krause, T. Hänke, M. Bode, and R. Wiesendanger. Surf. Sci. **600**, L20 (2006).

[17] R. Bäcker and G. Hörz. Fresenius' J. Anal. Chem. **353**, 757 (1995).

[18] Y.-S. Fu, Q.-K. Xue, and R. Wiesendanger. Phys. Rev. Lett. **108**, 087203 (2012).

[19] J. Prokop, A. Kukunin, and H. J. Elmers. Phys. Rev. B **75**, 144423 (2007).

[20] J.-F. Jia, S.-C. Li, Y.-F. Zhang, and Q.-K. Xue. J. Phys. Soc. Jpn. **76**, 082001 (2007).

[21] M. Getzlaff. *Fundamentals of Magnetism*, Springer, Berlin (2008).

[22] A. Enders, R. Skomski, and J. Honolka. J. Phys. Condens. Matter **22**, 433001 (2010).

[23] S. Blundell. *Magnetism in Condensed Matter*, Oxford University Press, Oxford (2010).

[24] R. Skomski. *Simple Models of Magnetism*, Oxford University Press, Oxford (2008).

[25] P. Bruno. Phys. Rev. B **52**, 411 (1995).

[26] O. O. Brovko, P. A. Ignatiev, V. S. Stepanyuk, and P. Bruno. Phys. Rev. Lett. **101**, 036809 (2008).

[27] B. Giovannini and M. Peter. Phys. Rev. Lett. **12**, 736 (1964).

[28] A. Oswald, R. Zeller, and P. H. Dederichs. Phys. Rev. Lett. **56**, 1419 (1986).

[29] Y. Takahashi. J. Appl. Phys. **85**, 5744 (1999).

[30] S. Krause. Ph.D. thesis, Hamburg University (2008).

[31] M. Menzel. Ph.D. thesis, Hamburg University (2011).

[32] J. Tersoff and D. R. Hamann. Phys. Rev. Lett. **50**, 1998 (1983).

[33] J. Tersoff and D. R. Hamann. Phys. Rev. B **31**, 805 (1985).

[34] J. Bardeen. Phys. Rev. Lett. **6**, 57 (1961).

[35] J. C. Slonczewski. Phys. Rev. B **39**, 6995 (1989).

[36] M. Julliere. Phys. Lett. A **54**, 225 (1975).

[37] R. Wiesendanger, H.-J. Güntherodt, D. Güntherodt, R. J. Gambino, and R. Ruf. Phys. Rev. Lett. **65**, 247 (1990).

[38] A. A. Khajetoorians, J. Wiebe, B. Chilian, and R. Wiesendanger. Science **332**, 1062 (2010).

[39] S. Loth, K. von Bergmann, M. Ternes, A. F. Otte, C. P. Lutz, and A. J. Heinrich. Nature Phys. **6**, 340 (2010).

[40] S. Loth, M. Etzkorn, C. P. Lutz, D. M. Eigler, and A. J. Heinrich. Science **329**, 1628 (2011).

[41] H. Lüth. *Surfaces and interfaces of solid materials*, Springer-Verlag, Berlin (2001).

[42] http://www.tectra.de/heater.htm .

[43] D. Haude. Master thesis, University of Hamburg (1997).

[44] C. Witt, U. Mick, M. Bode, and R. Wiesendanger. Rev. Sci. Instrum. **69**, 1455 (1997).

[45] O. Pietzsch, A. Kubetzka, D. Haude, M. Bode, and R. Wiesendanger. Rev. Sci. Instrum. **71**, 424 (2000).

[46] A. Kubetzka. Master thesis, University of Hamburg (1999).

[47] R. Wiesendanger. Rev. Mod. Phys. **81**, 1495 (2009).

[48] M. Bode. Rep. Prog. Phys. **66**, 523 (2003).

[49] A. Kubetzka, M. Bode, O. Pietzsch, and R. Wiesendanger. Phys. Rev. Lett. **88**, 057201 (2002).

[50] K. Koike and K.Hayakawa. Jap. J. Appl. Phys. **23**, L187 (1984).

[51] A. Hubert and R. Schäfer. *Magnetic Domains*, Springer, Berlin (1998).

[52] B. Elschner and W. Andrä. Fortschritte der Physik **3**, 163 (1955).

[53] U. Kaiser. *PhD thesis*, Hamburg University, Hamburg (2007).

[54] T. Okuda, J. Lobo-Checa, W. Auwärter, M. Morscher, M. Hoesch, V. N. Petrov, M. Hengsberger, A. Tamai, A. Dolocan, C. Cirelli, M. Corso, M. Muntwiler, M. Klöckner, M. Roos, J. Osterwalder, and T. Greber. Phys. Rev. B **80**, 180404 (2009).

[55] Y. Nishimura, M. Kakeya, M. Higashiguchi, A. Kimura, M. Taniguchi, H. Narita, Y. Cui, M. Nakatake, K. Shimada, and H. Namatame. Phys. Rev. B **79**, 245402 (2009).

[56] S. Pons, P. Mallet, L. Magaud, and J.-Y. Veuillen. Europhys. Lett. **61**, 375 (2003).

[57] K.-F. Braun and K.-H. Rieder. Phys. Rev. B **77**, 245429 (2008).

[58] J. Braun and M. Donath. Europhys. Lett. **59**, 592 (2002).

[59] P. R. Wallace. Phys. Rev. B **71**, 622 (1947).

[60] J. W. McClure. Phys. Rev. B **104**, 666 (1956).

[61] J. C. Slonczewski and P. R. Weiss. Phys. Rev. B **109**, 272 (1958).

[62] G. W. Semenoff. Phys. Rev. Lett. **53**, 2449 (1984).

[63] E. Fradkin. Phys. Rev. B **33**, 3263 (1986).

[64] F. D. M. Haldane. Phys. Rev. Lett. **61**, 2015 (1988).

[65] K. S. Novoselov, A. K. Geim, S. V. Morozov, D. Jiang, Y. Zhang, S. V. Dubonos, I. V. Grigorieva, and A. A. Firsov. Science **306**, 666 (2004).

[66] K. S. Novoselov, D. Jiang, F. Schedin, T. J. Booth, and V. V. Khotkevich. Proc. Natl. Acad. Sci. USA **102**, 0451 (2005).

[67] K. S. Novoselov, A. K. Geim, S. V. Morozov, D. Jiang, M. I. Katsnelson, I. V. Grigorieva, S. V. Dubonos, and A. A. Firsov. Nature **438**, 197 (2005).

[68] Y. B. Zhang, Y. W. Tan, H. L. Stormer, and P. Kim. Nature **438**, 201 (2005).

[69] H. B. Heersche, P. Jarill-Herrero, J. B. Oostinga, L. M. K. Vandersypen, and A. F. Morpurgo. Nature **446**, 56 (2007).

[70] K. S. Novoselov, Z. Jiang, Y. Zhang, S. V. Morozov, H. L. Stormer, U. Zeitler, J. C. Maan, G. S. Boebinger, P. Kim, and A. K. Geim. Science **315**, 1379 (2007).

[71] A. Gräneis, K. Kummer, and D. V. Vyalikh. New J. of Phys. **11**, 073050 (2009).

[72] K. S. Novoselov. Nature Materials **6**, 720 (2007).

[73] G. Bertoni, L. Calmels, A. Altibelli, and V. Serin. Phys. Rev. B **71**, 075402 (2005).

[74] Y. S. Dedkov, M. Fonin, U. Rüdiger, and C. Laubschat. Phys. Rev. Lett. **100**, 107602 (2008).

[75] Y. S. Dedkov, M. Fonin, and C. Laubschat. Appl. Phys. Lett. **92**, 052506 (2008).

[76] A. N. Obraztsov. Nature Nanotech. **4**, 212 (2009).

[77] Q. Yu, J. Lian, S. Siriponglert, H. Li, Y. P. Chen, and S.-S. Pei. Appl. Phys. Lett. **93**, 113103 (2008).

[78] J. Wintterlin, J. Wiechers, H. Brune, T. Gritsch, H. Höfer, and R. J. Behm. Phys. Rev. Lett. **62**, 59 (1989).

[79] K.-F. Braun and S.-W. Hla. Appl. Phys. A **98**, 583 (2010).

[80] Y. Gamo, A. Nagashima, M. Wakabayashi, M. Terai, and C. Oshima. Surf. Sci. **374**, 61 (1997).

[81] M. Fuentes-Cabrera, M. I. Baskes, A. V. Melechko, and M. L. Simpson. Phys. Rev. B **77**, 035405 (2008).

[82] M. Weser, Y. Rehder, K. Horn, M. Sicot, M. Fonin, A. B. Preobrajenski, E. N. Voloshina, E. Goering, and Y. S. Dedkov. Appl. Phys. Lett. **96**, 012504 (2010).

[83] M. Weser, E. N. Voloshina, K. Horn, and Y. S. Dedkov. Phys. Chem. Chem. Phys. **13**, 7534 (2011).

[84] A. Kubetzka, O. Pietzsch, M. Bode, and R. Wiesendanger. Phys. Rev. B **67**, 020401 (2003).

[85] P. E. Blöchl. Phys. Rev. B **50**, 17953 (1994).

[86] G. Kresse and J. Hafner. J. Phys.: Cond. Matt. **6**, 8245 (1994).

[87] G. Kresse and D. Joubert. Phys. Rev. B **59**, 1758 (1999).

[88] J. P. Perdew, K. Burke, and M. Ernzerhof. Phys. Rev. Lett. **77**, 3865 (1996).

[89] S. Grimme. J. Comp. Chem. **27**, 1787 (2006).

[90] P. A. Khomyakov, G. Giovannetti, P. C. Rusu, G. Brocks, J. van den Brink, and P. J. Kelly. Phys. Rev. B **79**, 195425 (2009).

[91] P. E. Blöchl, O. Jepsen, and O. K. Andersen. Phys. Rev. B **49**, 16223 (1994).

[92] L. Olesen, M. Brandbyge, M. R. Sørensen, K. W. Jacobsen, E. Lægsgaard, I. Stensgaard, and F. Besenbacher. Phys. Rev. Lett. **76**, 1485 (1996).

[93] J. J. W. M. Rosink, M. A. Blauw, L. J. Geerligs, E. van der Drift, and S. Radelaar. Phys. Rev. B **62**, 10459 (2000).

[94] O. Jepsen and O. Andersen. Zeitschrift für Physik B Cond. Matt. **97**, 35 (1995).

[95] L. Magaud, A. Pasturel, P. Mallet, S. Pons, and J.-Y. Veuillen. Europhys. Lett. **67**, 90 (2004).

[96] T. Ohwaki, D. Wortmann, H. Ishida, S. Blügel, and K. Terakura. Phys. Rev. B **73**, 235424 (2006).

[97] D. Tomänek, S. G. Louie, H. J. Mamin, D. W. Abraham, R. E. Thomson, E. Ganz, and J. Clarke. Phys. Rev. B **35**, 7790 (1987).

[98] R. Frömter, S. Hankemeier, H. P. Oepen, and J. Kirschner. Rev. Sci. Instrum. **82**, 033704 (2011).

[99] I. M. Pussei. Isv. Akad. Nauk. S.S.S.R., Ser. Phys. **21**, 1088 (1957).

[100] J. J. M. Franse and G. D. Vries. Physica **39**, 477 (1968).

[101] H. P. Oepen and J. Kirschner. Phys. Rev. Lett. **62**, 819 (1989).

[102] T. O. Wehling, A. I. Lichtenstein, and M. I. Katsnelson. Phys. Rev. B **84**, 235110 (2011).

[103] B. Uchoda, L. Yang, S.-W. Tsai, N. M. R. Reres, and A. H. C. Neto. Phys. Rev. Lett. **103**, 206804 (2009).

[104] K. T. Chan, J. B. Neaton, and M. L. Cohen. Phys. Rev. B **77**, 235430 (2008).

[105] Y. Mao, J. Yuan, and J. Zhong. J. Phys. Condens. Matter **20**, 115209 (2008).

[106] T. O. Wehling, A. V. Balatsky, M. I. Katsnelson, A. I. Lichtenstein, and A. Rosch. Phys. Rev. B **81**, 115427 (2010).

[107] M. Gyamfi, T. Eelbo, M. Waśniowska, T. O. W. S. Forti, U. Starke, A. I. Lichtenstein, M. I. Katsnelson, and R. Wiesendanger. Phys. Rev. B **85**, 161406(R) (2012).

[108] M. Gyamfi, T. Eelbo, M. Waśniowska, and R. Wiesendanger. Phys. Rev. B **84**, 113403 (2011).

[109] R. H. Victora and J. M. MacLaren. J. Appl. Phys. **69**, 5652 (1991).

[110] V. L. Moruzzi and P. M. Marcus. Phys. Rev. B **39**, 471 (1989).

[111] H. Chen, N. E. Brener, and J. Callaway. Phys. Rev. B **40**, 1443 (1989).

[112] G. G. Low and T. M. Holden. Proc. Phys. Soc. **89**, 116 (1966).

[113] S. Blügel, B. Drittler, R. Zeller, and P. H. Dederichs. Appl. Phys. A **49**, 547 (1989).

[114] H. J. G. Draaisma, W. J. M. de Jonge, and F. J. A. den Broeder. J. Magn. Magn. Mater. **66**, 351 (1987).

[115] J. V. Harzer, B. Hillebrands, R. L. Stamps, G. Güntherdt, C. D. England, and M. Falco. J. Appl. Phys. **62**, 2448 (1991).

[116] J. E. Bickel, F. Meier, J. Brede, A. Kubetzka, K. von Bergmann, and R. Wiesendanger. Phys. Rev. B **84**, 054454 (2011).

[117] H. Brune, C. Romainczyk, H. Röder, and K. Kern. Nature **369**, 469 (1994).

[118] H. Brune, H. Röder, C. Romainczyk, C. Boragno, and K. Kern. Appl. Phys. A **60**, 167 (1995).

[119] M. Hohage, M. Bott, M. Morgenstern, Z. Zhang, T. Michely, and G. Comsa. Phys. Rev. Lett. **76**, 2366 (1996).

[120] T. Michely, M. Hohage, M. Bott, and G. Comsa. Phys. Rev. Lett. **70**, 3943 (1993).

[121] R. Q. Hwang, J. Schröder, C. Günther, and R. J. Behm. Phys. Rev. Lett. **67**, 3279 (1991).

[122] W. U. Fengmin, J. Zhang, G. Bian, and Z. Wu. Surf. Sci. **6**, 61 (2001).

[123] F. A. Lewis. Platinum Metals Rev. **4**, 132 (1960).

[124] M. Sicot, O. Kurnosikov, O. A. O. Adam, H. J. M. Swagten, and B. Koopmans. Phys. Rev. B **77**, 035417 (2008).

[125] C. R. Abeledo and P. W. Selwood. J. Chem. Phys. **37**, 2709 (1962).

[126] G. J. Mankey, K. M. T, F. Huang, and R. F. Willis. J. Vac. Sci. Technol. A **11**, 2034 (1993).

[127] S. L. F. Meier, L. Z. J. Wiebe, S. Heers, P. Mavropoulos, P. H. Dederichs, S. Blügel, and R. Wiesendanger. Phys. Rev. B **83**, 075407 (2011).

[128] http://www.flapw.de .

[129] J. Brede. *PhD thesis*, Hamburg University, Hamburg (2010).

[130] P. Ferriani, C. Lazo, and S. Heinze. Phys. Rev. B **82**, 054411 (2010).

[131] V. Madhavan, W. Chen, T. Jamneala, M. F. Crommie, and N. S. Wingreen. Science **280**, 567 (1998).

[132] A. J. H. J. A. Gupta, C. P. Lutz, and D. M. Eigler. Science **306**, 466 (2008).

[133] A. F. Otte, M. Ternes, K. von Bergmann, S. Loth, H. Brune, C. P. Lutz, C. F. Hirjibehedin, and A. J. Heinrich. Nat. Phys. **4**, 847 (2008).

[134] V. V. Mazurenko, S. N. Isakov, A. N. Rudenko, V. I. Anisimov, and A. I. Lichtenstein. Phys. Rev. B **82**, 193403 (2010).

[135] V. V. Mazurenko, S. N. Isakov, M. V. Valentyuk, A. N. Rudenko, and A. I. Lichtenstein. Phys. Rev. B **84**, 193407 (2011).

[136] K. Miura, H. Kimura, S. Imanaga, and Y. Hayafuji. J. Appl. Phys. **72**, 4826 (1992).

[137] W. Auwärter, H. U. Suter, H. Sachdev, and T. Greber. Chem. Mater. **16**, 343 (2004).

[138] Y. Li, W. Zhang, M. Morgenstern, and R. Mazzarello. http://arxiv.org/abs/1210.2876 (2012).

[139] C. Rau, G. Xing, C. Liu, and M. Robert. Phys. Lett. A **135**, 227 (1988).

[140] H. Beckmann, F. Ye, and G. Bergmann. Phys. Rev. Lett. **73**, 1715 (1994).

Publications

Research articles:

L. V. Dzemiantsova, M. Karolak, F. Lofink, A. Kubetzka , B. Sachs, K. von Bergmann, S. Hankemeier, T. O. Wehling, R. Frömter, H. P. Oepen, A. I. Lichtenstein and R. Wiesendanger: *Multiscale magnetic study of Ni(111) and graphene on Ni(111).* Phys. Rev. B **84**, 205431 (2011)

L. V. Dzemiantsova, M. Hortamani, C. Hanneken, A. Kubetzka , K. von Bergmann and R. Wiesendanger: *Magnetic coupling of single Co adatoms to a Co underlayer through a Pd spacer of variable thickness.* Phys. Rev. B **86**, 094427 (2012)

Talks and Conferences:

L. V. Dzemiantsova, A. Kubetzka , K. von Bergmann and R. Wiesendanger: *SP-STM study on Ni(111).* Frühjahrstagung der Deutschen Physikalischen Gesellschaft, Dresden, GERMANY, 13-18 March 2011 (Talk)

L. V. Dzemiantsova, A. Kubetzka , K. von Bergmann and R. Wiesendanger: *Single Co atoms on Pd/Co/Ir(111): electronic and magnetic properties.* Group-seminar, Hamburg, GERMANY, 16 January 2012 (Talk)

L. V. Dzemiantsova, A. Kubetzka , K. von Bergmann and R. Wiesendanger, *SP-STM study of individual Co atoms on Pd/Co/Ir(111).* Frühjahrstagung der Deutschen Physikalischen Gesellschaft, Berlin, GERMANY, 25-30 March 2012 (Talk)

L. V. Dzemiantsova, A. Kubetzka , K. von Bergmann and R. Wiesendanger: *SP-STM study of individual Co atoms on Pd/Co/Ir(111).* ICN+T (International Conference of Nanoscience and Technology), Paris, FRANCE, 23-27 July 2012 (Talk)

L. V. Dzemiantsova, A. Kubetzka , K. von Bergmann and R. Wiesendanger: *SP-STM study of individual Co atoms on Pd/Co/Ir(111).* SPS-12&SPSTM-4 Workshop (Scanning Probe Microscopy and Spin-polarized Scunning Tunneling Microscopy), Timmendorfer Strand, GERMANY, 09-12 September 2012 (Talk)

L. V. Dzemiantsova and R. Wiesendanger: *Atomic-scale magnetism by SP-STM.* SSS TMAS II (Second International Surface Science "Technologies and Measurements on Atomic Scale"), Sochi, RUSSIA, 01-07 Oktober 2012 (Lecture)

Danksagung

Ich danke Prof. Dr. Roland Wiesendanger für die Möglichkeit, meine Doktorarbeit in diesem hervorragenden wissenschaftlichen Umfeld anzufertigen, und für die fortwährende Unterstützung.

Allen voran danke ich Kirsten von Bergmann und Anrdré Kubetzka, für die umfassende und gründliche Betreuung sämtlicher Phasen meiner Promotion und für ihre endlose Geduld, die ich nicht für selbstverständlich halte.

Matthias Menzel, Jessica Bickel, Yasou Yoshida und allen anderen Mitgliedern der Gruppe R danke ich für die produktive und immer angenehme Zusammenarbeit.

Ich danke Felix Marczinowski und Alex Khajetoorians für viele wertvolle Hinweise und die anregenden und produktiven Gesprähe.